TRANSIENTS IN REACTORS FOR POWER SYSTEMS COMPENSATION

HAZIAH ABDUL HAMID

Thesis submitted to Cardiff University in candidature for the degree of

Doctor of Philosophy

School of Engineering

Cardiff University

2012

DECLARATION

This work has not been submitted in substance for any other degree or award at this or any other university or place of learning, nor is being submitted concurrently in candidature for any degree or other award.

Signed …….. (candidate) Date ……

STATEMENT 1

This thesis is being submitted in partial fulfilment of the requirements for the degree of ……PhD…….

Signed ……. (candidate) Date ……

STATEMENT 2

This thesis is the result of my own independent work/investigation, except where otherwise stated. Other sources are acknowledged by explicit references. The views expressed are my own.

Signed ……. (candidate) Date ……

STATEMENT 3

I hereby give consent for my thesis, if accepted, to be available for photocopying and for inter-library loan, and for the title and summary to be made available to outside organisations.

Signed ……. (candidate) Date ……

STATEMENT 4: PREVIOUSLY APPROVED BAR ON ACCESS

I hereby give consent for my thesis, if accepted, to be available for photocopying and for inter-library loans **after expiry of a bar on access previously approved by the Academic Standards & Quality Committee.**

Signed ……. (candidate) Date ……

Acknowledgments

At this moment of accomplishment, first of all, I pay homage to the glorified and exalted be He for the strength and His blessing in completing this thesis.

I am extremely indebted to my supervisor, Professor Manu Haddad, for providing necessary infrastructure and resources to accomplish my research work. Despite his busy schedule, he reviewed my progress throughout and giving valuable suggestions and making corrections.

My sincere appreciation also goes to my second supervisor, Dr.Noureddine Harid, and Dr.Huw Griffiths for their valuable advice and constructive criticism during my annual progress assessment.

I would like to acknowledge the Malaysian Ministry of Higher Education (MOHE) and the University of Malaysia Perlis (UniMAP) for their financial support of this project.

I would also like to extend my appreciation to all my dear friends for the friendship and help offered over the past four years.

My deepest appreciation goes to my beloved parents, my parents-in-law, and all family members for their constant moral support provided throughout my long PhD journey. Lastly, I would like to pay high regards to my husband, Sabri Zakaria, who beyond being a brilliant engineer has been a pillar of constant support. Thank you to my two adorable little girls, Nani and Hana, who remain the inspiration for me to complete my PhD. Their many gazes and cuddles comforted me in the long hours of work, especially when I was at my wits end with revisions and rewrites necessary to complete this thesis.

Abstract

This thesis describes new models and investigations into switching transient phenomena related to the shunt reactors and the Mechanically Switched Capacitor with Damping Network (MSCDN) operations used for reactive power control in the transmission system. Shunt reactors and MSCDN are similar in that they have reactors. A shunt reactor is connected parallel to the compensated lines to absorb the leading current, whereas the MSCDN is a version of a capacitor bank that has been designed as a C-type filter for use in the harmonic-rich environment.

In this work, models have been developed and transient overvoltages due to shunt reactor deenergisation were estimated analytically using MathCad, a mathematical program. Computer simulations were then undertaken using the ATP/EMTP program to reproduce both single-phase and three-phase shunt reactor switching at 275 kV operational substations. The effect of the reactor switching on the circuit breaker grading capacitor was also examined by considering various switching conditions.

The main original achievement of this thesis is the clarification of failure mechanisms occurring in the air-core filter reactor due to MSCDN switching operations. The simulation of the MSCDN energisation was conducted using the ATP/EMTP program in the presence of surge arresters. The outcome of this simulation shows that extremely fast transients were established across the air-core filter reactor. This identified transient event has led to the development of a detailed air-core reactor model, which accounts for the inter-turn RLC parameters as well as the stray capacitances-to-ground. These parameters are incorporated into the transient simulation circuit, from which the current and voltage distribution across the winding were derived using electric field and equivalent circuit modelling. Further analysis of the results has revealed that there are substantial dielectric stresses imposed on the winding insulation that can be attributed to a combination of three factors. (i) First, the surge arrester operation during the MSCDN energisation, which causes steep voltage change at the reactor terminal. (ii) Second, the non-uniform voltage distribution, resulting in high stresses across the top inter-turn windings. (iii) Third, the rapid rate-of-change of voltage in the assumed worst-case reactor winding location. This is accompanied by a high dielectric (displacement) current through the inter-turn winding insulation.

Work within this investigation proposes that a synergistic effect of high electric field and high dielectric current occurring at worst energisation, followed by the thermal effects of steady state operation contributes to the failure of air-core reactors used on the 400 kV MSCDN.

List of Publications

1. H. Abdul Hamid, N. Harid, and A. Haddad, 2011. Stress Distribution on Mechanically Switched Capacitor with Damping Network Reactor during Energisation. *Proceedings of the 17th International Symposium on High Voltage Engineering (ISH2011)*. Hannover, Germany: 22-26 August, 2011.

2. H. Abdul Hamid, N. Harid, and A. Haddad, 2010. Transient Analysis during Switching of Mechanically Switched Capacitor and Damping Network (MSCDN). *Proceedings of the 45th International Universities' Power Engineering Conference (UPEC2010)*.Cardiff, United Kingdom: 31 August-3 September, 2010.

3. H. Abdul Hamid, N. Harid, and A. Haddad, A.2009. Determination of Transient Overvoltages during Shunt Reactor Deenergization. *Proceedings at the 44th International Universities' Power Engineering Conference (UPEC2009)*.Glasgow, United Kingdom: 1-4 September, 2009.

List of Abbreviations

ATP	Alternative Transients Program
BS	British Standard
CIGRE	International Council on Large Electric Systems
EHV	Extra High Voltage
EM	Electromagnetic
EMTP	Electromagnetic Transients Program
HV	High Voltage
HVAC	High Voltage Alternating Current
HVDC	High Voltage Direct Current
IEC	International Electrotechnical Commission
IEEE	Institute of Electrical and Electronics Engineers
MCOV	Maximum Continuous Operating Voltage
MSC	Mechanically Switched Capacitors
MSCDN	Mechanically Switched Capacitor with Damping Network
NGC	National Grid Company
POW	Point-on-wave
RMS	Root-mean-square
SC	Synchronous Compensator
SVC	Static Var Compensator/
TOV	Temporary Overvoltage
UK	United Kingdom

List of Symbols

CB	circuit breaker
V_o	source voltage
C_L	load side capacitance
C_s	source side capacitance
C_p	stray capacitance of the circuit breaker
C_g	winding capacitance-to-ground
C_{tt}	winding effective series capacitance
C_g	winding capacitance-to-ground
C_{tk}	inter-turn capacitance of section k
C_{gk}	capacitance-to-ground of section k
L_{wk}	winding turns of section k
L	shunt reactor inductance
L_b	buswork inductance
L_p	stray inductance of the circuit breaker
L_s	source side inductance
S_{cc}	Short-circuit level
R_{pk}	inter-turn insulation resistance of section k
R_{wk}	series winding resistance of section k

Table of Contents

Chapter 1: Introduction

Voltage variations and interruptions are inevitable phenomena in any electrical system around the world. The reasons for deficiencies in system voltage quality lie both within the responsibilities of the network operators and the connected customers. Fluctuating loads or loads that change drastically or abruptly is one of the events that causes voltage variations and interruptions in the power system. Apart from that, voltage interruptions are usually the results of faults in the power system and switching actions to isolate the faulty section, switching operations of the circuit breaker, and natural lightning phenomena.

Nevertheless, a good power system will maintain its voltage and frequency close to the rated system values. Table 1.1 presents voltage requirement limits of high voltage systems in the United Kingdom [1.1]. During normal operation of an electrical power system, the voltages must be maintained within a small range, from 0.95 to 1.05 p.u. of the rated value.

Table 1.1: System voltages [1.1]

Nominal system voltage (phase to phase)	400 kV	275 kV	132 kV	13 kV tertiary
Maximum continuous system voltage	420 kV	303 kV	145 kV	16.9 kV
Minimum continuous system voltage	360 kV	247 kV	119 kV	10.4 kV
Rated voltage of plant	400 kV	300 kV	145 kV	17.5 kV

Unlike system frequency, which is consistent throughout an interconnected system, different voltages experienced at points across the system combine to form a voltage profile. This voltage profile is uniquely related to local generation and demand at that instant, and it is also affected by the prevailing system network arrangements. This is predominantly achieved through circuit arrangements, transformers, and

shunt or static compensation [1.2]. Power flows, both actual and potential, must be carefully controlled for a power system to operate within acceptable voltage limits [1.2]. Reactive power flows can give rise to substantial voltage across the system. It is therefore necessary to maintain reactive power balances between sources of generation and points of demand to regulate the system voltage.

Most of the equipment connected to the electrical system will generate or absorb reactive power, but not all equipment can be used efficiently to provide the voltage control [1.2]. For instance, synchronous machines can be made to generate or absorb reactive power depending upon the excitation applied. However, the output of synchronous machines is continuously variable over the operating range, in which case the automatic voltage regulators must be employed to maintain a constant system voltage [1.2].

Shunt reactors and capacitors have been widely employed to regulate or balance reactive power flowing in the power system, thus improve the voltage profile. Reactor is another name for high voltage inductor. They are essentially one-winding transformer. Reactors are used in electric power systems for two main reasons. First, reactors are used in a shunt configuration (line to ground connections) to absorb excess reactive power (Vars) from generation or line charging [1.3, 1.4]. Line charging is the term used to describe the capacitance effects of long transmission lines. Particularly for high voltage (HV) and extra high voltage (EHV) transmission lines, the capacitance effects are naturally formed between the conductors and the ground plane, or between the two conductors separated by a dielectric (air). When such a transmission line is energised at no load or light load, the charging current flow between all phases will create a capacitive effect, which will consequently

cause the receiving end voltage to become higher than the sending end voltage [1.3,1.5]. This phenomenon is called the Ferranti Effect. Second, reactors are connected in series to reduce fault current in distribution lines. Reactors can be open-air coils or coils submerged in oil and are available in either single-phase or three-phase units. The shunt capacitor is employed for heavy load conditions to provide necessary reactive power support. Both shunt reactors and capacitors are connected to the system to adjust voltage levels, and are available as either capacitive or inductive alone or as a hybrid to provide both generation and absorption of reactive power [1.2].

Figure 1.1 shows the reactive power compensation schemes employed in the 132 kV, 275 kV, and 400 kV of the UK power system [1.6]. The chart shows that mechanically-switched capacitors (MSC) are the most popular reactive compensation method used in the UK system, in comparison to its counterparts such as the synchronous compensators (SC), the static Var compensators (SVC), and the reactors. Generally, the MSCs are applied to provide voltage support at the point of connection. MSC does not usually create any harmonics, but may interact with system harmonics. The additional capacitance added to any system by the adoption of a capacitor based solution, such as the MSC would have the effect of lowering the frequencies at which the system resonates. While this is not necessarily a problem, it can become an issue if the frequencies at which the system resonates coincide with those of harmonic sources on the system, frequencies occurring during the energisation and deenergisation of equipment on the system, or frequencies occurring during fault clearing.

In these cases, system resonance can result in equipment damage. Generally, solutions to these issues can be obtained through, firstly, means of switching transient suppression including Point-On-Wave (POW) switching and the use of pre-insertion resistor at the circuit breaker. Secondly, solutions can also be achieved by the application of appropriate rating of protective equipment, particularly surge arresters in the system. Thirdly, the solution to these issues can be obtained through the use of harmonic filtering techniques, such as the use of Mechanically Switched Capacitors with Detuning or Damping Networks (MSCDN), as opposed to Mechanically Switched Capacitor (MSC). The statistical data representing the MSCs shown in Figure 1.1 include those MSCs that are connected with its damping network for loss minimisation and harmonic control.

A mechanically-switched capacitor with damping network (MSCDN) is an advanced version of mechanically-switched capacitors (MSC), which were designed for use in harmonic-rich systems as it is insensitive to harmonics interaction [1.7, 1.8, 1.9]. MSCDN is mainly required to avoid harmonic resonance problems, which consequently could lead to unwanted voltage magnification [1.9]. In the MSCDN topology, capacitors are combined with air-core reactors, auxiliary capacitors, and shunt resistor to form a C-type filter circuit. The air-core reactor and the auxiliary capacitor are connected together to form a series LC branch, which is tuned to fundamental frequency for the purpose of loss minimisation.

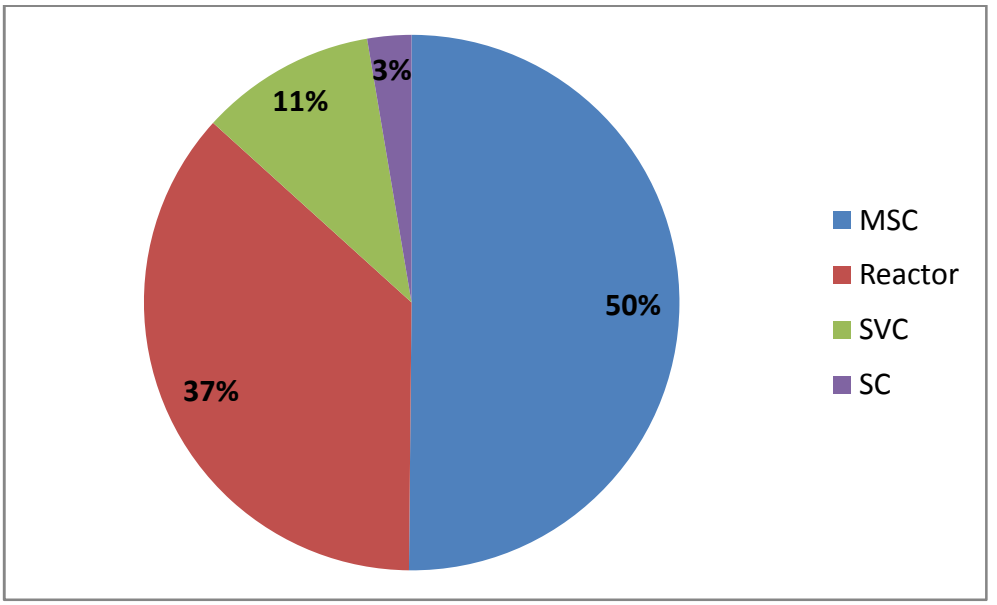

Figure 1.1: Reactive compensation equipment employed in the NGC system [1.6]

Depending on load variations, MSC/MSCDN and reactors are connected to and disconnected from the system using a circuit breaker. While the use of this reactive equipment helps maintain the voltage equilibrium of the connected system, their frequent switching operations render significant impacts. Disturbances in the form of transients are the problem of concern when switching the reactive equipment such as reactors and MSCs. The central causes of the problem are discussed as follows [1.10, 1.11].

i. Switching of capacitive current

Capacitive current are mostly encountered in four switching cases, such as switching of no-load overhead lines, switching of no-load cables, switching of capacitor banks, and switching of filter banks [1.10, 1.11, 1.12]. Closing operation of a circuit breaker performed in a dominantly capacitive network results in high inrush currents, which can cause problems for the protection system [1.13]. Furthermore, normal energisation of filter banks, particularly the lower order harmonic filters, can

generate overvoltage up to 4 p.u. across the filter capacitor, and 3 p.u for the filter reactor [1.12].

ii. Switching of inductive current

Switching of shunt reactors and unloaded transformers are two main cases of an inductive current switching [1.11]. Current interruption in a highly inductive circuit creates a problem due to current chopping phenomenon, during which the current is forced to zero before the natural current zero would occur. The high di/dt associated with current chopping results in high voltage induced in the inductive circuit [1.11]. A very specific inductive switching duty is the interruption of shunt reactor current. In the most onerous situation, a reignition occurs when the transient recovery voltage (TRV) exceeds the breakdown voltage of the circuit breaker [1.14]. Reignition overvoltage is undesirable as it causes non-uniform voltage distribution across the reactor winding [1.15, 1.16].

In a normal analysis, a stabilised condition of the circuit is assumed and steady-state values of current and voltage are sufficient. It often becomes important to know what happens during the transition period that occurs after a circuit disturbance but before the steady-state condition is reached. For that reason, transient studies are mostly required to address the problems above.

1.1 Aims and Objectives

The aims and objectives of this thesis are to identify and analyse the detrimental phenomena caused by switching operations of shunt reactors and mechanically-switched capacitor banks with damping network (MSCDN) in order to fulfil the intended function of steady-state voltage control. The studies are performed using ATP/EMTP software [1.17]. ATP/EMTP is the digital program simulation of

electromagnetic transients using time domain techniques. In the computation, ATP/EMTP employs the trapezoidal rule of integration to convert the differential equations of the network components into algebraics equations. In addition, mathematical modelling of the transients phenomena is also conducted analytically using the MATLAB and MathCAD programs [1.18].

In this thesis, analyses of transient overvoltage and/or overcurrent produced by shunt reactors and MSCDN switching operations are conducted separately. For that reason, the aims and objectives are specified separately for each study:

- **Shunt reactors transient studies**: The aim of these studies is to determine the resulting transient overvoltages produced by shunt reactor deenergisation, and to quantify the effect of transient overvoltage on the shunt reactor and the grading capacitors of the circuit breaker for different switching conditions.
- **Air-core reactor for MSCDN transient studies**: The aim of this investigation is to introduce, develop, and evaluate a detailed lumped parameter model of an air-core filter reactor for MSCDN using a simplified analytical approach. It should be emphasised that the main focus of this thesis is on transient voltage and transient current issues of the air-core reactor, as is extensively documented in this thesis. This study is conducted following the in-service failures associated with air-core reactors at transmission substations.

On this perspective, it is therefore very important to analyse the transient duties of the MSCDN and determine the effect of such stresses on all components, particularly the air-core filter reactor. The main objectives of this study are specified as:

- To quantify the effect of energising transient stresses produced at all MSCDN components.
- To establish a rigorous procedure for deriving a detailed equivalent circuit model of an air-core filter reactor for the MSCDN. Such a model could be further reduced or expanded if necessary and can be easily implemented in simulation software like ATP/EMTP.
- To establish a rigorous procedure for computing the average field strength on air-core reactor winding insulation using analytical equations.
- To evaluate the influence of key winding parameters on the impulse response of the air-core reactor.

1.2 Contribution of Present Work

The important contributions achieved during the course of this research work are as follows:

- Extensive review of important issues related to shunt reactor switching transients and research about implementation of associated techniques. This includes an appraisal of relevant standards for understanding transient phenomena that impact the circuit breaker grading capacitors due to shunt reactor switching (see Chapter 2).
- Extensive review of electrical stresses that impinge on a mechanically-switched capacitor with damping network (MSCDN) as a result of its switching operation. This includes a review of analytical and modelling techniques that were researched and implemented for the calculation of the transient duties of MSCDN components (see Chapter 2).

- Computation of overvoltages generated at the shunt reactor and the grading capacitor that are considered during the deenergisation process (see Chapter 3).
- Computation of overvoltages and overcurrents occurring at all of the MSCDN components that were considered during the energisation process (see Chapter 4).
- Derivation of a detailed equivalent circuit for an air-core reactor based on a lumped parameter model including the calculation of circuit parameters through new analytical equations (see Chapter 5).
- Computation of voltage distribution across the air-core reactor winding following the switching phenomena (see Chapter 5).
- New analysis of dielectric stresses for the calculation of average electric field strength on the reactor winding insulation through the derivation of analytical equations. This includes derivation of a new relationship between the maximum generated overvoltage and the main winding parameters (see Chapter 6).
- Analysis of the failure mechanism occurring in the air-core reactor of MSCDN due to switching; this includes a parametric analysis of the main winding parameters to determine the most influential parameters on the dielectric strength (see Chapter 6).

1.3 Thesis Content

Chapter 2 presents a critical review of the background information, modelling techniques, and calculation methods that are relevant to transient overvoltages and overcurrents due to switching operations. Given the studies carried out in this work,

the chapter content is divided into two sections that separately address the shunt reactor and the mechanically-switched capacitor with damping network (MSCDN). The review of shunt reactors covers the effect of transient overvoltages generated during the disconnection on the grading capacitor of a circuit breaker. Chapter 2 also presents an overview of transient duties associated with the MSCDN. In particular, it provides a critical review on the transient response of the air-core reactor that has been investigated and used by researchers and utilities around the world.

Chapter 3 details the computer simulation of shunt reactor switching transients, which demonstrates the deenergisation of a shunt reactor at various switching conditions. In addition, this chapter also presents analytical calculations of transient overvoltages carried out on the same shunt reactor.

Chapter 4 discusses transient duties of the MSCDN. In particular, it addresses a) the modelling procedures of MSCDN components including the surge arresters, b) the simulation of worst switching duties, and c) the possible improvements to the MSCDN representation particularly, the filter reactor model to be used in detailed transient studies.

Chapter 5 discusses the derivation of a detailed model of an air-core filter reactor and shows the calculation of lumped parameters of the reactor winding using an analytical approach. In addition, this chapter also presents simulations that are carried out on a detailed air-core reactor model.

Chapter 6 discusses possible failure mechanisms of an air-core filter reactor of an MSCDN due to non-uniform voltage distribution. In particular, it describes a) a new analysis of electric field strength based on a simplified approach, b) the investigation of dielectric capacitive current flow through the inter-turn insulation, and c) the

investigation of each of the winding parameters that influence the voltage distribution across the winding and the dielectric strength of the inter-turn insulation. Finally, chapter 7 contains the main conclusion of this work and suggests topics for further research.

The code of the MATLAB program used to calculate the lumped parameters of a detailed equivalent circuit of an air-core reactor is given in Appendix A.

The electrical properties of Mylar polyester film, which is the insulating material used for wrapping the air-core reactor winding conductors, is given in Appendix B.

Chapter 2: Switching Transients in Shunt Reactor and MSCDN Applications

In an electrical power system, passive reactive power compensation is provided by shunt capacitors and shunt reactors. Shunt capacitors are used for lagging power factor circuits, whereas reactors are used on systems with leading power factors. In both cases, the effect is to provide reactive power support that maintains the voltage limits in the system. This chapter presents a literature review of findings pertinent to this research. Section 2.1 presents a review of shunt reactors' applications for compensating the reactive power in an electrical system. Transient phenomena related to the switching operation of shunt reactors are presented in Section 2.2. A. The review about MSCDN applications in a power system is presented in Section 2.3. Next, section 2.4 presents a discussion about air-core reactors used in the MSCDN system; transient stresses on air-core reactors due to MSCDN switching is also included in this section. Finally, the chapter summary is provided in Section 2.5.

2.1 Shunt Reactors

As defined in the BS60076-8 and IEEE C37.015 [2.1, 2.2], the term 'shunt reactors' refers to reactors that are intended for phase-to-earth, phase-to-neutral or between-phases connections in a power system in order to compensate for capacitive current.

The need for shunt inductive compensation is mainly due to the large inherent capacitance of lightly-loaded transmission systems, which draw a substantial quantity of charging current [2.3]. When such a line is open-circuited or very lightly loaded at the receiving end, the flow of leading capacitive charging current through the inductance of the line and the system causes the operating voltage to increase

with increased distance along the line [2.3]. This phenomenon is referred to as Ferranti effect, which is classified as a temporary overvoltage (TOV) [2.3]. The provision of a shunt reactor tends to reduce the leading capacitive charging current of the line and thus reduces the voltage rise [2.3]. Another TOV phenomenon is ferroresonance, which is the interaction of line capacitance with any saturable portion of system inductive reactance. One example of ferroresonance is in the switching of the transformer terminated line, where the voltage at the end of the line may increase to a value that is sufficient to saturate the transformer inductance [2.3, 2.4]. The interaction between this inductance and the capacitance of the line can generate harmonics, causing overvoltages [2.3,2.4]. In such a case, the application of a shunt reactor connected to the tertiary winding of the transformer is used to mitigate the generated overvoltage.

2.1.1 Classification of the Shunt Reactor

Figure 2.1 shows the classification of shunt reactors according to applications and design. Generally, there are two kinds of shunt reactors: dry-type reactors and oil-insulated type reactors [2.3,2.4]. Oil-immersed shunt reactors with an air-gapped iron core are widely used in transmission systems [2.5]. For this type of reactor, the main winding and the magnetic circuit are immersed in oil. The insulation oil acts as the cooling medium, which can both absorb heat from the reactor winding and conduct the heat away by circulating the oil [2.5]. The core of an oil-immersed reactor is made of ferromagnetic materials, with one or more built-in air gaps. These air-gapped iron cores are designed to resist not only the mechanical stresses during normal operation but also withstand the fault conditions in the network [2.5].

The characteristic and design construction of shunt reactors are more dependent on the applied voltage. In the UK, 400 kV and 275 kV are referred to as transmission voltage network, whilst the distribution voltages are 132 kV, 33 kV, 11 kV, and 400 V. According to IEEE C37.015 [2.2], the design of shunt reactors rated 60 kV to 245 kV is most commonly oil-filled and have three-legged gapped cores with layer, continuous disc or interleaved disc windings. At 300 kV to 500 kV, the design of shunt reactors can be single-phase or three-phase units with three-legged, five-legged or shell-type cores. For shunt reactors rated below 60 kV, the design is either oil-filled, three-legged iron core types or dry coil types.

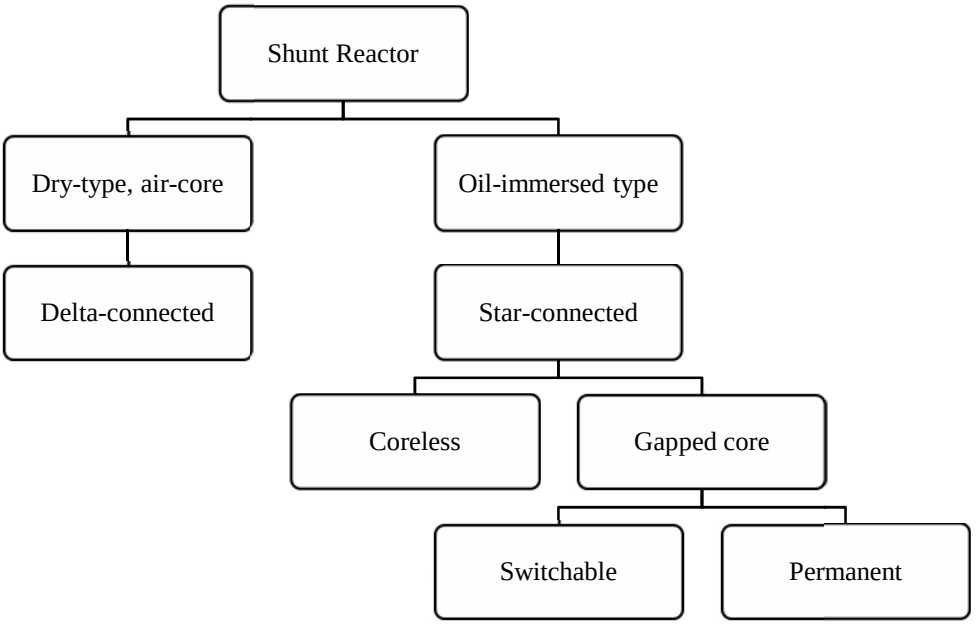

Figure 2.1: Classification of shunt reactors [2.3]

Depending on the intended function, a shunt reactor can be designed to have either linear or adjustable inductances [2.3]. As the name implies, linear shunt reactors have constant inductance within the specified tolerances [2.3]. Conversely, a shunt reactor in which the inductance can be adjusted by changing the number of turns on the winding or by varying the air gap in the iron core is called an adjustable shunt

reactor [2.3]. The number of turns on a winding is changed by means of a tap changer. The service conditions are vital to the design and structure of the shunt reactor. For oil-immersed shunt reactors, the ambient temperatures are usually specified within the range of -25°C to 40°C [2.1]. Exceeding the specified ambient temperature may reduce both the reliability and the life of the shunt reactor. The shunt reactor is installed in a three-phase system as either a three-phase shunt reactor or three single-phase shunt reactors. Generally, single-phase shunt reactors are favoured over three-phase shunt reactors due to cost benefits and transport restrictions. Each reactor has specific ratings in the form of minimum specifications, as indicated in Table 2.1 [2.1, 2.5].

Table 2.1: Recommended entries on the reactor rating plate as per [2.1]

No.	Items	Remarks
1.	Type of reactor	
2.	Outdoor/Indoor application	
3.	Number of relevance part of IEC 60076	
4.	Manufacturer's name	
5.	Manufacturer's serial number	
6.	Year of manufacture	
7.	Insulation level (s)	
8.	Number of phases	
9.	Rated power	for tapped reactors, the power on each tapping position
10.	Rated frequency	
11.	Rated voltage	
12.	Rated current	
13.	Maximum operating voltage	
14.	Winding connection	where applicable
15.	Reactance at rated voltage and frequency or inductance at rated voltage	measured value
16.	Type of cooling	
17.	Thermal class of insulation	for dry-type reactors only
18.	Temperature rise of top-oil and average winding	for liquid-immersed reactors only
19.	Total mass	
20.	Transportation mass	for liquid-immersed reactors
21.	Untanking mass	where applicable
22.	Type of insulating liquid, if not mineral oil	where applicable

23.	Connection diagram showing tappings and instrument transformers	where applicable
24.	Zero-sequence reactance, measured value	where applicable on request
25.	Mutual reactance, measured value	where applicable on request

2.1.2 Shunt Reactor Rating

Figure 2.2 shows typical connections of shunt reactors within electrical networks [2.3]. Shunt reactor rating is given in terms of rated power (MVar) and the rated voltage.

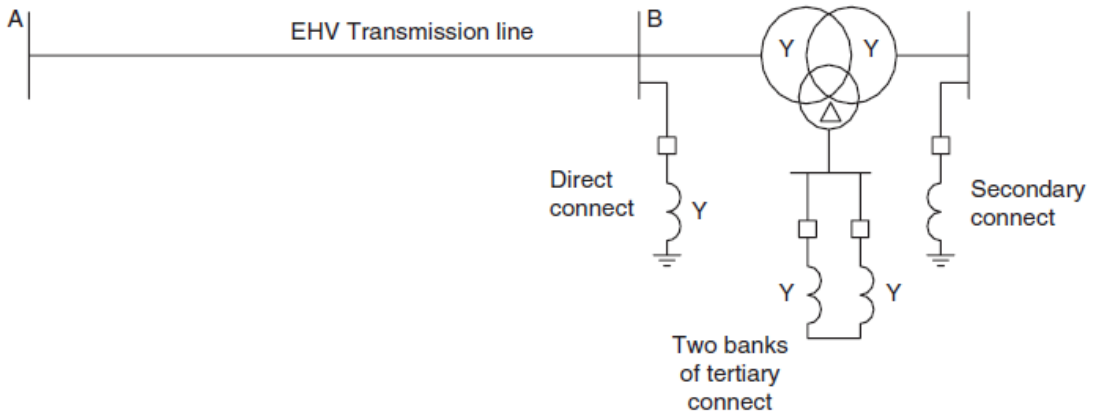

Figure 2.2: Typical connections of shunt reactors [2.3]

For system voltages below 60 kV, shunt reactors may be inserted into the system through a tertiary winding of a power transformer connected to the overhead line that is being compensated [2.6]. Tertiary-connected shunt reactors are of dry-type, air-core, single-phase per unit construction, or oil-immersed and three- or single-phase per unit construction [2.6]. At system voltages of 60 kV and above, shunt reactors are normally connected directly to the high-voltage busbar or transmission line that is to be compensated [2.6]. These shunt reactors have a power rating between 30 and 300 MVar (three-phase). Shunt reactors that are directly connected to the system are

usually of oil-immersed type [2.6]. This direct connection to overhead line is made either at the end of the line or at an intermediate point, depending on voltage profile considerations.

Ching-Yin, et al. [2.7] explored transient phenomena concerning the switching of shunt reactors installed on the line's two terminals and the station busbar. In the investigated studies, the shunt reactors are planned to be installed on the underground transmission system, which consists of a dual-circuit 345 kV tie-line connecting two different stations. The distance between the two locations is 20 km and the line charging of the cable is about 800 MVar. Two compensation schemes were considered: First, a shunt reactor with 25% (200 MVar) compensation is connected at each end of 345 kV dual-lines four terminals. Second, a fixed shunt reactor with 100% (800 MVar) compensation is installed at 161 kV station busbar on the receiving-end. The results obtained from these two cases were compared based on the improvement made on the high capacitive effect of the XLPE cables after the compensation. Based on the simulation conducted, transient overvoltage during deenergisation produced at the shunt reactor installed at the 161 kV station busbar is higher than the overvoltage generated at the shunt reactor installed at the 345 kV line's two terminals. It was also reported that the provision of shunt reactors at the 345 kV line's two terminals greatly improve the maximum overvoltage produced at the lines due to Ferranti effect. In the following sections, determination of the power rating of direct-connected shunt reactors is discussed.

2.1.2.1 Shunt Reactor Connected to the Busbar

Figure 2.3 shows a practical circuit used for simplified voltage control analysis in an electrical system. Upon the connection and disconnection of the shunt reactor,

voltage variation at the high-voltage busbar should not be higher than 2-3% of the rated voltage [2.6]. The reactor rating should be chosen to limit the magnitude of the voltage step change that occurs during a routine switching operation.

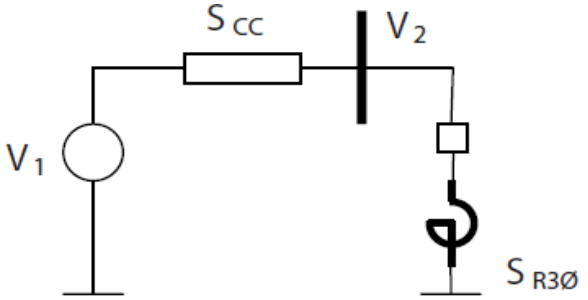

Figure 2.3: Circuit for voltage control analysis [2.6]

The voltage sensitivity to changes at one busbar (i) due to small changes in real and reactive power at another busbar (j) is provided as in Equation (2.1).

$$dV_i = \frac{\partial V_{ij}}{\partial P} dP_j + \frac{\partial V_{ij}}{\partial Q} dQ_j \qquad (2.1)$$

Evaluation of Equation (2.1) requires a complete load flow analysis, which involves complicated procedures. A simplified equation that is quite accurate in most cases is given, as in Equation (2.2) [2.6].

$$\Delta V_i = \frac{\Delta Q_i}{S_{cc}} \quad \Rightarrow \quad Q_i = \Delta V_i \times S_{cc} \qquad (2.2)$$

Equation (2.2) renders the required reactive power of the shunt reactor in terms of the short-circuit level (S_{cc}) at the busbar, where the reactor will be connected. For the system shown in Figure 2.3, Equation (2.2) can be rewritten as follows [2.6]:

$$S_{R3\emptyset} = S_{cc}\left(\frac{V_1 - V_2}{V_2}\right) \qquad (2.3)$$

where, V_1 is the maximum bus voltage and V_2 is the acceptable bus voltage that should be maintained in the system. $S_{R3\phi}$ represents the required inductive power of the shunt reactor necessary to reduce the voltage level from voltage V_1 to voltage V_2. It is noted that the power rating of the shunt reactor is merely dependent on the specified voltage limits and the short-circuit level of the compensated system [2.6]. Once the power rating is known, other shunt reactor parameters can be calculated subsequently through simple mathematical manipulation, as shown in Table 2.2 [2.6]. Important formulae are given for calculating the reactance, the rated current, and the maximum continuous current of the shunt reactor based on known parameters of rated voltage and rated frequency.

Table 2.2: Calculation of shunt reactor parameters [2.6]

Parameters	Star-connected	Delta-connected
Reactance	$X = \frac{U_N^2}{S_{R3\emptyset}} = \frac{U_N^2}{3 \times S_{R1\emptyset}}$	$X = 3 \times \frac{U_N^2}{S_{R3\emptyset}} = \frac{U_N^2}{S_{R1\emptyset}}$
Rated Current	$I_N = \frac{S_{R3\emptyset}}{\sqrt{3} \times U_N} = \frac{S_{R1\emptyset}}{U_N / \sqrt{3}} = \frac{U_N}{\sqrt{3} \times X_R}$	$I_N = \frac{S_{R3\emptyset}}{3 \times U_N} = \frac{S_{R1\emptyset}}{U_N} = \frac{U_N}{X_R}$
Maximum continuous current	$I_{max} = \frac{U_{max}}{U_N} \times I_N$	$I_{max} = \frac{U_{max}}{U_N} \times I_N$

where:

X rated reactance per phase (positive sequence) (Ω)

$S_{R3\phi}$ rated three-phase reactive power (MVA)

$S_{R1\phi}$ rated reactive power per-phase (MVA)

U_N rated system voltage (V)

U_{max} maximum system operating voltage (V)

I_N rated current (A)

I_{max} maximum continuous current (A)

2.1.2.2 Shunt Reactor Connected to the Transmission Lines

For the shunt reactor installed at the line terminals, the power rating calculation is performed by considering the lossless radial transmission line, where the line is energised by a generator at the sending end (V_1) and is open-circuited at the receiving end (V_2). The matrix representation provided by the ABCD parameters, where I_2=0 is expressed as in Equation (2.4) [2.6]:

$$\begin{bmatrix} V_1 \\ I_1 \end{bmatrix} = \begin{bmatrix} A & B \\ C & D \end{bmatrix} \times \begin{bmatrix} V_2 \\ I_2 \end{bmatrix} \tag{2.4}$$

Simplifying Equation 2.4 yields the following [2.6]:

$$V_1 = A \cdot V_2 = \left(1 + \frac{ZY}{2}\right) \cdot V_2 \tag{2.5}$$

For voltage control purposes, the shunt reactor is required and inserted at the receiving end to absorb the reactive power, resulting in modified ABCD parameters of the line, as presented in Equation (2.6) [2.6].

$$\begin{bmatrix} V_1 \\ I_1 \end{bmatrix} = \begin{bmatrix} A & B \\ C & D \end{bmatrix} \times \begin{bmatrix} 0 & 0 \\ \frac{1}{X} & 0 \end{bmatrix} \times \begin{bmatrix} V_2 \\ I_2 \end{bmatrix} \Rightarrow \begin{bmatrix} V_1 \\ I_1 \end{bmatrix} = \begin{bmatrix} A' & B' \\ C' & D' \end{bmatrix} \times \begin{bmatrix} V_2 \\ I_2 \end{bmatrix} \tag{2.6}$$

Subsequently, a new relationship is obtained between the voltages V_1 and V_2 of the line and is given as:

$$V_1 = A' \cdot V_2 \Rightarrow \quad V_1 = \left(A + \frac{B}{X}\right) \cdot V_2 \Rightarrow \quad V_1 = \left(1 + \frac{ZY}{2} + \frac{L_{line}}{L}\right) \cdot V_2 \tag{2.7}$$

By comparing Equations (2.5) and (2.7), it is noted that a new term of the inductance L resulting from shunt reactor installation is added to the operating voltage.

2.2 Shunt Reactors Switching Transients

Transients caused by switching of high voltage shunt reactors are well known. Failures of shunt reactors during service operations received significant attention in recent years via numerous technical papers and guides from the power community. The reasons for the shunt reactor failures are now well-understood and physically explained; adequate precautions to avoid such failures or at least reduce the probability of their occurrence are now available [2.8].

Shunt reactors are typically connected and disconnected at least once per day, and this sometimes occurs even more frequently depending on the power system loading patterns. Whenever the bus voltage rises to 4-5% more than the rated voltage, a shunt reactor is switched in to the system [2.6]. Shunt reactors may be kept out of service when the bus voltage is 2-3% less than the rated value [2.6]. Consequently, frequent switching becomes an important characteristic of the shunt reactors. The switching routines are performed by the circuit breaker, which are most often modern SF6 or air-blast types [2.8].

2.2.1 Transients during Energisation

When the reactor is connected to the network, there is a transient condition; the main problems associated with such transients are high inrush currents. Numerous research papers explain the problems associated with shunt reactor energising transients [2.9, 2.10, 2.11]. The magnitude of inrush current depends on the instant of the switching and the linearity of the reactor core [2.1]. Depending on the frequency and point on the voltage wave at which the reactor is connected to the network, an inrush current may be experienced with a peak value that is higher than the peak value of the rated current [2.1, 2.8].

Current asymmetry is smaller if the energisation occurred at or near the maximum supply voltage, whereas the current asymmetry is larger if the reactor is energised at the zero crossing of the voltage wave [2.8]. The latter is the worst energising transient, in which the linked flux produced is about twice the steady-state value. For a reactor with linear magnetic characteristic, the resulting inrush current peak can reach approximately twice the peak value of the steady-state current. For reactors with a non-linear magnetic characteristic, the inrush current peak can attain more than twice the peak of the steady-state current [2.1, 2.8].

The damping of this inrush current is mainly determined by the reactor winding losses, assuming that the power system has a small resistive component [2.1]. Without optimum switching, the DC component of the current will take many cycles to decay due to low system resistance and the high Q factor of the reactor. Mechanical vibrations with excessive electromagnetic stresses in the reactor winding and malfunction of protective relays are two common problems that result from inrush currents [2.5]. In practice, however, a high-magnitude inrush current caused by closing operations at an unfavourable instant can be avoided by the application of controlled switching [2.12]. In this case, an optimum switching point is specified at the peak of the power frequency voltage. While the closing operation made at the peak of the supply voltage can reduce the inrush current magnitude, this may create another problem associated with transient overvoltage of steep rise time [2.12]. This overvoltage is mainly caused by circuit breaker prestrikes during the energisation of the shunt reactor.

According to IEEE C37.015 [2.5], for directly grounded reactors, the breakdown voltage across the circuit breaker due to prestriking will not exceed 1 p.u., and the

peak value of the energising transient is usually around 1.5 p.u. or less. This value is acceptable with regards to the equipment insulation [2.5]. In this thesis, transients due to reactor energisation were not analysed, as it was considered that possible high inrush currents would be avoided by the application of closing controlled switching.

2.2.2 Transients during Deenergisation

Shunt reactor load currents are referred to generically as small inductive currents [2.5]. In general, the capability of circuit breakers to interrupt this current is not a concern. Nevertheless, it is particularly when disconnecting the reactor from the system that severe overvoltage may arise. This problem occurs because the circuit breaker tends to break the currents too quickly, which results in the current being prematurely forced to zero before its prospective zero crossing, a phenomenon referred to as current chopping [2.2, 2.5, 2.13, 2.14]. Following current interruption, the generation of significant transient overvoltage, specifically the following two types can be expected in the shunt reactor circuit [2.5]:

- Chopping overvoltages with oscillating frequencies up to 5 kHz
- Reignition overvoltages with frequencies up to several hundred kHz

These overvoltages can be described based on a single-phase equivalent circuit of the shunt reactor, as shown in Figure 2.4. In this case, each phase can be considered independently of the other two, since the zero-sequence and the positive-sequence reactances are equal (X_o=X_1), and the interaction between phases for star-connected, solidly-earthed neutral, three-phase reactors can be ignored [2.5, 2.15].

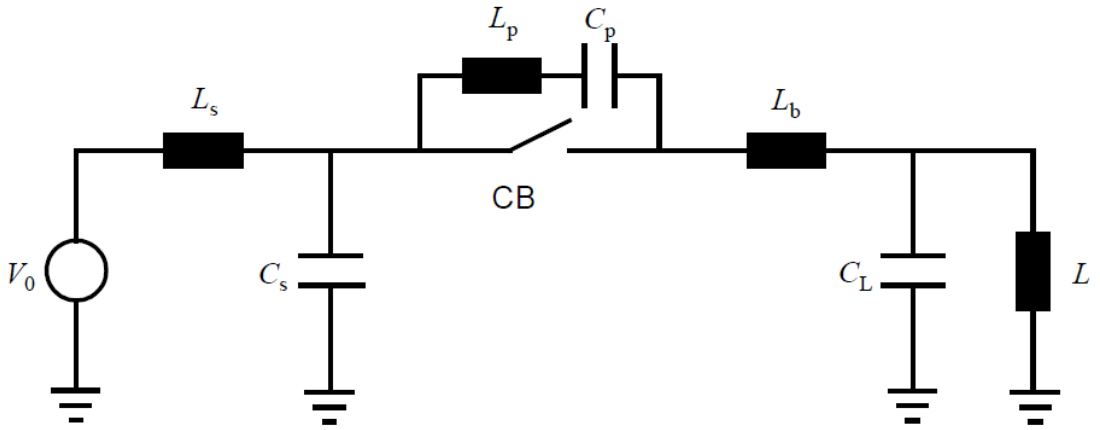

Figure 2.4: Single-phase equivalent circuit for analysing shunt reactor switching [2.5]

where:

V_o source voltage

L_s source side inductance

C_s source side capacitance

CB circuit breaker

L_p,C_p stray capacitance and inductance of the CB

L_b buswork inductance

C_L load side capacitance

L shunt reactor inductance

i. Current Chopping and Chopping Overvoltage

The current chopping phenomenon is caused by arc instability [2.8]. For shunt reactor switching, the current chopping is dependent mainly on the type of circuit breaker, the arcing time, and the circuit involved [2.5]. The chopped current level increases with the increased number of chambers per interrupting pole, which is the characteristic of a circuit breaker [2.5]. Furthermore, the equivalent capacitance (C_t) seen from the circuit breaker terminals also influences the current chopping magnitude. Referring to the circuit shown in Figure 2.4 above, the equivalent

capacitance viewed from the circuit breaker terminals is provided in Equation (2.8) [2.5].

$$C_t = C_p + \frac{C_s C_L}{C_s + C_L} \quad (2.8)$$

The capacitance C_L is the effective load side capacitance-to-ground, and is given by Equation (2.9) [2.5],

$$C_L = C_g + 2C_{\emptyset} \quad (2.9)$$

where, C_g is the summation of capacitances-to-ground of the load-side equipment and $C_{\emptyset}$ is the phase-to-phase capacitance of the shunt reactor and its associated connections. For many cases, the capacitance $C_{\emptyset}$ may not be significant compared to C_g, and can be safely ignored. Accordingly, a relationship of the current chopping level, the equivalent capacitance, and the circuit breaker is provided as in Equation (2.10) [2.5]:

$$i_{ch} = \lambda\sqrt{NC_t} \quad (2.10)$$

where

i_{ch} the current level at the instant of chopping (A)

C_t the equivalent capacitance in parallel with the circuit breaker (F)

λ the chopping number for N interrupter ($AF^{-0.5}$)

The chopping number (λ) in Equation (2.10) is a unique characteristic that belongs to a circuit breaker. Table 2.3 provides typical chopping number (λ) for selected circuit breaker types.

Table 2.2: Circuit breaker chopping numbers [2.5]

Circuit breaker type	Chopping number (λ)
Minimum oil	7-10x10^4
Air blast	15-25x10^4
SF6	4-17x10^4

The overvoltage resulting from the current chopping phenomenon is called chopping overvoltage. The magnitude of the chopping overvoltage can be calculated by observing the energy balance at the load side circuit, following the circuit breaker current interruption [2.8, 2.12]. The energy trapped in the load-side inductance and capacitance at the instant of current chopping will oscillate between the inductance and the capacitance associated with the shunt reactor [2.8]. This can be expressed as in Equation (2.11) [2.8]:

$$\frac{1}{2}Li_{ch}^2 \Rightarrow \frac{1}{2}C_L V_m^2 \tag{2.11}$$

where,

L inductance of the reactor

i_{ch} current chopping level

C_L effective capacitance (including the reactor) at the circuit breaker's load side

V_m voltage across the effective capacitance

Equation (2.11) reflects that the magnetic energy in the reactor is transformed to the electrostatic energy in the capacitance, as a result of switching operation. Rearranging Equation (2.11), the voltage magnitude at the reactor terminal just after the disconnection is obtained as [2.8]:

$$V_m = i_{ch}\sqrt{\frac{L}{C_L}} \tag{2.12}$$

The chopping overvoltage will oscillate due to the energy exchange that occurs between the stray capacitance and the inductance of the reactor [2.8]. This oscillation will be damped due to the inherent resistances of the reactor and the circuit. A typical course of the chopping overvoltage across the reactor is shown in Figure 2.5 [2.16]. The values of the chopping overvoltage are in the range of 1.2-2.0 p.u. for widely-used SF_6 circuit breakers [2.48]. Due to the comparatively low frequency of oscillation, the rate-of-rise of the chopping overvoltage is relatively moderate so, this voltage is harmless to the reactor and the surroundings [2.5].

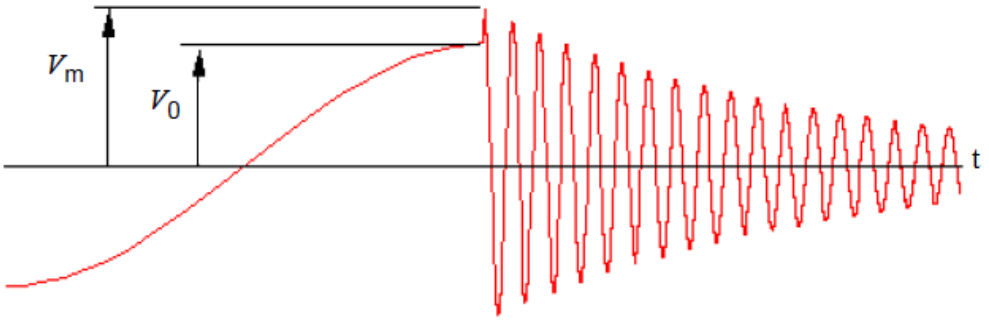

Figure 2.5: Typical waveform of chopping overvoltage [2.16]

ii. Reignition Overvoltage

Usually, when breaking at a low level of highly-reactive currents, the circuit breaker arc is weak because the current is not large [2.8]. This means that the contacts of a circuit breaker are not far apart when the arc extinguishes. If the interruption was made at current zero, as in most of the switching cases, the system voltage is near its peak; thus, the recovery voltage between the circuit breaker contacts can be large [2.8]. Figure 2.6 illustrates a typical TRV waveform measured across the circuit breaker contacts after the current interruption [2.16].

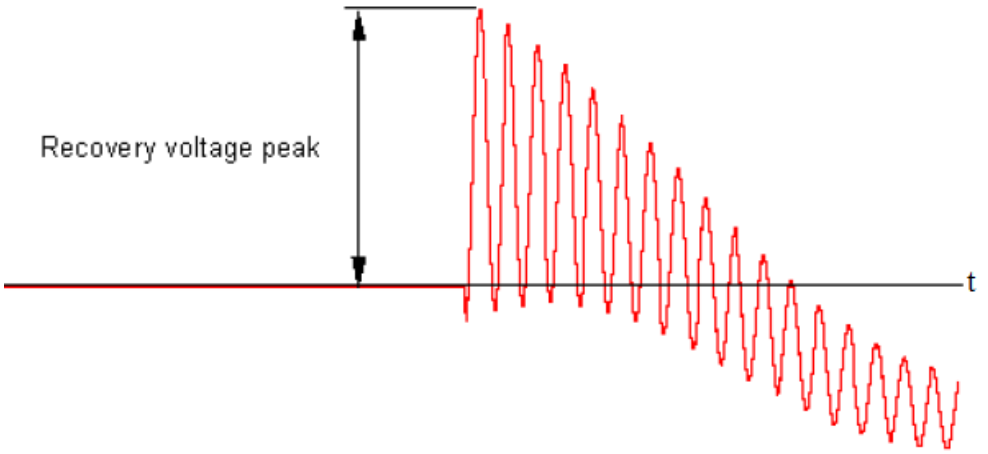

Figure 2.6: Typical waveform of transient recovery voltage (TRV) across the circuit breaker [2.16]

Severe problems may occur when the circuit breaker cannot withstand the transient recovery voltage (TRV) across its open contacts. Depending on the circuit breaker capability, the TRV that exceeds the dielectric strength of the residual column of that circuit breaker will create a dangerous transient caused by reignition [2.5]. Reignition overvoltage is described as steep voltage transients, having the front rise time in a range of one microsecond to several microseconds. Such a voltage can cause non-uniform voltage distribution across the reactor winding [2.5]. The reignition overvoltage depends mainly on the network configuration and the circuit breaker characteristics [2.5]. Figure 2.7 shows a typical voltage course on the reactor terminal when a reignition in the circuit breaker occurs [2.16].

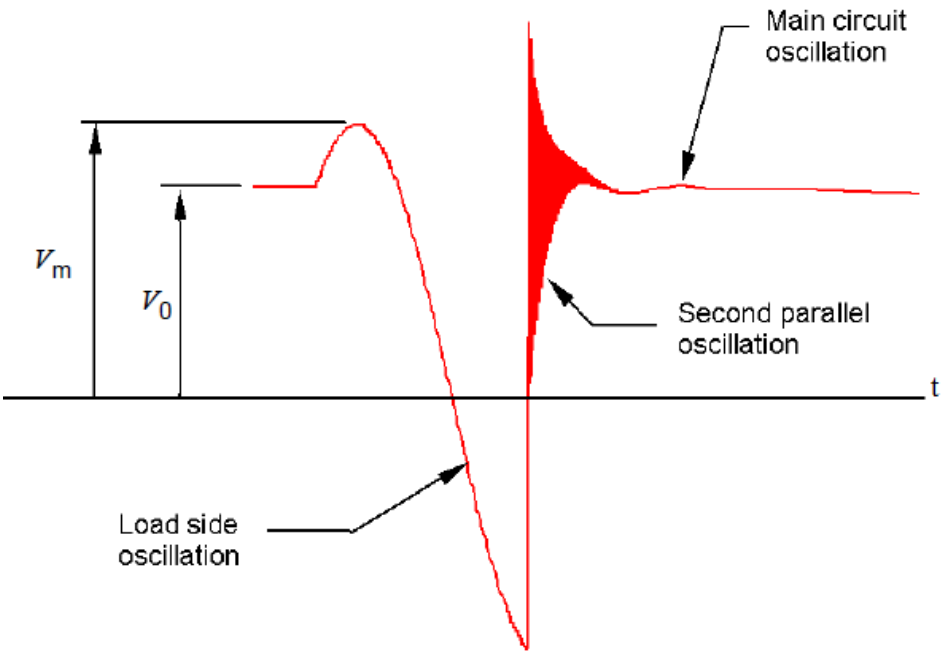

Figure 2.7: Typical waveform of reignition overvoltage [2.16]

Table 2.4 shows the reignition overvoltages obtained when disconnecting two shunt reactors of different power rating [2.12]. As shown, the resulting transient overvoltages are inversely proportional to the shunt reactor rated power. Based on the simulation conducted, the overvoltage magnitudes obtained for a 100 MVar shunt reactor was higher, than those obtained for a 150 MVar shunt reactor [2.12]. Overvoltages produced when disconnecting a 100 Mvar reactor in a 400 kV system reached up to 2.05 p.u. when the surge arrester was not connected [2.12]. The magnitude obtained for a 150 MVar shunt reactor was 1.67 p.u. when the disconnection was made without the surge arrester [2.12]. Besides the voltage magnitude, the effect of shunt reactor deenergisation is also evaluated in terms of voltage steepness [2.12]. It was shown that the surge arrester installed across the shunt reactor is capable of reducing the overvoltage magnitude; however it has no significant influence on the voltage steepness [2.12].

Table 2.4: Simulation results of shunt reactor deenergising transient [2.12]

Reactor	Surge arrester	Umax (kV)	Sav (kV/µs)
100 MVar	No	703.5	1322
100 MVar	Yes	654.8	1320
150 MVar	No	666.6	1159
150 MVar	Yes	632.7	1155

Prikler, et. al. [2.17] carried out a comprehensive analysis to determine the effect of non-uniform voltage distribution across the shunt reactor winding. The comprehensive model is developed based on an n-part inductively coupled element of EMTP. Such a model was obtained considering both self and mutual inductances of the reactor winding as shown in Figure 2.8. Moreover, shunt and series capacitances and resistances representing the losses to each of them are also considered [2.17]. This model is suitable for analysing the response of shunt reactor winding to the steep reignition voltage generated during deenergising transient.

Figure 2.9 shows the computed voltage gradients between neighbouring part-windings obtained using this model. It is shown that the first tenth of the winding closest to the high voltage terminal was overstressed with 17% of the reactor voltage [2.17].

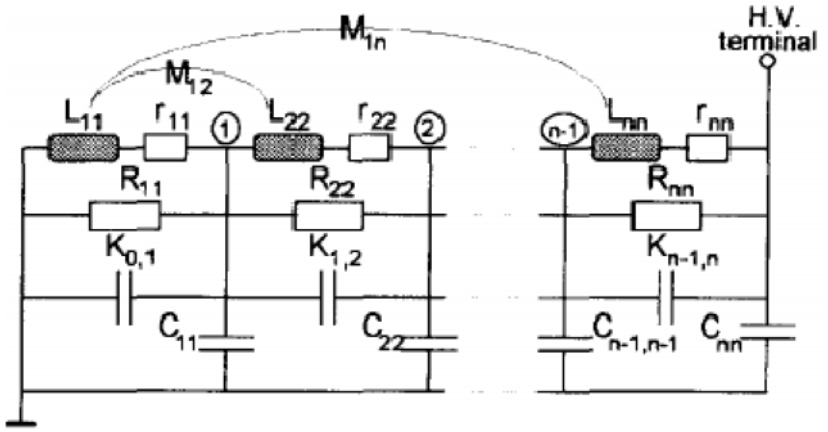

Figure 2.8: Detailed model of a shunt reactor [2.17]

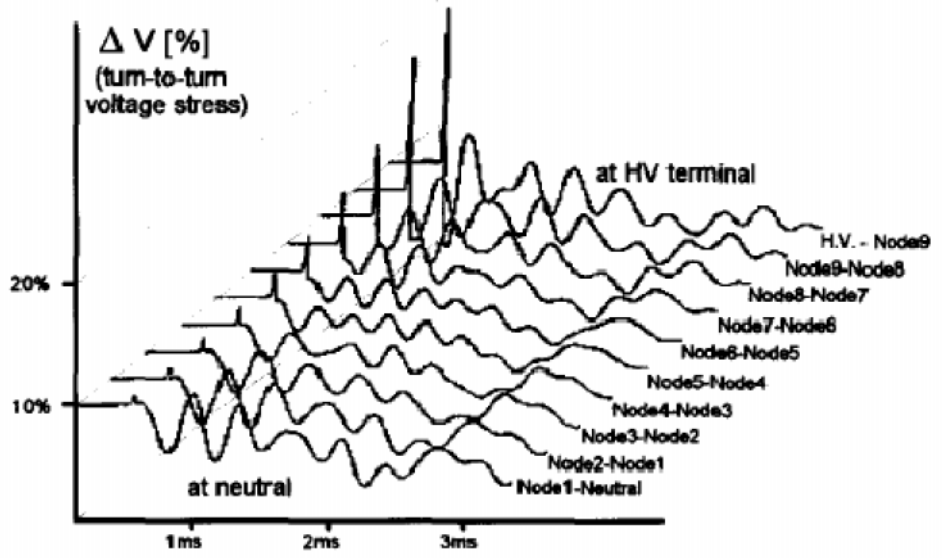

Figure 2.9: Typical voltage gradients between part-windings calculated using a detailed reactor model [2.17]

Various techniques have been developed to control the occurrence of the reignitions in the circuit breakers. One of the methods used and is applicable to the shunt reactor switching is known as the point-on-wave (POW) technique [2.12, 2.18, 2.17, 2.18]. POW ensures that the contacts of a circuit breaker are well-separated from each other before the current is interrupted, and thus reducing the probability of reignition occurrences. Figure 2.10 illustrates a simple control mechanism employed in the

POW method. It mainly involves specifying the right time on the rising part of the current waveform for the contact to start separating from each other [2.8]. The use of surge arresters can further improve the overvoltage magnitudes generated during shunt reactor switching [2.18, 2.19].

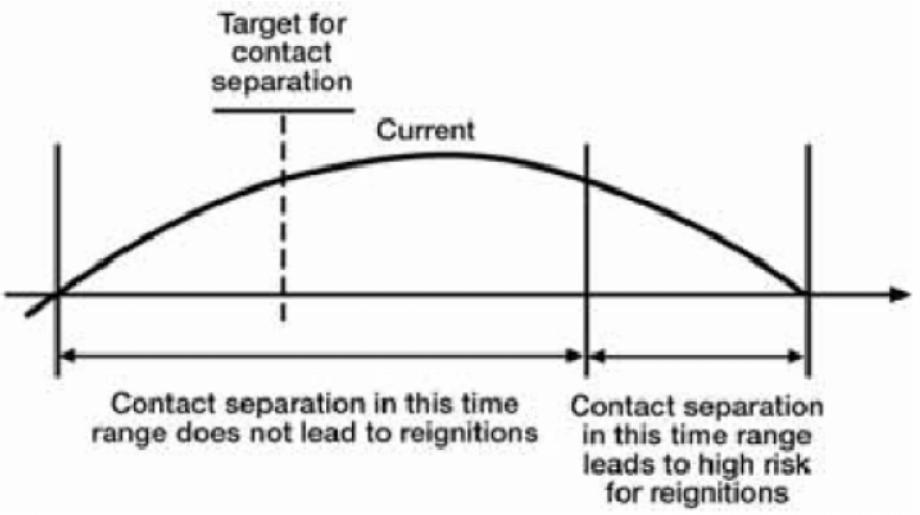

Figure 2.10: Principle of point-on-wave (POW) controlled switching [2.8]

2.2.3 Transient Stresses in a Grading Capacitor of the Circuit Breaker

In this thesis, the transient studies related to shunt reactor disconnection were carried out with two main purposes. The first one was to determine the overvoltages produced by the shunt reactor switching. There are two significant overvoltages that resulted from the shunt reactor disconnection: chopping overvoltage and reignition overvoltage. The second objective was to determine the stresses imposed on the grading capacitors of the circuit breaker as a result of shunt reactor switching. Figure 2.11 shows an image of grading capacitors, which are mounted in parallel with each chamber of a circuit breaker [2.16]. Voltage grading capacitors are accessories for high-voltage circuit breakers that are used to provide equal voltage distribution

across each interrupting chamber of multi-unit circuit breakers [2.16]. They are chiefly employed for circuit breakers in high voltage system e.g. at 400 kV.

Figure 2.11: Example of two-unit circuit breaker with grading capacitors [2.16]

During their service life, a number of disruptive dielectric failures have occurred on both gas insulated substation (GIS) and air insulated substation (AIS) [2.16]. Most of the reported cases involved the circuit breakers that had been switching low inductive current associated with shunt reactors [2.20, 2.21]. It was found that the grading capacitors failed on or shortly after the circuit breaker opening operation, which is caused by unexpected dielectric stresses [2.20, 2.21]. In order to investigate the electrical stresses on the grading capacitor, the circuit breaker is modelled based on an equivalent circuit shown in Figure 2.12 [2.16]. The voltage sharing across the interrupters of an open circuit breaker is determined by the grading capacitors, C_{p1}

and C_{p2}, as well as the stray capacitances, especially the stray capacitance-to-ground, C_e [2.21].

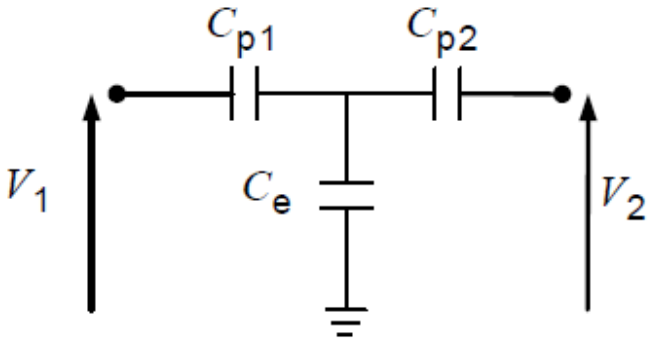

Figure 2.12: Equivalent circuit of circuit breakers with two interrupters per pole [2.16]

Under dynamic conditions, such as during the occurrence of reignition, the grading capacitors (C_{p1} and C_{p2}) are subjected to greater differences in the voltage stresses [2.21]. According to the simulation conducted in [2.21], if the source side interrupter reignites before the load side interrupter, the voltage across the load side grading capacitor increases up to 2.34 times the source voltage. Likewise, when the load side interrupter reignites before the source side interrupter, the voltage across the source side grading increases up to 2.39 times the source voltage within about 300 ns after the reignition occurs [2.21]. It was shown that when the circuit breaker is in an open position to disconnect the shunt reactor, the voltage stresses impressed on the grading capacitors can reach more than two times the peak value of the source voltage [2.20, 2.21]. As shunt reactor switching is typically performed on a daily basis, the grading capacitors will be exposed to the associated stresses hundreds of times per year [2.20, 2.21].

2.3 Mechanically-Switched Capacitor with Damping Network (MSCDN)

Following the privatisation of the Electricity Supply Industry in England and Wales in 1990, generation and transmission were unbundled into separate investor-owned companies [2.22]. The biggest of these companies is the National Grid Company plc. (NGC), which owns the 400 kV and 275 kV transmission systems. As a result of the deregulation, NGC does not control the establishment of new generating stations or the closures of existing generating stations [2.22]. The planning and system development process must be able to respond to changing system patterns and network topologies within tight timescales.

Nevertheless, the reactive power balance and voltage control must be maintained, to ensure that the security and quality standards of the system [2.23]. NGC has found it most practicable to increase the use of mechanically-switched capacitors (MSCs) and static Var compensators (SVCs) for this task [2.23]. MSCs are primarily employed for steady-state voltage control. The requirements for installing MSCs on 400 kV and 275 kV substations within the UK power system are threefold [2.23]. First, MSCs must be capable of relocation to other substations when needed. They should be ready for operation within three months of deenergisation at the original site [2.23]. Second, the MSCs must have minimum losses at fundamental frequency; an important criteria that should be accounted for during the design stage of MSCs. This requirement is imposed based on the high rate of loss capitalisation at the fundamental frequency, which is estimated at £2700/kW [2.23, 2.24]. Third, as the MSC is normally used in the system with significant harmonic problems, it is required that the installation of MSCs should not worsen the existing harmonic distortion [2.23]. This requirement is in accordance with an upward trend in pre-

existing harmonic levels, particularly at 3rd, 5th, and 7th harmonics [2.23]. According to MacLeod, et. al. [2.23], harmonic benchmarking exercise conducted at nearly 50 substations at both 400 kV and 275 kV in the UK confirms a general increase in magnitudes of pre-existing harmonic distortion. This is mainly due to the changing nature of the loads connected at lower voltage, particularly the proliferation of consumer electronic equipment containing non-linear power supplies [2.23].

Amplification of pre-existing harmonics in a network can be explained using the circuit presented in Figure 2.13 [2.23]. This circuit shows the pre-existing harmonic distortion represented as an ideal voltage source (V_o) behind the system harmonic impedance (Z_{sn}) [2.23].

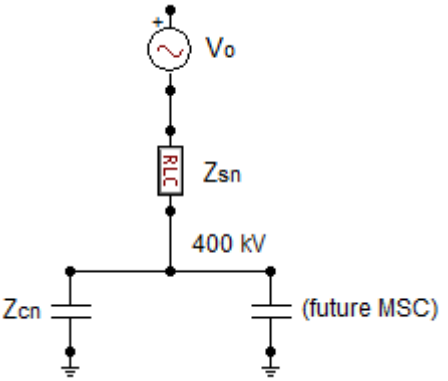

Figure 2.13: System representation with capacitor banks [2.16]

Before the MSC is connected to the system, the harmonic voltage at the 400 kV bus was simply V_o. When the MSC was connected, the harmonic voltage of the 400 kV bus became magnified by the parallel combination of the system impedance (Z_{sn}) and the MSC impedance (Z_{cn}) [2.23]. The magnification factor is defined as the ratio of the bus harmonic voltage when the MSC is connected and the bus harmonic voltage prior to connection (V_o). In order to provide the required harmonic damping,

the capacitor bank can be configured as a tuned harmonic filter with a damped characteristic [2.23]. However, even with a parallel-connected damping resistor, the predicted fundamental frequency loss when subjected to the loss capitalisation figure would have resulted in an uneconomic design [2.23]. For that reason, the capacitor banks was designed as a C-type filter, as shown in Figure 2.14 [2.24].

Figure 2.15 shows an MSCDN installation in a 400 kV substation in the UK [2.25]. In service, the MSCDN serves the dual functions of reactive power compensation and harmonic filtering [2.26, 2.27]. As can be seen from Figure 2.14, the C-type filter comprises of an L_f-C_2 branch tuned to the fundamental frequency (50 Hz) for minimising the losses at steady state condition. This also means that, at the fundamental frequency, the reactive power compensation is only provided by the main capacitor, C_1. The second L_f-C_1-C_2 branch of the C-type filter is tuned on the harmonic frequency intended to be eliminated. The damping resistor (R_d) is used to damp the harmonic voltages of the network.

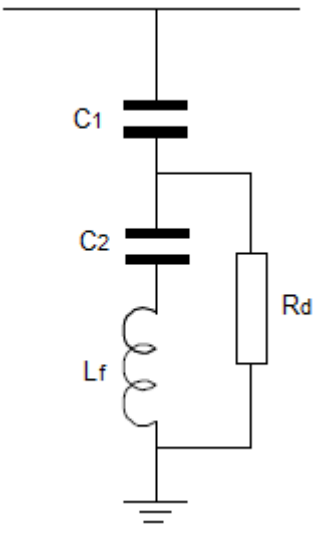

Figure 2.14: MSCDN circuit diagram [2.24]

Figure 2.15: MSCDN installation at 400 kV operational substation in the UK [2.25]

Xiao,Y. et al. [2.51] describes a mathematical relationship between all components of the filter, which can be used to the determine the filter components. The equation was useful for selecting the components that yield the most cost-efficient filter. Figure 2.16 compares the frequency responses obtained for a C-type filter, a single-tuned filter, and a capacitor bank [2.24]. The frequency response of the C-type filter in terms of impedance and phase angle is also presented in Figure 2.17. As can be seen, only the main capacitor is effectively in service at fundamental frequency, providing the reactive power required for steady state system compensation and voltage support. At frequencies above fundamental, the C-type filter acts as a heavily-damped high-pass filter. This is an interesting feature of a C-type filter in comparison with other filters, since its flat frequency response curve prevents any possible resonance with the network harmonic impedance [2.27]. This means that

very small or no voltage amplifications should be expected in the system, due to C-type filter installation [2.27].

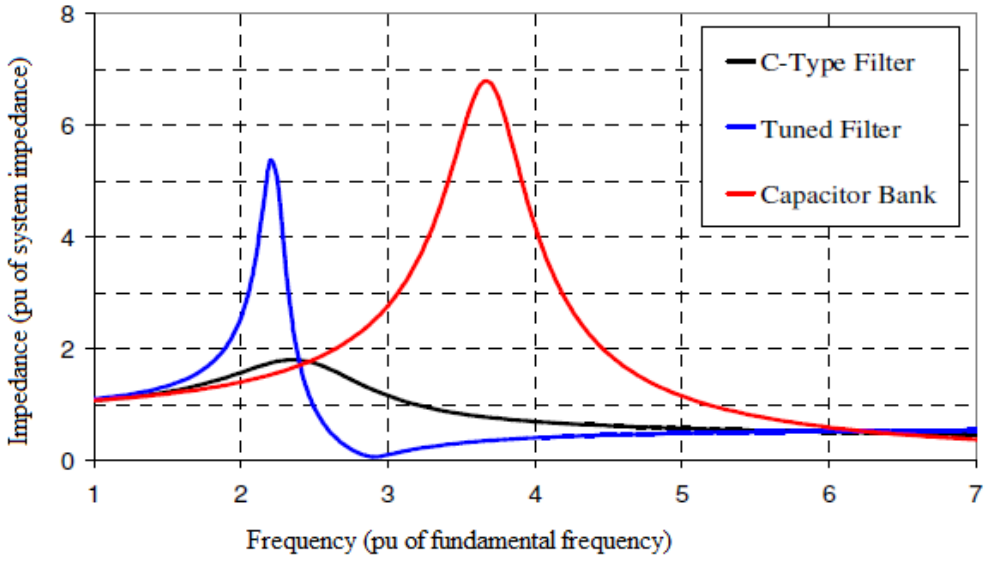

Figure 2.16: Typical frequency responses of capacitor banks, harmonic single-tuned filter, and C-type filter (MSCDN) [2.27]

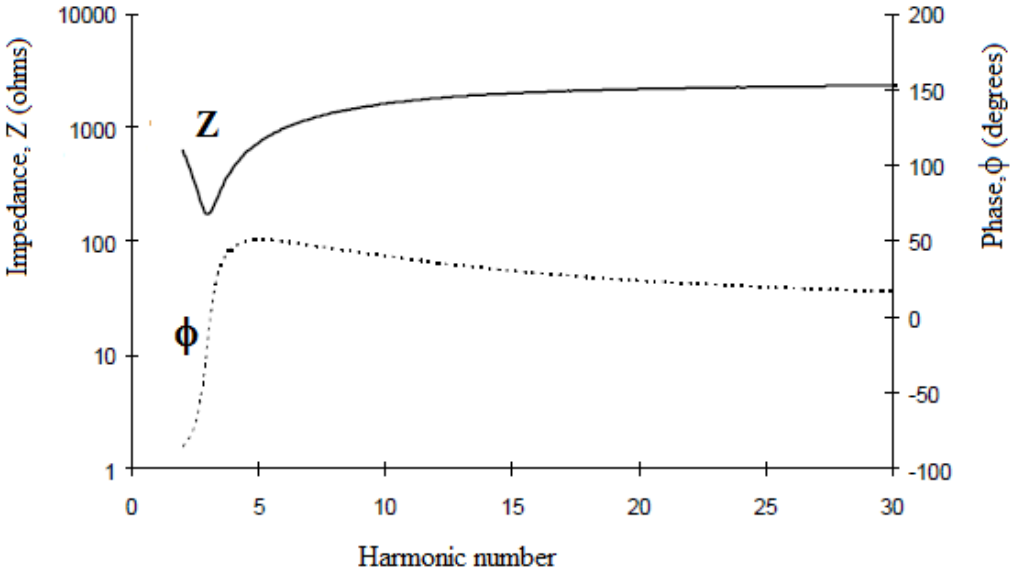

Figure 2.17: Typical frequency responses (impedance and phase) of 3rd harmonic C-type filter [2.24]

2.3.1 Switching Transients of MSCDN

In service, the MSCDN or C-type filter is also subjected to various electrical stresses that result from routine switching. The MSCDN is typically intended to operate for a daily average of 12 hours and is switched on and off each day [2.27]. Frequent switching operations and system perturbations may expose the filter components to non-standard short time transient voltages and currents with a high rate of rise and lengthy duration [2.27]. Like other harmonic filters, the MSCDN components are susceptible to high electrical and mechanical stresses, which may reduce the service life of the equipment [2.29]. As primary overvoltage protection, surge arresters are installed across the resistors and reactors, respectively to limit the transient and dynamic overvoltages on these components [2.29].

Figure 2.18 shows a circuit model indicating important electrical stresses imposed on the MSCDN components [2.31]. Accordingly, transient voltage and current stresses on the MSCDN components, as well as the surge arrester's protective level and energy absorption capability, may be determined and evaluated by the following conditions [2.26]:

- Energisation of one or more filter banks in parallel, at minimum and maximum system short-circuit levels, and for different closing times within the point-on-wave range.
- Switching surges, simulated by applying standard surge voltages, i.e. 250/2500 μs, to the filter banks.
- Lightning impulse surges, reproduced by applying standard surge voltages, i.e. 1.2/50 μs, and chopped voltages to the filter banks, equivalent to shielding failure and back-flashovers.

- Occurrence of system faults, i.e. single-phase and/or three-phase fault to earth, in close proximity to the filter banks.

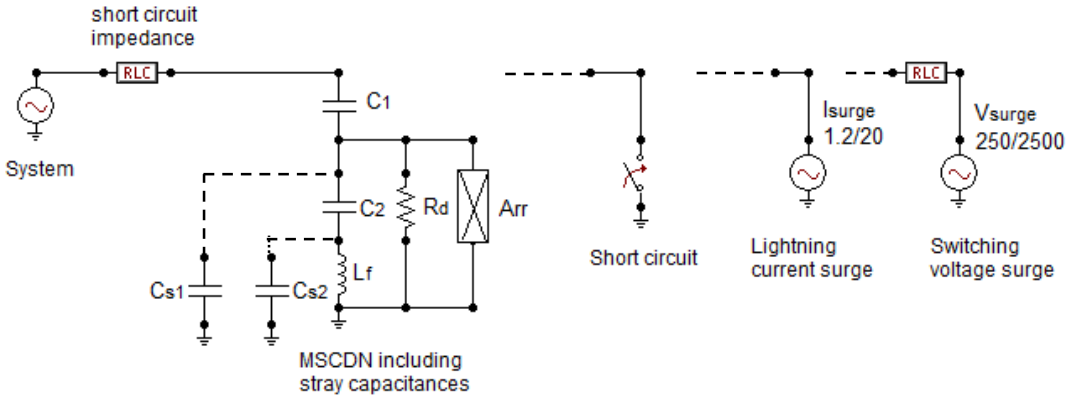

Figure 2.18: Electrical stresses on MSCDN components [2.26]

Practically, the Lightning Impulse Withstand Level (LIWL) of the MSCDN components, such as capacitors, reactors, and resistors are chosen to be at least 25% higher than the prospective maximum peak transient voltage, which also corresponds to the highest possible arrester residual voltage [2.27]. For the resistors and reactors, the Switching Impulse Withstand Level (SIWL) is selected around 80% of their Lightning Impulse Withstand Levels (LIWL) [2.27]. Transient and dynamic overvoltages and overcurrents experienced by most industrial filters are caused by some switching events such as reported in [2.29]:

- normal energising of the banks
- energising of transformers connected to the bus
- fault initiation and fault clearing on the bus
- filter breaker restriking during opening

All of these events may cause overvoltages across the individual components of the filter that exceed the bus voltage. Influential factors such as the duration of the

transient, the repetitive frequency of the event, and in some cases the duration between events can greatly contribute to the adverse effect on the filter components [2.29]. Furthermore, fast-fronted voltage and current waveforms may be generated, particularly during normal energisation of the filter banks and breaker restriking. These particular phenomena are capable of producing large rates-of-change in the voltage and current, which consequently may expose the filter components to dangerous voltage stresses [2.29].

2.3.2 Transients during Deenergisation

Deenergisation of the passive filter may cause restrikes in the circuit breaker due to arc instability [2.29], which can subsequently produce severe overvoltages at the filter components. The simulation results obtained by Bonner, et al. [2.29] confirmed that the circuit breaker restrikes during the filter deenergisation produce the highest overvoltage magnitude.

In the case of C-type filter or MSCDN, the disconnection of capacitor banks is usually made at an instant corresponding to the minimum current of the system. Following the current interruption, the capacitor bank is charged to full system voltage. The voltage stress that appears across the circuit breaker contacts is determined by the difference between the charged capacitor voltage and the supply-side voltage, which in turn influences the occurence and severity of the circuit breaker restrikes.

However, restrikes in the circuit breaker due to the filter deenergisation may not happen more than several times in the service life of the filter [2.29]. Thus, although the overvoltage magnitude due to circuit breaker restriking is the highest, the occurrence of this phenomenon is relatively less frequent; therefore, its overall

damaging effect is inconsequential. In evaluating the effect of transient overvoltages on the equipment, not only the magnitude, but also the frequency of such events occurring is important [2.29].

In this thesis, the effect of deenergising transients on the MSCDN components is not studied. It was assumed that possible high overvoltages would be avoided by the application of syncronous opening and protective devices. In addition, the use of a phase-to-ground surge arrester can reduce the generated overvoltage to safe and acceptable levels.

2.3.3 Transients during Energisation

When a capacitor is switched on to a supply, there is a powerful current surge because, for the first instant, the capacitor appears as a short circuit to the network [2.30, 2.31]. In general, capacitors can withstand current surges of up to 100 times the rated current, but the circuit breakers often limit the maximum permissible current surge to far lower values [2.25, 2.27].

Enslin, et. al [2.32] carried out the transient studies with regards to turn-on currents and voltages during the energisation of mechanically-switched capacitor with damping network (MSCDN). Figure 2.19 depicts the 150 MVar, 220 kV, C-type filter used in the studies [2.32]. The computer simulations using DigSILENT program were conducted to determine the harmonic and transient performances of the MSCDN, which were intended for replacing the existing regular MSCs. The results presented in the paper show that a maximum inrush current of 900 A was produced at the filter bank when the MSCDN is switched-in to the system [2.32]. However, the voltage transient generated at the filter bank during the energisation was barely noticeable [2.32]. In addition, the transient current appearing at the

damping resitor of the MSCDN was also computed as shown in Figure 2.20, in which case the design of a surge arrester across the damping resistor was identified to handle these transients [2.32]. Based on the results obtained, MSCDNs were regarded as a better option based on its lower inrush currents and negligible transient voltages [2.32] as compared to regular MSCs. Hence, the decision to choose the MSCDN over the regular MSCs for voltage support in the system was confirmed for Tenne-T 345 kV network [2.32].

Figure 2.19: C-type filter installation rated 150 MVar at 220 kV [2.32]

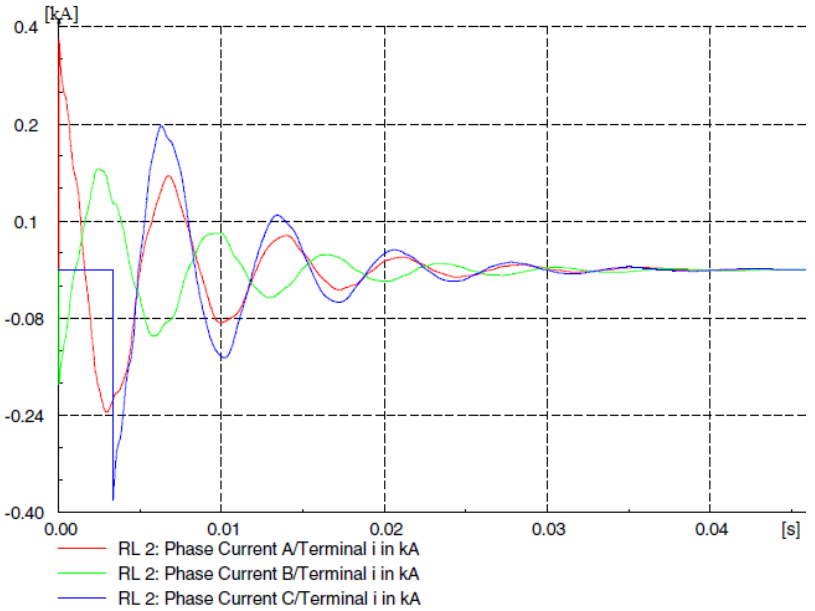

Figure 2.20: Turn-on Currents of the Damping Resistor [2.32]

According to IEEE C57.16 [2.33], and as described in Bonner, et al. [2.29], both the capacitor and the reactor of the filters are susceptible to multiple peak voltage stresses that are produced by the filter energisation. As energisation and de-energisation may occur several times a day, the damaging effects on filter components are considerable issues [2.29]. It is therefore important to conduct a detailed investigation for determining various electrical stresses impressed on the filter reactor, as a result of the MSCDN energisation.

2.4 Air-core Reactor for MSCDN

Harmonic filter reactors for medium and high voltage are typically dry-type, air-core reactors [2.33]. Figure 2.21 shows the typical construction of dry-type air-core reactors that are presently available [2.35]. The reactor winding consists of a number of parallel-connected, individually-insulated aluminium or copper conductors [2.34]. These conductors can be small wires or proprietary cables that are custom-designed and manufactured [2.34]. The windings are mechanically reinforced with epoxy-resin-impregnated fibreglass, and terminated at each end to a set of aluminium bars called a spider [2.34].

Generally, air-core reactors can be installed in either side-by-side or vertically-stacked configurations, as shown in Figures 2.22 and 2.22 [2.34]. The latter are preferred when installed in the substations or locations where space limitations exist.

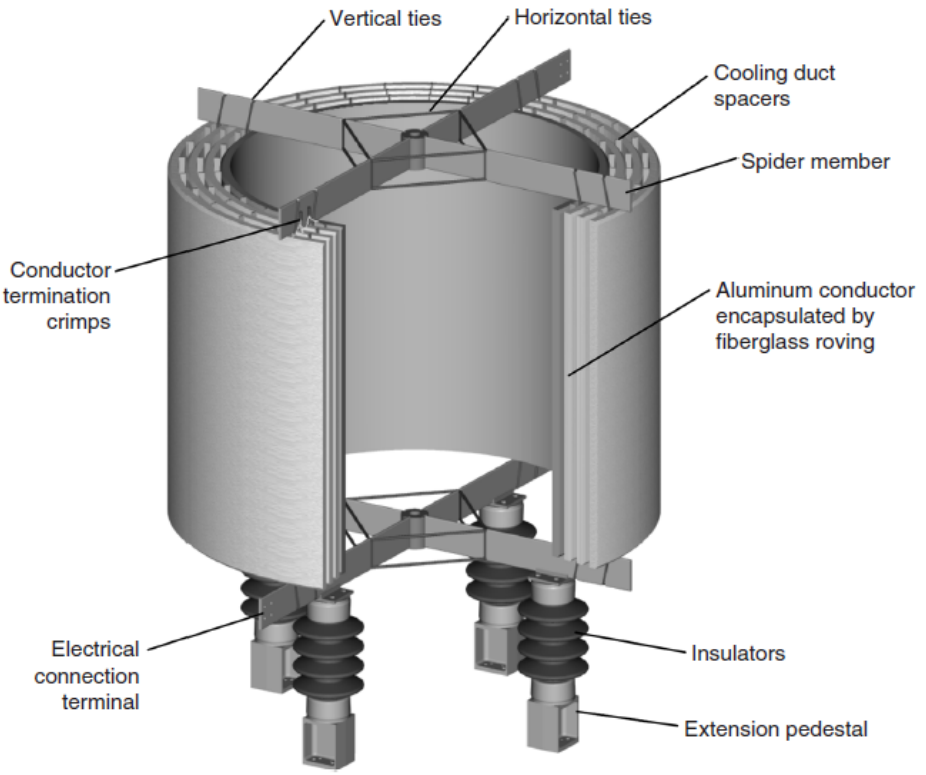

Figure 2.21: Modern fully-encapsulated design of air-core reactor [2.35]

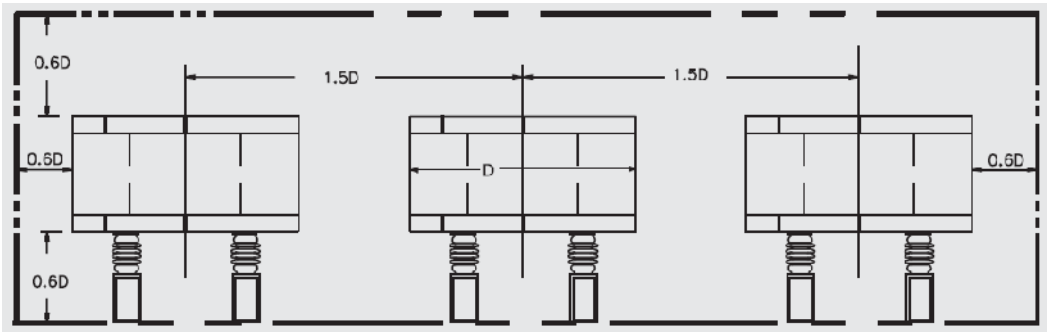

Figure 2.22: Side-by-side arrangement with recommended minimum magnetic clearances to other reactors shown [2.34]

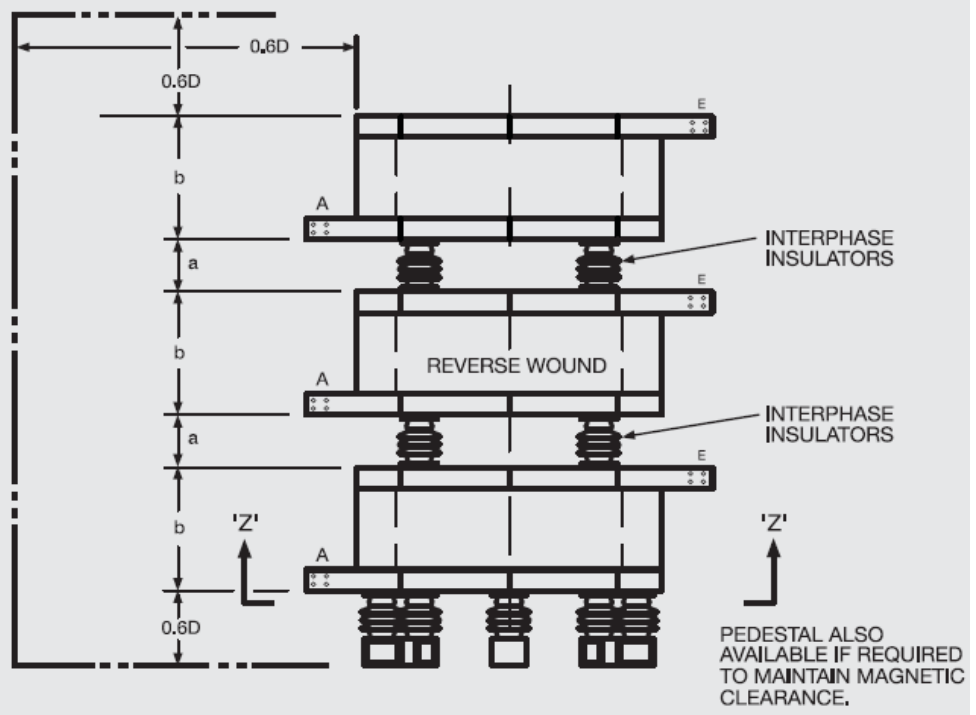

Figure 2.23: Three-phase stacked arrangement [2.34]

2.4.1 Transient Response of the Winding

The steady-state voltage across a filter reactor is low when compared to the system voltage [2.34]. Nevertheless, the reactor may be subjected to transient voltage and current stresses that result from the daily switching regime [2.33]. The current flow through a filter reactor will increase both the voltage and the cooper losses of the reactor winding. Excessive current flow may result in increased magnetic field and Joule heating.

Transient voltages can be harmful to the insulation of any power equipment if the peak value surpasses the operating voltage of the equipment. In addition, frequent switching operations may result in the imposition of repetitive stresses on the reactor, which can be harmful to the winding, as these stresses can excite its internal resonances [2.35]. Impulse voltages with a steep wave front are capable of producing

non-uniform voltage distribution, which may significantly affect the performance of winding insulation within many types of equipment, including air-core reactors [2.35]. Although the magnitude of the voltage surge is not necessarily larger than the operating voltage, the insulation is stressed much harder locally than it would be during normal operation [2.35, 2.36, 2.37].

In order to select an efficient winding and insulation structure, it is necessary for the reactor designer to know the impulse response at all parts of the winding as accurately as possible during the design stage [2.29]. The basic approach to the analysis of air-core reactor impulse response is the same as the approach applied to transformers [2.38, 2.39]. Most of the works found in the literature review [2.38, 2.39, 2.40, 2.41] analysed the voltage distribution in reactor winding based on formulae derived for transformers.

Although the response of an air-core reactor to impulses is quite similar to the response of transformers, the parameters of the reactor's equivalent circuit are somewhat different from those of the transformer [2.39]. One way in which an air-core reactor differs from a transformer is in the absence of iron-core and steel tanks. This causes the series losses in the air-core reactor to be substantially higher than the transformer [2.39]. For certain reactor designs, this also makes its ground capacitances much smaller than the series capacitances, whereas in the transformer, these capacitances are generally comparable [2.39]. Furthermore, the series and ground capacitances of air-core reactors depend critically on how the reactor is mounted with respect to the ground plane. Thus, although the equivalent circuit of the air-core reactor is essentially the same as for the transformer, its parameters are significantly different. Hence, the resultant impulse response will be different.

2.4.1.1 Lumped Parameter Model

Due to the wide spectrum of impulse voltages, a detailed model must be developed to study the internal winding stress [2.35, 2.36, 2.37, 2.42]. The analysis is carried out by first constructing a detailed lumped parameter model of the winding structure, and then carrying out a numerical solution for the transient voltage response [2.42]. For this purpose, a traditional equivalent circuit, as shown in Figure 2.24, was used [2.35]. This detailed lumped parameter model is obtained by subdividing the winding into a finite number of sections (or groups of turns) [2.35]. Each section is composed of inductances, capacitances, and resistances, which represent not only the flow of energy between the distributed electrostatic and electromagnetic characteristics of the winding but also the losses [2.35]. The computed transient voltage distribution of such a circuit is shown in Figure 2.25 [2.35].

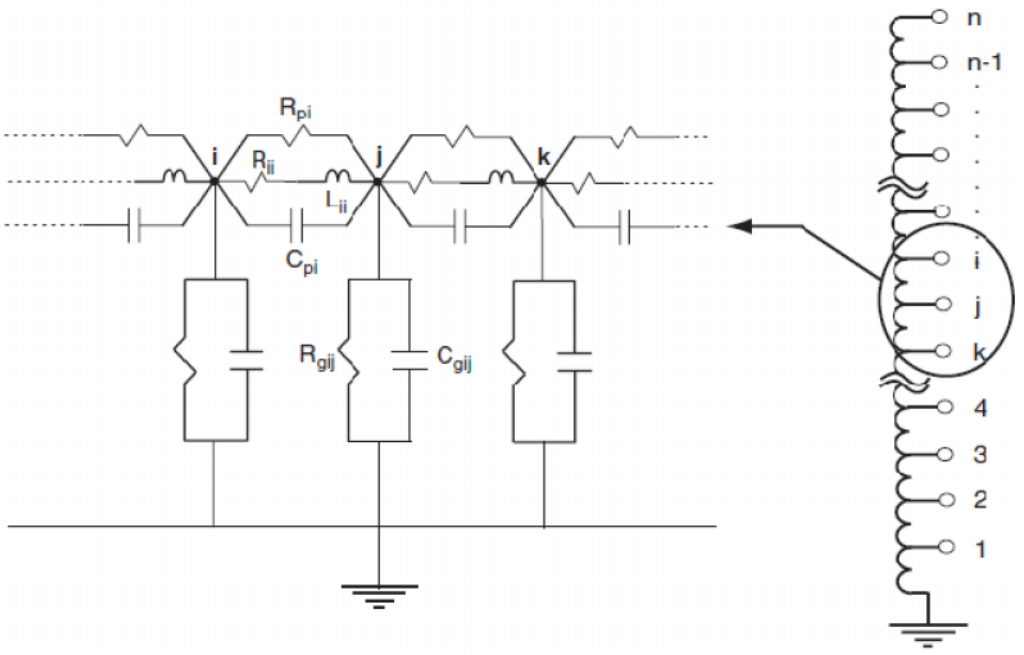

Figure 2.24: Typical lumped parameter equivalent circuit [2.35]

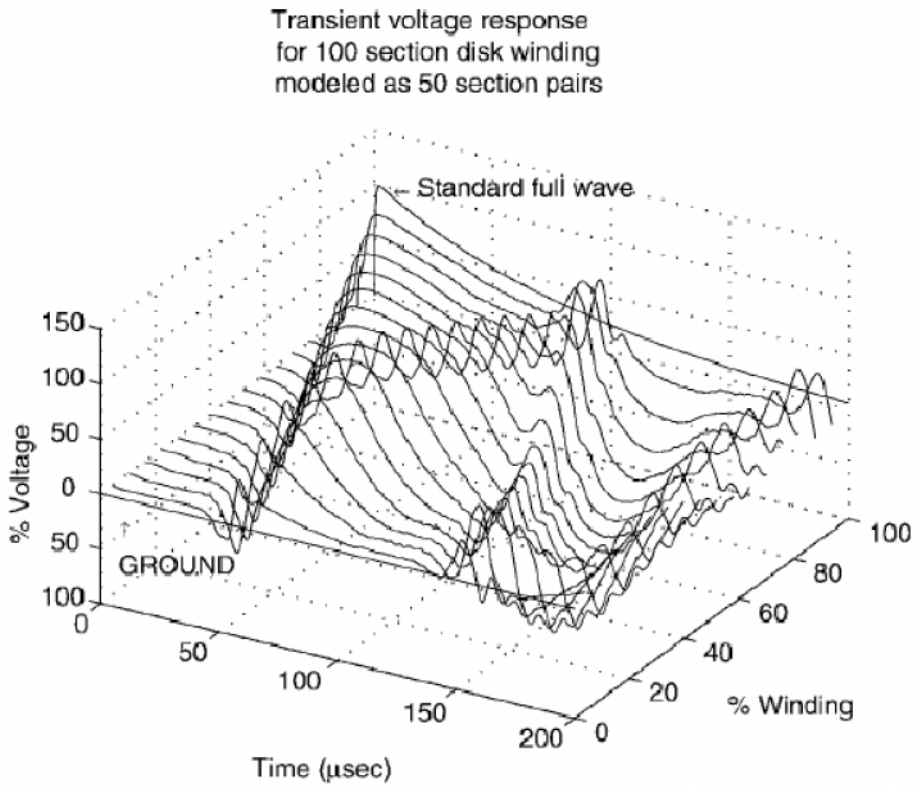

Figure 2.25: Time response of voltage across helical coil winding [2.35]

The calculation of lumped parameters within a circuit is performed using several methods. For example, the capacitance matrix of a detailed lumped circuit can be obtained using the Charge Simulation Method (CSM), as extensively documented in [2.39, 2.40,2.41]. Perhaps, the simplest method of calculating the capacitances is by using a rectangular parallel plate formula. The ground capacitances obtained using this method will be different for a horizontally- or vertically-mounted reactor, due to variation in the elevated height from the ground surface. Maruvada, et.al [2.43] introduced a set of ready-to-use equations for calculating the capacitance-to-ground of various electrode configurations, which were derived based on the parallel plate formula. This method is also adopted by Salama [2.38] for calculating the

capacitances-to-ground of a multi-package reactor winding. The series capacitance of the reactor winding was calculated using the parallel plate formula [2.38].

Under impulse conditions, the effect of the shunt losses is more dominant; therefore, the series losses can be adequately represented by the winding resistance [2.39]. The shunt losses represent the dielectric losses of the turn-to-turn insulation and the turn-to-ground insulation [2.39].

Grover's tabular method to compute the self and mutual inductances of coaxial single-layer coils is probably the fastest and most convenient formula to implement on a computer [2.45, 2.46]. This method uses a single formula in conjunction with a set of three lookup tables to simplify mutual inductance calculations [2.45]. These formulas of inductance coils are derived by solving elliptic integrals of the first, second, and third kinds. Another option for calculating the winding-turns inductance is by using fast converging and accurate elliptic integral evaluation, as introduced by Fawzi, et. al [2.46].

2.4.1.2 Transient Voltage Distribution

The voltage distribution in a winding can be established using both experimental and analytical methods. By using an analytical method, the voltage distribution was obtained by injecting a current into the excited node and determining the normalised voltage throughout the transformer winding structure [2.35]. Particularly for a single coil, it is common practice to determine the gradient of the transient voltage near the excited terminal, which is usually the most severely-affected area. This gradient is referred to as α and is expressed as [2.35]:

$$\alpha = \sqrt{\frac{C_g}{C_{tt}}} \qquad (2.13)$$

where

α winding gradient

C_g capacitance-to-ground (F)

C_{tt} effective series capacitance (F)

Ideally, for a typical coil of winding consisting of several turns, the coil voltage is distributed among the turns, so that the turn-to-turn voltage is less than the full coil voltage [2.47]. In practice, however, the pattern of impulse voltage distribution in the winding may be uniform or non-uniform. Dielectric stresses with steep wave fronts arising from switching surges are the major factors that contribute to the insulation failures of the winding [2.35]. Figure 2.26 illustrates the influence of wave front duration of a surge approaching a winding [2.47].

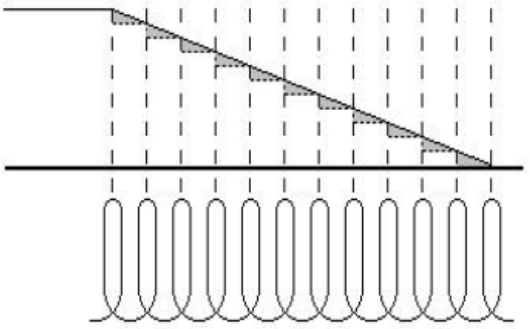

(a). Wave front duration longer than propagation time

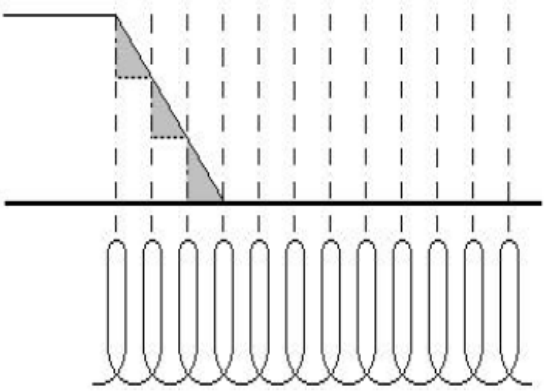

(b). Wave front duration shorter than propagation time

Figure 2.26: The influence of the surges wavefront on the voltage distribution in the winding (a) Uniform voltage distribution (b) Non-uniform voltage distribution [2.47]

In cases where the wave front duration is longer than the propagation time of a coil, the resulting voltage distribution across the winding is uniform, as shown in Figure 2.26(a) [2.47]. Both inter-turn and inter-coil insulations are not stressed by this surge. On the other hand, when the wave front duration is shorter than the propagation time of the winding, the voltage distribution becomes non-uniform, as shown in Figure 2.26(b) [2.47]. The extent of the non-uniformity is dependent on the magnitude of the difference between the wave front duration and the winding propagation time [2.47].

In this thesis, mathematical modelling and impulse voltage responses of air-core reactors is obtained based on the methodologies discussed in most previous publications [2.38, 2.39]. Salama [2.38] used analytical approach and laboratory measurements to determine the impulse and steady-state performances of a multi-package air-core reactor. In the analytical study of impulse voltage distribution, Salama [2.38] considers only the outer package of the multi-package reactor based on the assumption that this package suffers from a relatively large ground capacitive coupling. Since the internal structure of a multi-package air-core reactor is complex and difficult to model, the actual response of the winding to the applied impulse voltage is approximated as electrostatic transients [2.38]. Such an approximation leads to a relatively simple equivalent circuit of the reactor winding, comprising only of a system of capacitances, as shown in Figure 2.27. One winding element is represented capacitively by a series capacitance and two capacitances-to-ground, one at each end of the element.

Figure 2.28 shows the response of this circuit to the impulse signal that is applied [2.38]. The voltage distribution of the equivalent circuit shown in Figure 2.27 has been solved using an analytical expression, given as:

$$\frac{E}{E_1} = \frac{\sinh(N_p\alpha(1 - x/l))}{\sinh(N_p\alpha)} \qquad (2.14)$$

where,

x any distance from the tip of the reactor

l the outer package length

N_p the number of the package elements

α winding gradient of Equation (2.13)

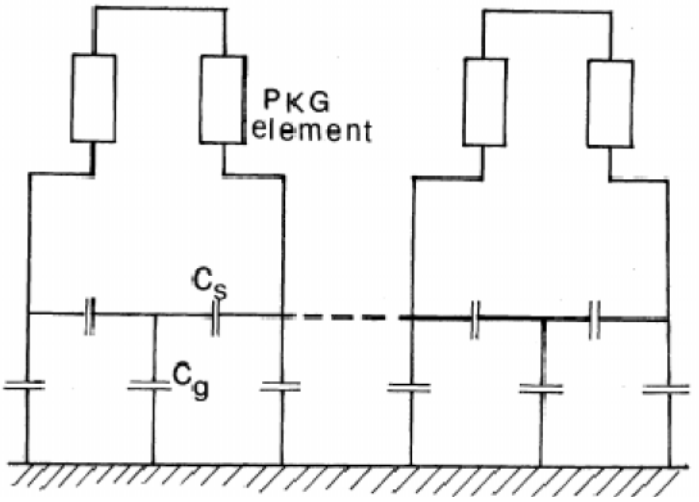

Figure 2.27: A capacitive equivalent circuit of the air-core reactor winding [2.38]

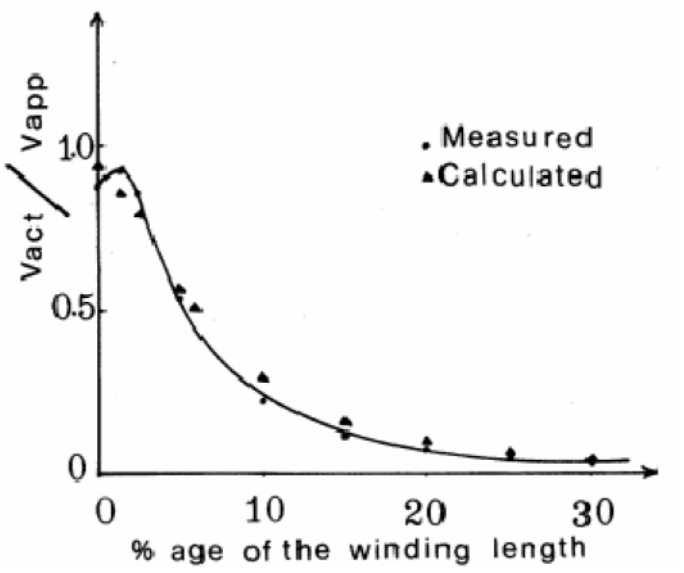

Figure 2.28: Impulse voltage distribution along the winding length for the circuit shown in Figure 2.27 [2.38]

Electrostatic treatment of the winding impulse response where, the actual winding was replaced by a system of capacitances, as presented by Salama [2.38] gives excellent results. This technique ignores the effects of capacitance-to-ground and its variation upon voltage profile along the coil length. The reactor coil is usually mounted vertically, which causes the capacitance-to-ground to vary along the coil length. Therefore, it is deemed necessary to include the effect of varying capacitance-to-ground in the calculation, as this could influence the voltage distribution and high frequency behaviour of multi-package air-core reactors.

Figure 2.29 presents the circuit model developed by Dahab, et. al. [2.39]. In the paper, a full equivalent circuit for a single-layer coil was developed, which includes the capacitances between the individual turns, the capacitances between the turns and the ground, the self and mutual inductances, and the turns and insulation resistances. In actual calculation, both the shunt resistance denoted as R_g, which accounts for the losses of the winding to ground insulation, and the mutual

capacitances denoted as $C_{i,i+}$ shown in the proposed equivalent circuit were omitted. The calculation of the capacitance coefficient was accomplished by using the charge simulation method (CSM). Figure 2.30 presents the voltage distribution along the reactor winding obtained at various time using an equivalent circuit proposed by Dahab, et. al [2.39]. The voltage response was solved analytically using the trapezoidal rule of integration with a companion network [2.39].

Dahab, et. al. [2.39] stated that the difficulty of predicting the transient behaviour of the air-core reactor were largely influenced by firstly, to the way in which the winding is divided and secondly, to the errors in the computation of the winding parameters. In their studies, the discrepancy obtained between measured and computed results is believed to be due to approximations made in the calculation process, especially during the computation of the capacitance to ground. Since the reactor used in their studies is horizontally mounted, the capacitance to ground was calculated by first evaluating the total capacitance analytically using methods described by Maruvada, et.al [2.43], and then dividing it by the total number of winding sections.

Although good agreements of the results were obtained between the calculation and the measurement, neither Salama [2.38] nor Dahab, et. al [2.39] considered the effect of varying capacitance-to-ground when constructing the detailed air-core reactor model. Thus, a more detailed distributed model accounting for the variation of the stray capacitances to ground is necessary to quantify the effect it has on the voltage distribution when the reactor is subjected to impulse voltage.

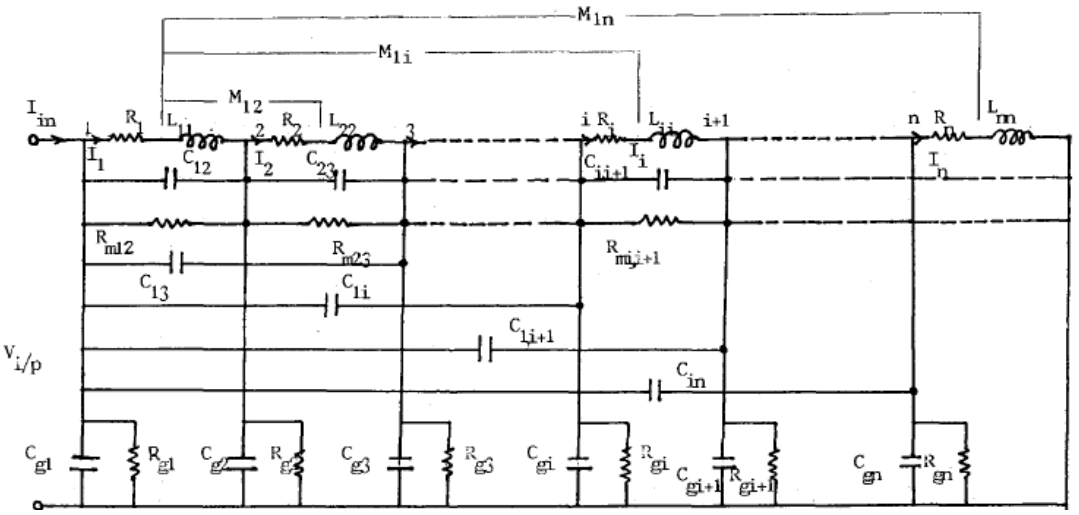

Figure 2.29: A complete model of an air-core reactor winding [2.39]

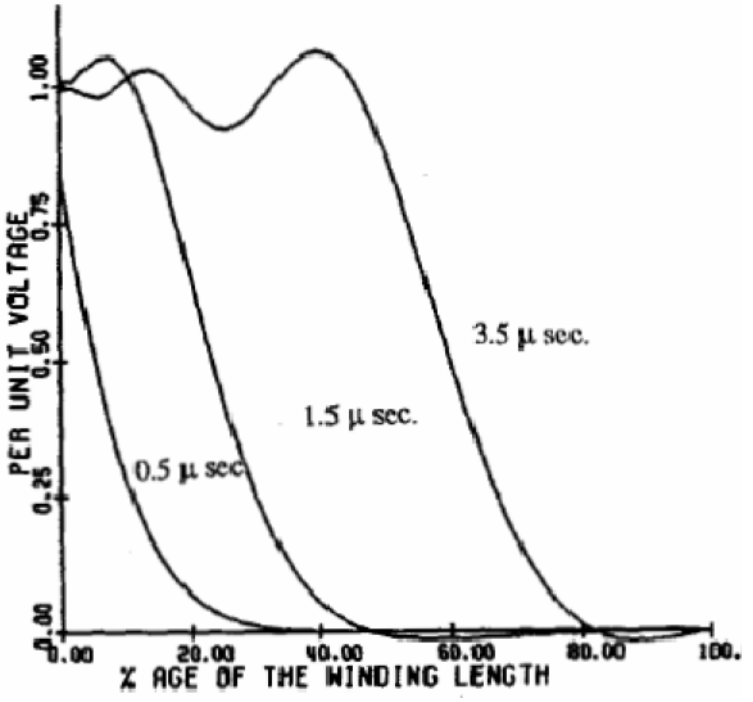

Figure 2.30: Impulse voltage distribution along the winding length for the circuit shown in Figure 2.29 [2.39]

2.4.1.3 Average Electric Field Strength

Conductors usually conform to Ohm's Law, and their resistance remains fairly constant, so the current flowing is generally proportional to the applied voltage and

is, therefore, predictable. In the case of insulators, there are properties other than resistivity that determine the passage of current and, by extension, their value as an insulator. These properties are chiefly electric strength, permittivity, and power factor. The essential properties of a dielectric are its insulation characteristic that will prevent the passage of an excessive current when electric stress is applied, and its dielectric strength to withstand electric field. The electric strength of most materials falls as temperature increases. Other parameters that significantly affect the electric strength are the waveform of the voltage, the rate of increase in voltage, the duration of voltage stress that is maintained, and the thickness of the insulating material.

In view of all the features that affect the electric strength of dielectrics, it is preferable to obtain comparative values for each variable: at a range of temperatures, for various thicknesses, and with electric stress maintained for different periods of time. Figure 2.31 and Figure 2.32 present the dielectric strength characteristics of Mylar polyester films, which is the dielectric material commonly used for air-core reactor winding insulation [2.34, 2.38, 2.39, 2.48].

As with most materials, the AC dielectric strength of Mylar increases as the film thickness decreases [2.48]. This means that the greater the film thickness, the more the failure is due to melting [2.48]. With reference to Figure 2.31, a thinner film of an insulating material can withstand a considerably higher electrical field than a thicker film of the same material. The figure also shows that a 1/4 mil thick of sheet of Mylar can withstand an electric field of 19 kV/mil. Thus, four stacked sheets of 1/4 mil Mylar can withstand 19 kV. In contrast, a single of 1 mil thick Mylar can only withstand about 7 kV. In either case, the total material thickness is 1 mil, but

the four thinner sheets are able to withstand 2.71 times the voltage stress of the single sheet of the same overall thickness.

For solid insulation, breakdown takes place due to heat generated inside the insulation. The losses loss (I^2R) generated due to increasing applied voltage would result in temperature rise of the material. This temperature rise may be higher in case of any local flaw situated deep inside a thicker insulation, because the heat cannot be dissipated to outside easily. As a consequence, local searing of the insulation may occur and could lead to local conducting path and increased current passing. However, same flaw when located in a thinner material may not result in the same process due to better heat transfer. Therefore, the breakdown voltage is high in thinner insulation and low in thicker insulation. Referring to Figure 2.32, the effect of film temperature on the dielectric strength of Mylar indicates that there is a slight decrease in dielectric strength from room temperature up to 150°C [2.48].

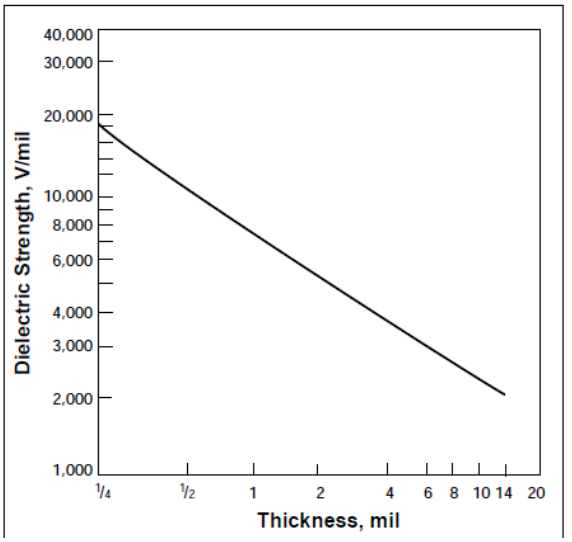

Figure 2.31: The effect of insulation thickness on dielectric strength [2.48]

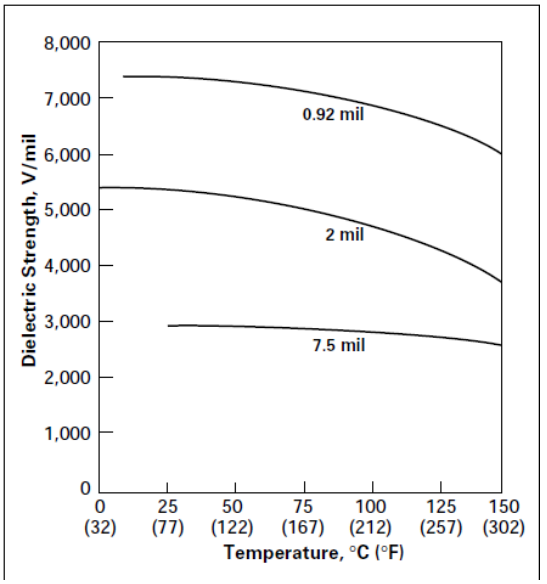

Figure 2.32: The effect of temperature on dielectric strength [2.48]

2.5 Conclusion

Chapter 1 proposed that reactors are important passive devices employed in the shunt compensation scheme for the steady-state voltage control. This chapter appraised the applications of two types of reactors, namely the shunt reactor (section 2.1) and the filter reactor (section 2.4) in the passive compensation equipment. Observations were made on the reactors that were reviewed, and the relevance of the transient stresses due to normal switching routines was summarised. The salient phenomenon associated with reactor switching is that the circuit breaker can break currents too quickly during the disconnection. The magnitude of overvoltages generated at the shunt reactor and the TRV across the circuit breaker depends merely on the phase position at which the switching takes place and the network arrangement. For shunt reactor, reignition overvoltages, which may be generated during the deenergisation present detrimental effects on the turn-to-turn winding insulation due to the steep voltage change induced. Reignitions can also produce dangerous stresses on the

connected equipment, particularly the circuit breaker grading capacitor. The resulting overvoltages across the grading capacitors can reach a magnitude extending up to three times the source voltage. The application of the MSCDN in the transmission system to provide reactive power support and harmonic filtering were reviewed in this thesis. It is of specific importance to study the transient performances of the MSCDN installation; particularly the stresses imposed on the individual components during energisation. The outcome of this analysis can be used to determine with certainty the worst case condition arising from such a routine switching, and to recommend and evaluate any required protective equipment such as surge arresters. Due to high rate-of-rise of transients that may occur during the MSCDN energisation, it is found important to study the effect of such transients on the internal insulation stresses of the filter reactor. A separate transient study of the filter reactor is necessary to determine non-uniformity of voltage distribution and possible failure mechanisms.

Chapter 3: Deenergisation Transient Voltages in Shunt Reactors

3.1 Introduction

Chapter 3 describes the deenergising transients of a 100 MVA shunt reactor as set up in an operational 275 kV substation. First, the chapter briefly describes the routine switching of a shunt reactor and the problems encountered during both energisation and deenergisation. Section 3.2 presents an analytical computation of the shunt reactor transient overvoltage during disconnection. Detailed explanation of the calculation procedures is given along with a comparison with computer simulation waveforms. The following section presents three-phase simulations of shunt reactor deenergisation by means of the ATP/EMTP program. This section also shows the results of switching during the worst conditions, which are transient overvoltages at the shunt reactor and the grading capacitor of the circuit breaker. In addition, the effect of circuit breaker switching times and the current chopping levels on overvoltage amplitude are also investigated.

3.2 Switching Transients of the Shunt Reactor

High-voltage shunt reactors are connected to the power system via circuit breakers and are switched in and out almost on a daily basis according to load fluctuations. During the energisation of a shunt reactor, problems associated with a high unsymmetrical inrush current are often encountered. For shunt reactors with a solidly-grounded neutral, unsymmetrical currents cause zero-sequence current flow, which could activate zero-sequence current relays [3.1]. In general, the mitigation method applying controlled or synchronous switching of the shunt reactor during its energisation can minimise the problem caused by inrush currents [3.2]. Furthermore,

the use of pre-insertion resistors at the circuit breaker is also capable of minimising the inrush currents during energisation, particularly for larger capacity (MVar) shunt reactors [3.2].

The real problem of shunt reactor switching is often encountered during the disconnection of a shunt reactor. Deenergisation of a shunt reactor imposes a unique and severe duty on the connected system and circuit breaker. As discussed in Chapter 2, sudden interruption of the inductive current causes energy to become trapped, resulting in oscillation between the inductor and capacitor in the load-side circuit, which consequently generates a chopping overvoltage. After the current interruption, transient recovery overvoltage (TRV) determined by the difference between the source side and the load side voltages appears across the circuit breaker. Under certain circumstances, high TRV may impose severe stresses on the circuit breaker, surpassing its voltage withstand capability, which leads to a reignition overvoltage.

The work presented in this chapter aims to investigate transient overvoltages produced by disconnecting a shunt reactor. In the analysis, the computation of transient overvoltages is established using an analytical calculation and the ATP/EMTP simulation. For analytical calculations, the Mathcad program [3.3] is employed to solve mathematical equations describing the voltage and current of the shunt reactor. The calculated results are compared and verified with the simulations performed in the ATP/EMTP program [3.4, 3.5, 3.6].

3.2.1 Analytical Calculation of Transient Overvoltages

Figure 3.1 depicts a simplified circuit used to compute the deenergising transient of the shunt reactor. In order to derive the analytical solutions, a number of simplifying

assumptions is made regarding the shunt reactor deenergisation transient. First, only one of the three phases of the shunt reactor (phase A) is represented. The shunt reactor is modelled by a lumped inductor with a series resistance. A parallel capacitance across the reactor is also included, representing the total capacitance of the bushing capacitance and the equivalent winding to ground capacitance. To simplify matters, a parallel resistance representing high frequency damping is not included in the model. Second, the connection between the circuit breaker and the shunt reactor is represented by a lumped inductor, whose value is approximated as 1 μH/m. The switch in the circuit is initially closed representing a closed circuit breaker. The switch is specified to open at a time corresponds to the minimum current.

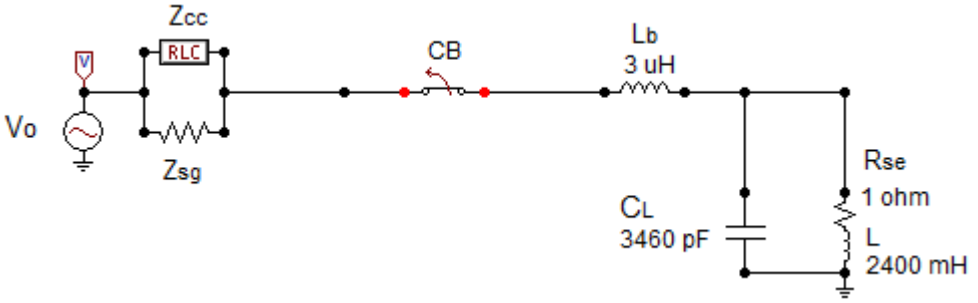

Figure 3.1: Single-phase circuit for analytical investigations

In the following analysis, the Laplace transform method is employed in an analytical transient solution of a shunt reactor disconnection [3.7].

i. Steady-state voltage and current

While the switch is in the closed position, the steady-state voltage and current as well as the initial conditions of the shunt reactor can be calculated. First, the equivalent impedance of the supply source in phasor form is obtained as Equation (3.1):

$$Z_{in} = \frac{(Z_{cc} \times Z_{sg})}{(Z_{cc} + Z_{sg})} = 0.99\angle 3.56° \ \Omega \quad (3.1)$$

Next, equivalent impedance of the load side is derived and shown in Equation (3.2):

$$Z_{out} = X_{Lb} + \frac{(X_L + R_{se}) \times X_{CL}}{(X_L + R_{se}) + X_{CL}} = 754.6 \angle 89.92° \ \Omega \quad (3.2)$$

Subsequently, the relationship between the load voltage and the source voltage can be expressed using the voltage division rule, as expressed in Equation (3.3):

$$V_c = \left(\frac{Z_{out}}{Z_{out} + Z_{in}}\right) V_o \quad (3.3)$$

where V_o is the sinusoidal source voltage given by Equation (3.4):

$$v_o(t) = 224.54\ sin(100t) \quad (3.4)$$

This source voltage is expressed in phasor form and is substituted into Equation (3.3) along with Equations (3.1) and (3.2) to yield the load-side voltage:

$$V_c = 224.5\angle 0.075° \ \text{kV} \quad (3.5)$$

The voltage obtained above is the voltage applied across the shunt reactor. Therefore, the current of the shunt reactor can be determined by dividing this voltage with the impedance of the shunt reactor. Using the voltage obtained with Equation (3.5), the shunt reactor current is found as:

$$I_L = \frac{V_c}{(X_L + R_{se})} = 297.78\angle -89.849° \ \text{A} \quad (3.6)$$

ii. Independent and dependent initial conditions

After shunt reactor disconnection, the circuit in Figure 3.1 is reduced to a parallel LC circuit that consists of the reactor inductance, L and the stray capacitance, C_L. Following the opening operation, the sum of the currents in the two branches must be zero:

$$i_c + i_L = 0 \tag{3.7}$$

The integro-differential equations are often used to characterise current and voltage for a circuit having more than one energy-storing element. Equation (3.8) presents the integro-differential equation for each of those currents in terms of the voltage across the reactor winding:

$$C_L\left(\frac{dV_L}{dt}\right) + \frac{1}{L}\int V_L\, dt = 0 \tag{3.8}$$

By taking the differentiation of both sides of Equation (3.8) with respect to time, the result is the second-order differential equation provided by the following Equation (3.9):

$$\frac{d^2}{dt^2}V_L + \frac{1}{LC_L}V_L = 0 \tag{3.9}$$

At this point, using the Laplace transform method is highly preferable to complete the circuit solution. This method has an important advantage of automatically taking the initial conditions into account [3.7]. Applying the Laplace transformation to Equation (3.9) yields the following expression:

$$s^2V_L - sV_{Lo} - V_{Lo}^{'} + \frac{V_L}{LC_L} = 0 \tag{3.10}$$

The respective V_{Lo} and V'_{Lo} are the initial value of the capacitor voltage and its first derivative. The initial conditions can be divided into independent and dependent types [3.7]. The capacitor voltage and the inductor current at the instant just after the switching are the independent initial conditions, since their values do not depend either on the circuit sources or the status of the rest of the circuit elements [3.7]. In contrast, dependent initial conditions refer to the remaining quantities in the circuit, such as the inductor voltage and the capacitor current. As expected, dependent initial conditions at the instant just after switching can change abruptly based on the initial

conditions, and their values rely on factors such as switching condition and circuit configuration [3.7].

The following analysis describes the computation of the initial conditions indicated in Equation (3.10). In the calculation, the switching time is specified at t=5 ms, the moment that coincides with the minimum system current. When the current is interrupted, the capacitance C_L is charged to voltage V_{co}. Using the phasor representation of capacitor voltage provided in Equation (3.5), the voltage when the switch chops the current is obtained as:

$$V_{co} = 224.54 \text{ kV} \tag{3.11}$$

Besides the voltage, there is also the current I_{Lo} flowing through the inductance before the switching takes place. Using the phasor representation of the inductance current in Equation (3.6), the chopped current caused by switching operation is identified as:

$$I_{Lo} = 0.833 \text{ A} \tag{3.12}$$

The following initial condition, a dependent one, is the derivative V_{co}' or dV_{co}/dt, which can be expressed as a capacitance current divided by capacitance C_L:

$$\frac{dv_{co}}{dt} = \frac{1}{C_L} i_c(0_+) \tag{3.13}$$

Based on Equations (3.7) and (3.12), the capacitance current after switching is provided as:

$$i_c(0_+) = -i_L(0_+) = -I_{Lo} \tag{3.14}$$

Substituting Equation (3.14) into Equation (3.13), the derivative capacitance voltage is finally obtained as follows:

$$\frac{dv_{co}}{dt} = -2.407 \times 10^8 \tag{3.15}$$

Next, all initial conditions provided by Equations (3.11) and (3.15) are substituted into Equation (3.10), and the voltage across the shunt reactor is expressed as follows:

$$V_L(s) = \frac{2.245 \times 10^5 s - 2.407 \times 10^8}{s^2 + 1.204 \times 10^8} \tag{3.16}$$

By taking the inverse Laplace transform, the shunt reactor voltage after disconnection is provided as:

$$v_L(t) = 224.5\, cos(1.097 \times 10^4 t) - 21.94\, sin(1.097 \times 10^4 t) \text{ kV} \tag{3.17}$$

The reactor voltage provided by Equation (3.17) is plotted as in Figure 3.2. Based on the waveform shown, the highest voltage magnitude is 225.57 kV. The frequency of oscillation, as determined mainly by the inductance (L) and the capacitance (C_L) is obtained as 1745.93 Hz.

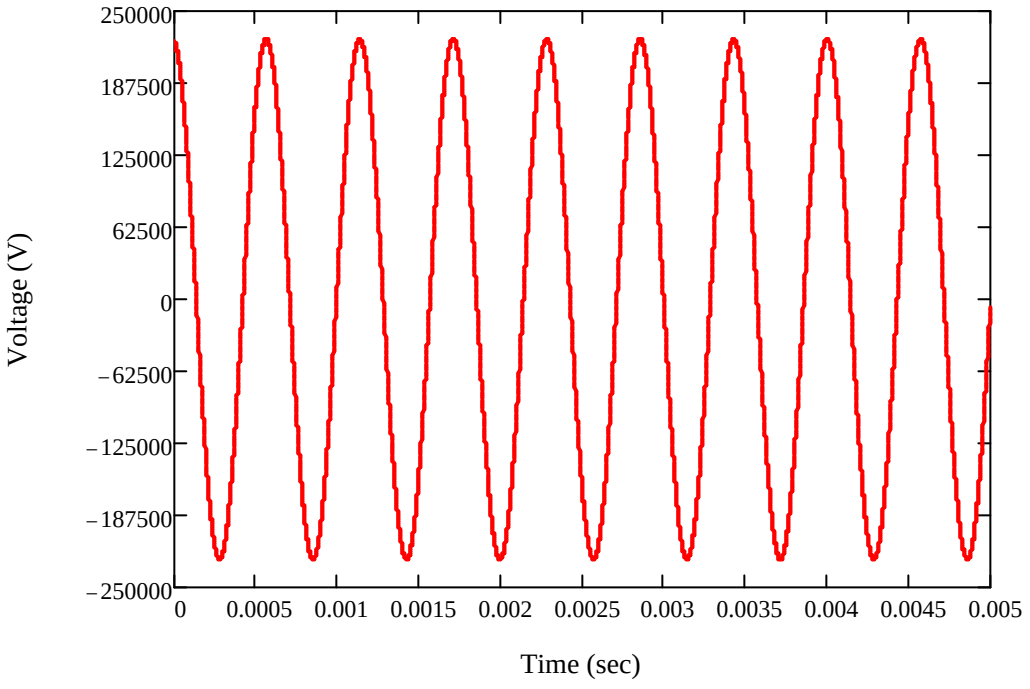

Figure 3.2: Shunt reactor voltage calculated by Laplace transforms model and equivalent circuit

3.2.2 Single-phase Shunt Reactor Simulation by ATP/EMTP

For the purpose of comparison, a single-phase transient analysis of the circuit in Figure 3.1 is also conducted by means of an ATP/EMTP simulation. The same switching condition are used for the simulation, in which the circuit breaker is set to disconnect the shunt reactor at the instant corresponding to the system current minimum. The resulting reactor voltage response after the switching operation is shown in Figure 3.3. As can be seen from the figure, no significant overvoltage is generated during the switching operation. This is expected, since the disconnection was made when the current through the shunt reactor almost reached its zero value. The highest voltage magnitude obtained for this case is 225.47 kV, and the oscillating frequency is approximately 1743.92 Hz.

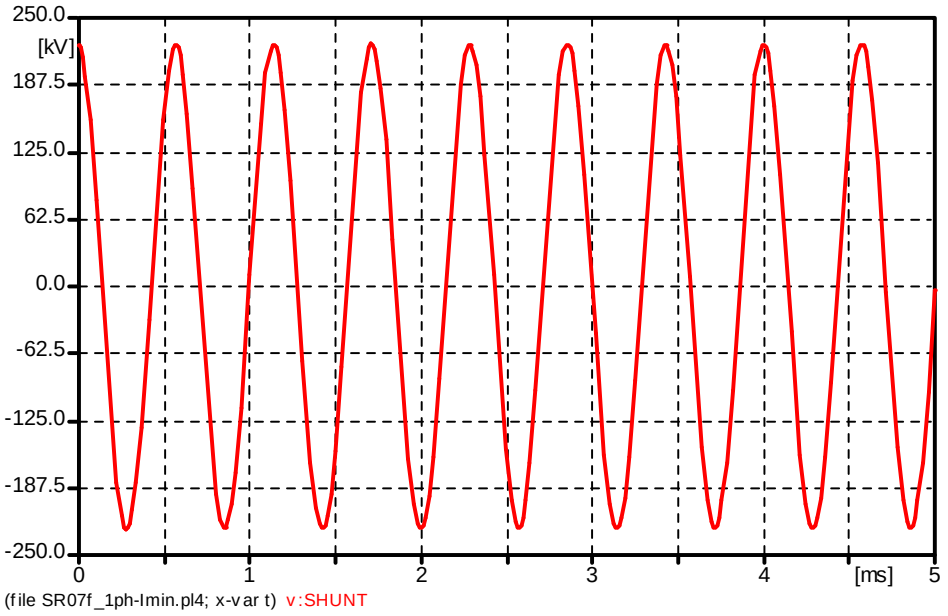

Figure 3.3: Shunt reactor voltage computed by single-phase ATP/EMTP simulation

It was found that the analytical approach gives a better understanding of the whole interrupting process, however the ATP/EMTP simulation gives more complete results with all details considering all boundary conditions automatically. Therefore,

it is much easier for the user when studying different situations of current interruption to use the ATP/EMTP.

Comparisons of the results obtained with the ATP/EMTP program and Laplace transform were presented. When using the numerical Laplace transform, the phenomena related to shunt reactor disconnection was solved in frequency domain. Conversion of the calculated voltage from the frequency domain to the time domain is required in order to recognise the amplitude and oscillating frequency. In contrast, applying ATP/EMTP, the transient voltage occuring during the shunt reactor disconnection was straightforwardly calculated. Despite the differences in solving techniques, the responses presented in Figure 3.2 and Figure 3.3 show that full agreement in transient frequencies and amplitudes of overvoltages can be confirmed between simulated and calculated, which validates the modelling approach.

3.3 ATP-EMTP Simulation of Transient Overvoltage in Three-phase Shunt Reactor Network

The previous section described switching transients associated with single-phase shunt reactor circuits. Practically, all electric power is generated, transmitted, distributed, and utilised in three-phase systems. This section presents a full three-phase simulation of reactor switching, which is conducted based on the network given in Figure 3.4 [3.8].

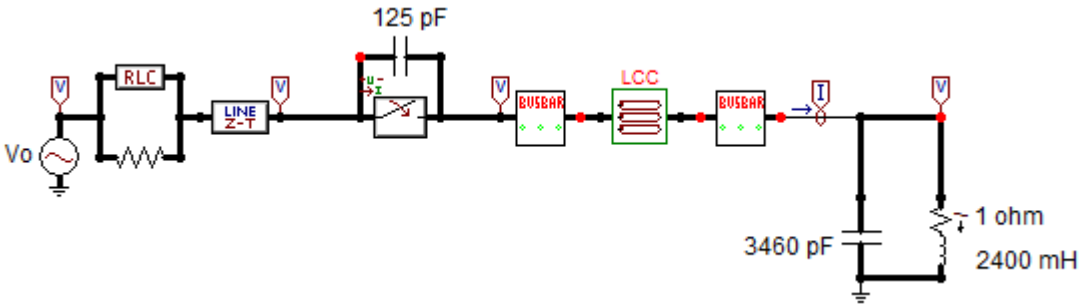

Figure 3.4: Three-phase circuit of shunt reactor switching transient [3.8]

3.3.1 Modelling Procedures

In this simulation, all components shown in Figure 3.4 were modelled according to procedures described by IEC 60071-4 [3.9] and as adopted by Coventry, et. al [3.8]. The supply network shown in Figure 3.4 is represented by a three-phase AC source of an ATP/EMTP component. The internal impedance of the source and the surge impedance seen from the reactor terminal are also taken into consideration. The circuit breaker pole responsible for disconnecting the shunt reactor from the system is modelled using a time-controlled switch of ATP component. This model is regarded as the simplest alternative to breaker modelling and can be used to represent the air-blast type breaker and the SF_6 insulated breaker [3.1].

In the initial simulation, a current chopping level of 10 A is specified to represent the circuit breaker interrupting capability of a small inductive current. Furthermore, a capacitance element is placed across the switch to represent the grading capacitors of the circuit breaker [3.8, 3.10]. The busbars and underground cables, which form the connection between the circuit breaker and the shunt reactor, have been modelled as three-phase nominal pi-circuits with parameters calculated at the free oscillation frequency of the reactor voltage (1750 Hz) [3.8]. Generally, the use of nominal pi-circuit is restricted to the case of very short lines when the line's travelling time is smaller than the integration step of the simulation. With reference to Figure 3.4, the circuit breaker is connected to the shunt reactor through a length of 57 m cable and a few meters of air-insulated busbars. Finally, a simplified shunt reactor model that consists of an inductor in parallel with a stray capacitor is employed to represent the 100 MVA shunt reactor. The objectives of the simulation are twofold:

a) To examine the variation of the overvoltages as the switching time changes. The shape and magnitude of the switching overvoltage in this case depend mainly on the point-on-wave instant at which the switching takes place, the network configuration, and the type of load that will be disconnected.

b) To observe how the surges resulting from the switching operation vary with the level of chopped current. The value of the chopped current relies mainly on the capacitance seen from the circuit breaker terminals, the number of interrupters in series per pole, and the so-called chopping number for a single interrupter, which is a characteristic value of the circuit breaker [3.2].

3.3.2 Transient Overvoltages at the Shunt Reactor and the Grading Capacitor

In the simulation, denergisation of the shunt reactor is performed at two switching times, and the highest generated transient overvoltage is observed. The switching times of 0 ms and 5 ms were specified for the first and second simulation cases, respectively. The chosen switching times represent the instants during which the current through the reactor attains minimum and maximum values.

i. Deenergisation of Shunt Reactor at Minimum Current on Phase A

The following results are obtained when the deenergisation of shunt reactor occurs at time 0 ms, corresponding to the maximum value on phase A supply voltage. The computed shunt reactor voltage during the open operation is shown in Figure 3.5 for all phases. As can be seen in the figure, no visible overvoltages were observed on phase A of the shunt reactor voltage, which was the first phase to clear because the current on this phase during interruption was at its minimum. However, overvoltages of slightly higher amplitudes can be seen in the remaining phases on the shunt reactor voltage. Their magnitude are largely dictated by each pole's operating time,

which in turn determine the magnitude of the chopped current. The highest magnitude of suppression peak overvoltage of 1.16 p.u. is identified on phase C, which was the second interrupted phase. In the last interrupted phase B, the computed suppression peak overvoltage of 1.15 p.u was obtained. The frequency of this load-side oscillation was determined to be approximately 830 Hz.

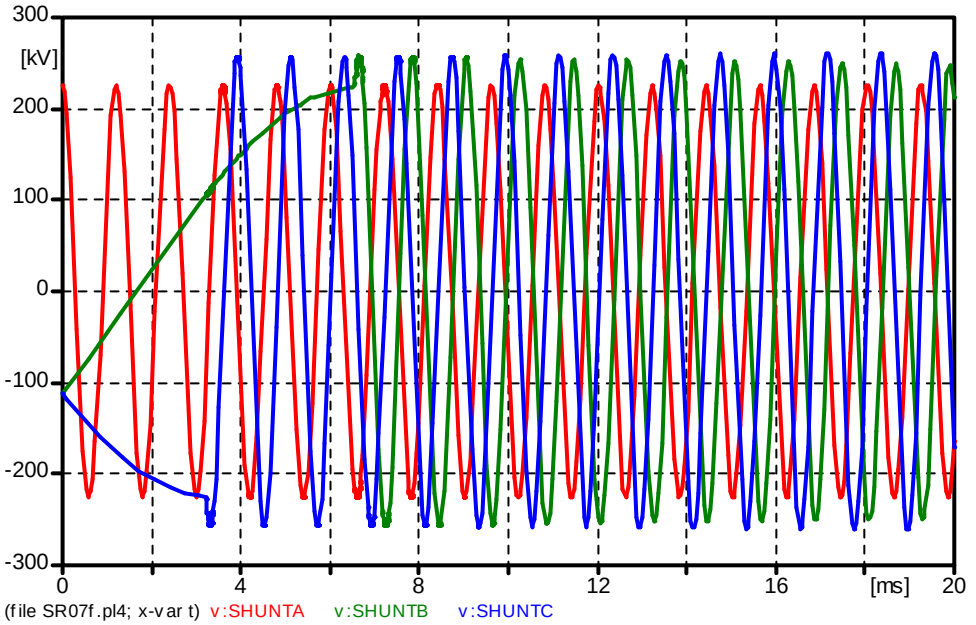

Figure 3.5: Voltage across the shunt reactor when opening at minimum current on Phase A.

Figure 3.6 depicts the computed voltage across the grading capacitor during shunt reactor disconnection. Based on the results obtained, overvoltages of high magnitude are clearly seen on all of the three phases. The resulting stress represents the difference between the system voltage on the source-side and load-side oscillations. The computed frequency of oscillation is approximately 820 Hz. The highest overvoltage was identified in the second interrupted phase, phase C, with a magnitude of 2.15 p.u. The calculated overvoltages of phase A and phase B are 2.01 p.u. and 2.13 p.u., respectively.

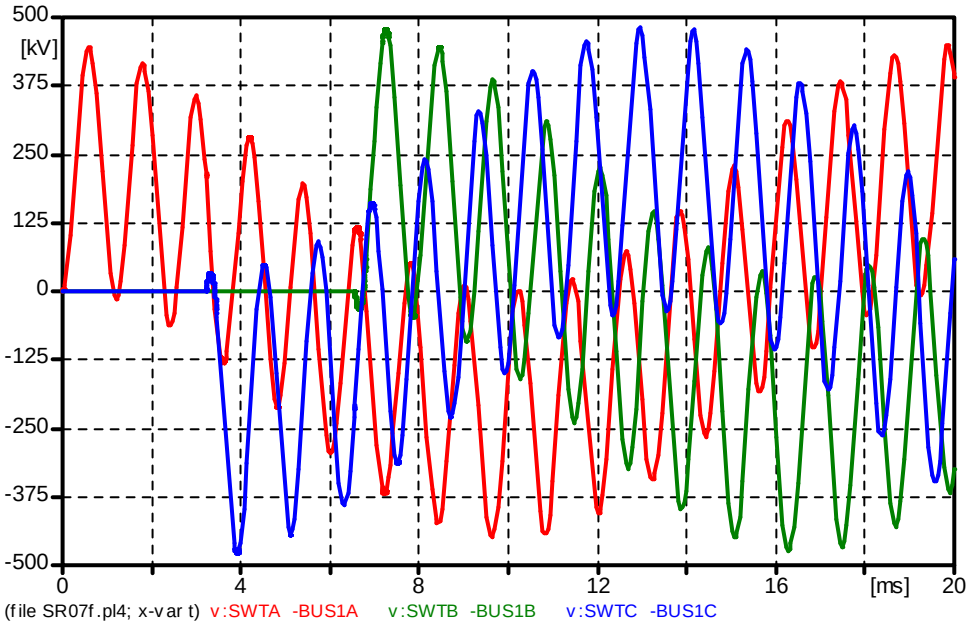

Figure 3.6: Voltage across grading capacitor when opening at minimum current on Phase A

ii. Deenergisation of Shunt Reactor at Maximum Current on Phase A

In the following, voltage responses of the shunt reactor and the grading capacitor during worst-condition deenergising transient are presented. The switching time was specified at 5 ms, which corresponds to the maximum value of the reactor current. Figure 3.7 shows the computed shunt reactor voltage for this case. As expected, the unfavorable conditions at the opening time result in high generated overvoltages on all phases of the shunt reactor. Capacitive and inductive interphase coupling can be observed. The calculated frequency of oscillation is approximately 800 Hz. The highest magnitude of suppression peak overvoltage, 1.17 p.u., was identified in phase B, which was the first phase to clear. The computed suppression peak overvoltages for phase A and phase C, which were the second and last interrupted phases, are 1.14 p.u. and 1.15 p.u., respectively.

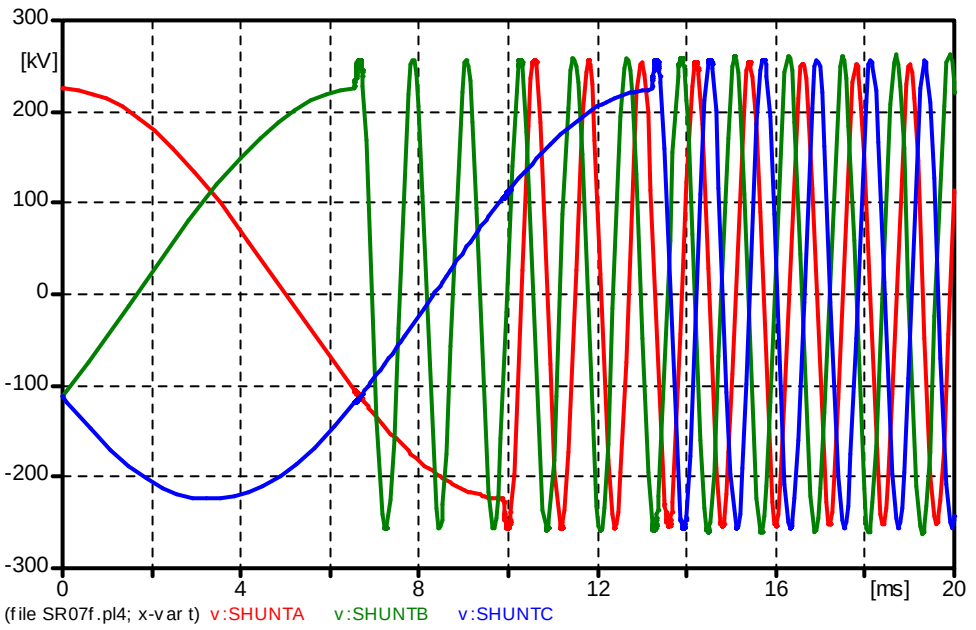

Figure 3.7: Voltage across the shunt reactor when opening at maximum current on Phase A

Comparison of the simulation results shown in Figures 3.6 and 3.7 with the result presented in Figure 3.3, demonstrates the differences between the single-phase and three-phase modelling of the shunt reactor switching. Referring to the single –phase simulation result shown in Figure 3.3, the computed shunt reactor voltage was 1.0 p.u in the minimum current switching case. The frequency of oscillation was around 1740 Hz. For the three-phase simulation, the computed shunt reactor voltage (phase A) was 1.14 p.u. in the maximum current switching case (Figure 3.7), indicating an overvoltage condition resulted from the current chopping phenomenon. Whereas, the reactor voltage (phase A) was 1.0 p.u. in the minimum current switching case (Figure 3.6).

The oscillation frequency was obtained approximately 800 Hz in the three-phase shunt reactor switching. This value is less than 1740 Hz calculated in the single-phase simulation, which is expected as the three-phase modeling considers the

connection means between the circuit breaker and the reactor, and is also subjected to frequency modulation due to phase interaction.

Figure 3.8 presents the resulting worst-case deenergising transient at the grading capacitor. It can be seen that the magnitudes of generated voltage at all phases of the grading capacitor are almost the same as in the previous simulation case. The highest overvoltage magnitude in this case, which was seen on phase C, is slightly lower in comparison with the previous case. The frequency of oscillation is determined at approximately 830 Hz. Comparing the simulated voltage of the grading capacitor shown in Figure 3.8 with the measured waveform of the same grading capacitor obtained by Coventry, et. al [3.8] shows that good agreement has been achieved between the predicted and measured voltages.

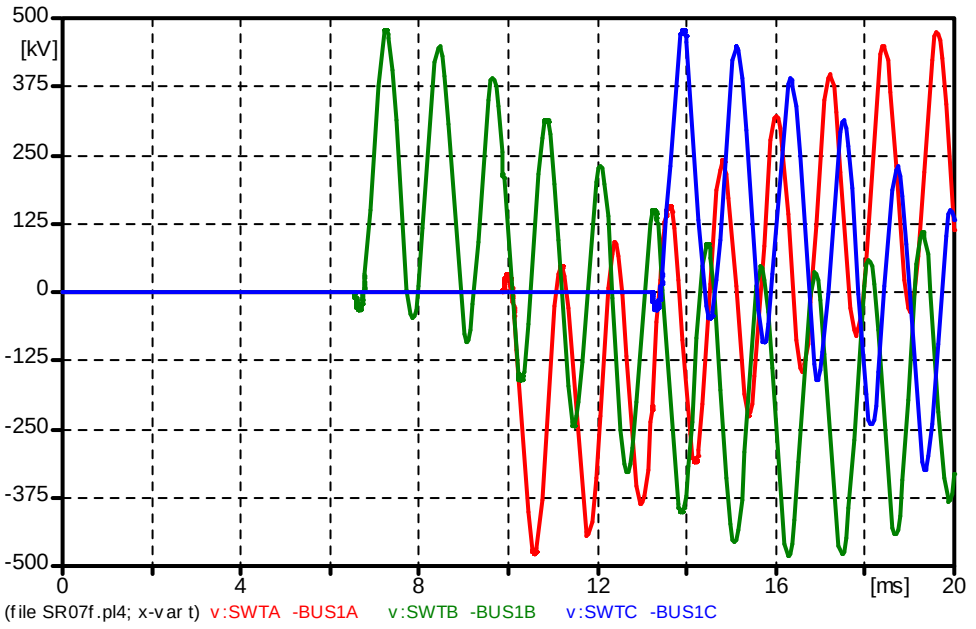

Figure 3.8: Voltage across grading capacitor when opening at maximum current on Phase A

3.3.3 Variation of Circuit Breaker Switching Time

The generated transient overvoltages at the shunt reactor and the grading capacitor mainly depend on the switching instant of the circuit breaker. Figure 3.9 and Figure 3.10 illustrate the influence of circuit breaker switching times on the overvoltage magnitude for the shunt reactor and the grading capacitor, respectively. In the computation, the opening time of the circuit breaker was varied in equal steps from an optimum time of 0 ms up to 7 ms, with the current-chopping level of the circuit breaker kept constant at I=10A. The calculated results show a significant increase in overvoltage magnitude at interruption times later than 5 ms. A similar pattern was observed for the overvoltage across the grading capacitor, shown in Figure 3.10. The saturation effect observed in both cases is due to the limitation of the maximum chopped current.

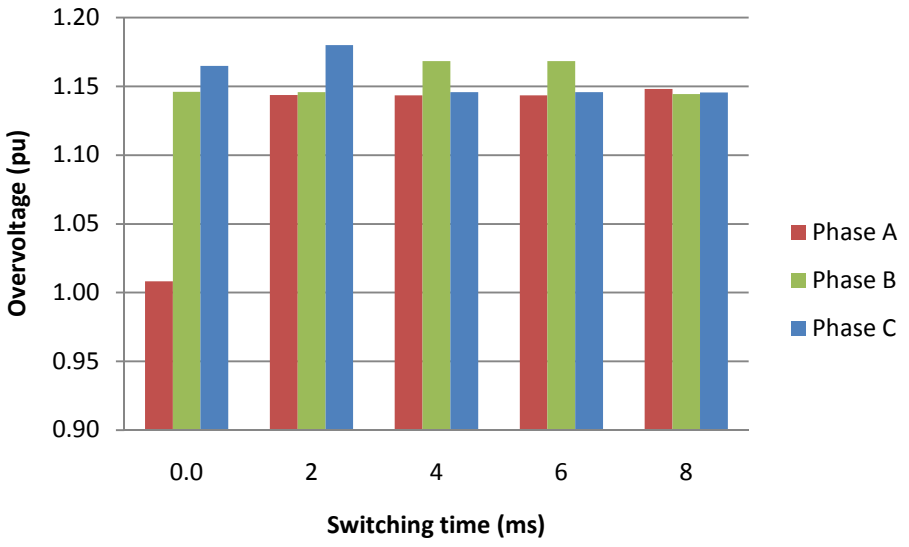

Figure 3.9: Variation of peak overvoltage across the shunt reactor with the circuit breaker switching time

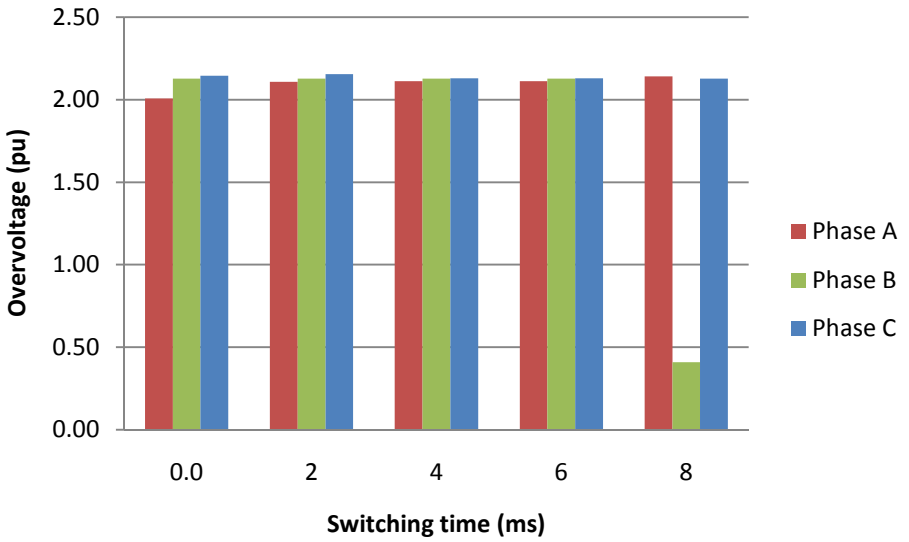

Figure 3.10: Variation of peak overvoltage across the grading capacitor with the circuit breaker switching time

3.3.4 Variation of Chopped Current Level

The current chopping level is determined by the instant of switching. In addition to that, the current chopping level is also a characteristic of the circuit breaker responsible for disconnecting the shunt reactor. This section presents the effect of a chopped current on the generated overvoltages during shunt reactor deenergisation. The disconnection of a shunt reactor is made at the time coinciding with current maximum, resulting in the worst deenergising transients of the shunt reactor. The effect of current chopping is considered by varying the marginal current of the time-controlled switch of ATP component, within a range from 0 A to the extremely high value of 100 A. The generated overvoltages at the shunt reactor and the grading capacitor are recorded. Figures 3.11 and 3.12 present the calculated overvoltages of the shunt reactor and the grading capacitor respectively, which are plotted against the chopped current levels.

As can be seen in the figure, overvoltage magnitudes in both the reactor and the grading capacitor increase with the chopped current magnitude [3.1, 3.8]. Within the realisitic current chopping capabilities of circuit breakers, the overvoltage level is always below 2.5 p.u. The increase in overvoltage magnitudes are pronounced for chopping currents in excess of 20 A. However, these values are unlikely to occur in real modern circuit breakers because of new design improvement. The overvoltages across the grading capacitors exhibit increments that are similar to those of the shunt reactor but with a much higher overvoltage.

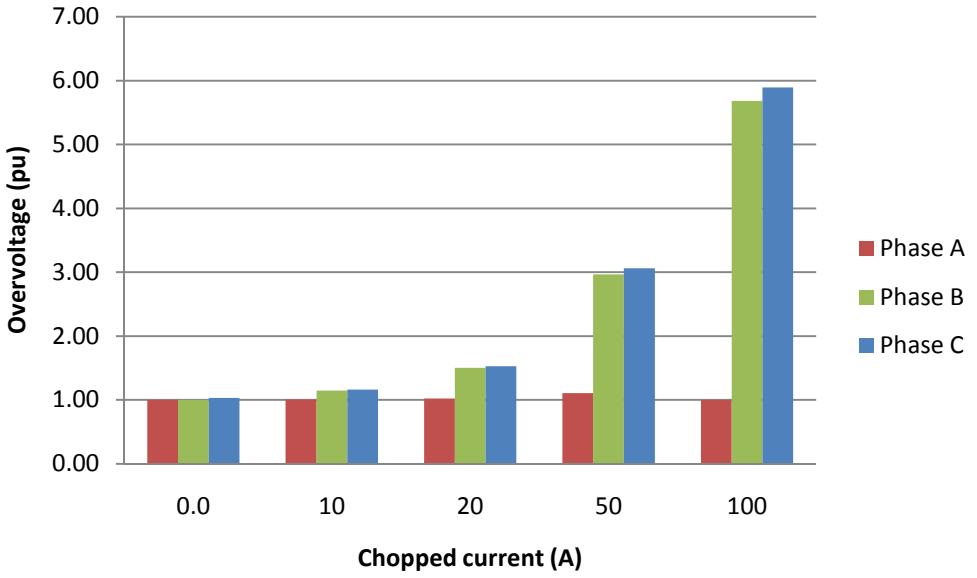

Figure 3.11: Variation of overvoltage across the shunt reactor as a function of the chopped current magnitude

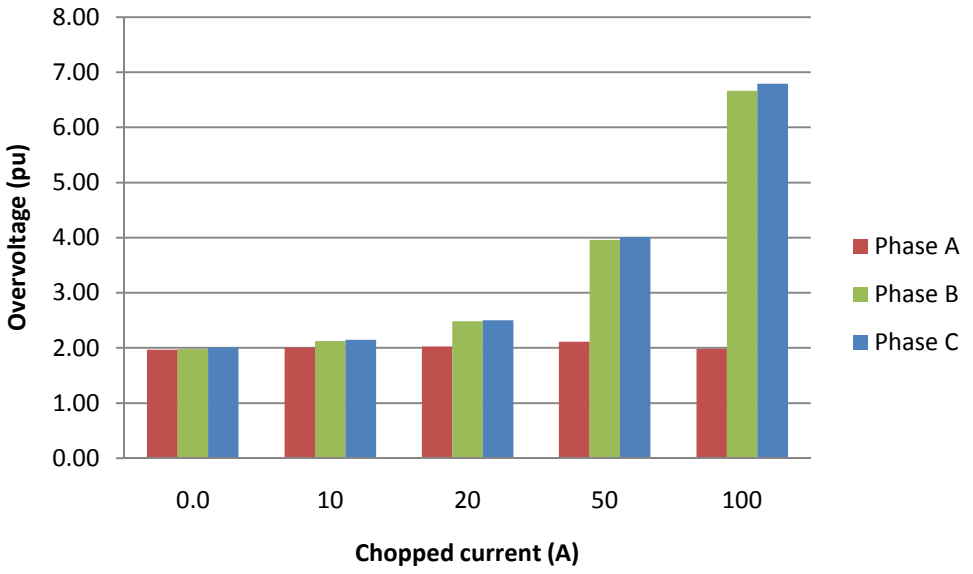

Figure 3.12: Variation of overvoltage across the grading capacitor as a function of the chopped current

3.4 Conclusion

This chapter presented both analytical and computer simulation results for overvoltages occurring during shunt reactor deenergisation. Analytical solutions using an equivalent circuit and the Laplace transform method demonstrated strong agreement with ATP simulations. Comparison between the single-phase and three-phase simulations of the shunt reactor switching shows that the oscillation frequency in the three-phase circuit is less than the value obtained in the single-phase circuit. This is expected as the modelling of the three-phase circuit considers the effect of the busbar and cable that connect the circuit breaker to the shunt reactor. For three-phase circuit, frequency modulation is dependent on the length of the connection between the circuit breaker and the reactor.

Simulations were used to analyse the three-phase shunt reactor switching overvoltages at an operational substation. The disconnection of the shunt reactor was

particularly examined at 0° and 90°on the voltage waveform of Phase A, which are considered the most important instants for a comparative data of the switching overvoltages. With a random opening of the circuit breaker, high overvoltages are generated. In addition, the influences of chopped current on the overvoltage were examined; higher chopping levels provoke excessive overvoltages across the reactor and the grading capacitors of the circuit breaker. Reduction of these amplitudes can be achieved with switching at current zero, which corresponds to the instant of minimum energy stored in the reactor.

Neglecting the damping, the phase-to-ground overvoltage magnitude is determined by the chopped current level (values range from 0 to as high as 10 A or more) and the surge impedance at the reactor terminal. In addition, the magnitude of generated overvoltages at the shunt reactor is also dependent on the MVar rating of the reactor. For the same rated voltage, a shunt reactor with large MVar rating possesses low inductance and high capacitance values. This LC combination will result in small surge impedance of the shunt reactor, which in turn reduces the overvoltage magnitude. On the other hand, a shunt reactor with small rated power has a relatively high inductance and small capacitance values. Such a reactor exhibits high surge impedance; therefore, the generated overvoltage magnitude is much higher.

Chapter 4: Energising Transient Voltages in MSCDN

4.1 Introduction

This chapter discusses the computation of transient stresses imposed on MSCDN components during routine switching of the filter. The chapter is organised as follows: after a brief introduction on the routine switching of the MSCDN in providing harmonic filtering and reactive compensation in the high-voltage power system, Section 4.3 describes the transient response of a single-phase MSCDN circuit obtained by analytical approach. The MathCAD program is used to perform analytical calculations about the voltage and current of the MSCDN components. The analytical results are compared with ATP/EMTP single-phase simulation for the purpose of modelling validation. In Section 4.4, a full model of an MSCDN three-phase network is developed. The simulations describe the responses of voltage and current at all MSCDN components in two switching cases.

4.2 Energising Transients of MSCDN

The basic topology of C-type filters is shown in Figure 4.1 [4.1]. An MSCDN is typically intended to operate for 12 hours on average each day, involving more than 700 switching operations per year [4.1]. Daily switching and system disturbances are potentially dangerous as they may generate non-standard transient voltages or current surges, which will subject the equipment to high dielectric and mechanical stresses [4.1]. Engineering studies, therefore, are vitally important and will always be performed to ensure adequate determination of the ratings of individual filter components [4.1]. The MSCDN comprises of main components such as two 3-phase capacitor banks, three single-phase air-core air-cooled reactor and six single-phase air-cooled resistors [4.2].

In this present work, the parameters of the MSCDN components are in accordance with specifications of a field-installed system supplied by the collaborating company. The MSCDN nominal rating is 225 MVar at a nominal voltage of 400 kV and fundamental frequency of 50 Hz.

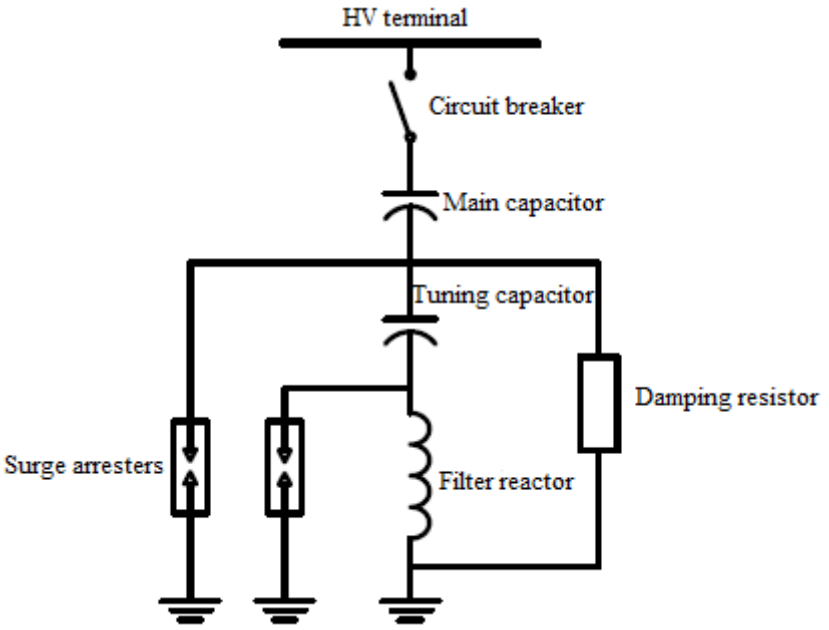

Figure 4.1: Simplified topology of MSCDN [4.1]

4.3 Analytical Solution for MSCDN Transient Analysis

Figure 4.2 shows a single-phase MSCDN circuit used for analytical studies. In this calculation, a DC voltage source is used to represent a constant application of the highest system voltage during a worst-case transient event [4.3]. The magnitude of this source voltage is specified as equal to the peak voltage of a 400 kV system. It should be noted that in this analytical calculation, surge arresters that are installed across both the damping resistor and the filter reactor are represented by lumped resistances. This resistance is obtained based on the leakage current flows through the arrester at a continuously-applied power frequency voltage. The maximum

continuous operating voltage (MCOV) can be determined from the manufacturer's datasheet based on the rated voltage of the arrester [4.4]. For the resistor arrester at 96 kV rated voltage, the MCOV is 77 kV, whereas for the reactor arrester at 144 kV rated voltage, the MCOV is 115 kV [4.4]. Based on these values, the resistance of each arrester can be calculated using the minimum resistive leakage current of 1 mA [4.4]. As a result, the resistance of the resistor arrester is 77 MΩ and the resistance of the reactor arrester is 115 MΩ, as given in Figure 4.2.

4.3.1 Main Capacitor Voltage and Current

Analytical computation of currents and voltages of the circuit elements shown in Figure 4.2 is performed using the Laplace transform method [4.3]. A mathematical routine was developed and implemented in Mathcad to perform the calculations. Two approaches are feasible namely, a) a solution based on time domain differential equations, and b) solutions based on complex frequency domain (s-domain) circuit models [4.2, 4.5]. In this work, the second approach, which allows simplification when using the Laplace transformation is used to identify currents and voltages of the MSCDN. Using this method, all elements in the circuit are expressed in terms of their impedances at a complex frequency domain, or s-domain. The DC voltage source in the s-domain is given as in Equation (4.1):

$$V_{in}(s) = \frac{326.6 \times 10^3}{s} \tag{4.1}$$

The circuit shown in Figure 4.2 was first reduced in order to allow simplified calculation of currents and voltages. This is done through the series-parallel combination circuit analysis, which is applied to the original circuit until the total impedance of the circuit is found [4.6]. Figure 4.3 shows the simplified circuit that is

obtained. The impedance Z_{eqL} represents an equivalent impedance of parallel connected reactor (L_f) and its surge arrester (ArrL), while the impedance Z_{eqR} represents an equivalent impedance of parallel connected damping resistor (R_d) and its surge arrester (ArrR).

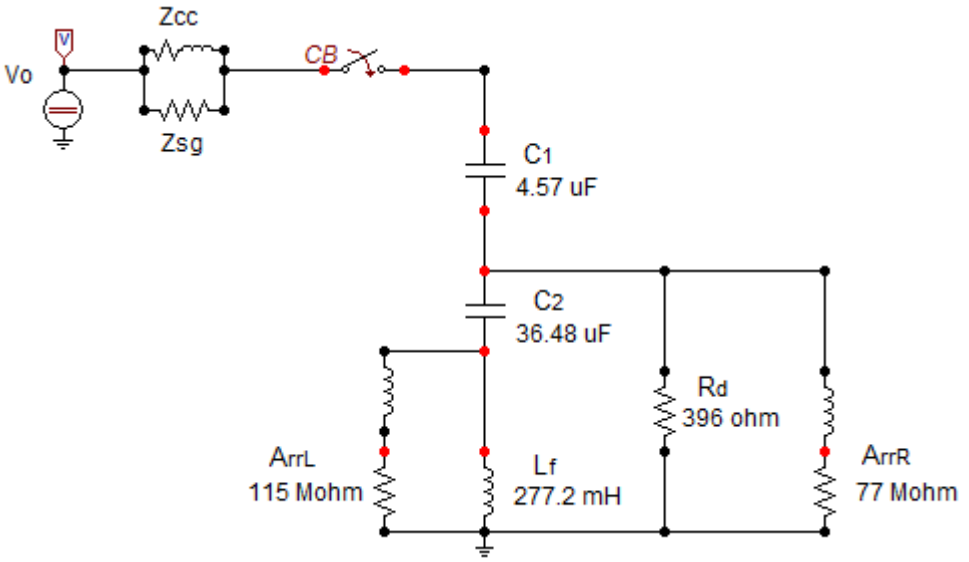

Figure 4.2: Single-phase MSCDN circuit for analytical studies

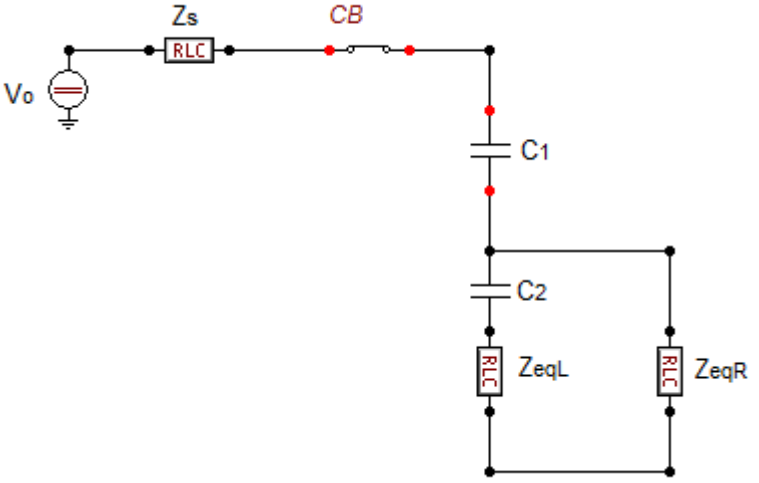

Figure 4.3: Reduced single-phase MSCDN circuit for analytical studies

This circuit is further reduced by combining the two parallel branches of C2-Z_{eqL} and Z_{eqR}. The resultant impedance forms a series connection with the main capacitor, C_1. By adding these impedances together, the total load-side impedance, which also represents the total impedance of the MSCDN, is finally obtained as:

$$Z_{out}(s) = \frac{2.188 \times 10^5}{s} + \frac{3.217 \times 10^4}{s + 72.947} - \frac{5.978.10^5}{s + 1.355 \times 10^3} - \frac{6.667310^{11}}{s + 2.567 \times 10^{13}} + 395.999 \quad (4.2)$$

By a similar method, the total source-side impedance can be calculated from a parallel combination of the short circuit and surge impedances. The equivalent impedance of the source-side is provided in Equation (4.3):

$$Z_{in}(s) = \frac{150(17s + 500)}{17s + 7.55 \times 10^4} \quad (4.3)$$

At this point, this reduced circuit only consists of a voltage source (V_{in}) in series with the equivalent source impedance (Z_{in}) and the equivalent load impedance (Z_{out}). Now, the voltage divider method can be employed to determine the load-side voltage, referred to here as the output voltage. The voltage division is expressed as in the following equation:

$$V_{out}(s) = \left(\frac{Z_{out}}{Z_{in} + Z_{out}}\right) V_{in}(s) \quad (4.4)$$

By substituting Equations (4.1-4.3) into Equation (4.4), the voltage at load terminal is obtained as:

$$V_{out}(s) = \frac{2.369 \times 10^5 s^5 + 6.08 \times 10^{18} s^4 + 3.036 \times 10^{22} s^3 + 2.031 \times 10^{25} s^2 + 2.431 \times 10^{28} s \cdots}{s(s + 3.555 \times 10^3)(s + 2.567 \times 10^{13})(s + 63.756) \cdots}$$

$$\frac{\cdots + 1.475 \times 10^{30}}{\cdots (s^2 + 402.875 + 7.761 \times 10^5)} \quad (4.5)$$

Based on this voltage and the equivalent impedance of the load side, the associated current can be obtained and is expressed as:

$$I_{out}(s) = \frac{598.234\, s^7 + 1.535 \times 10^{16} s^6 + 9.859 \times 10^{19} s^5 + 1.623 \times 10^{23} s^4 + 1.422 \times 10^{26} s^3 \cdots}{(s + 3.555 \times 10^3)(s + 2.567 \times 10^{13})(s + 63.753)(s + 63.756) \cdots}$$

$$\frac{\cdots + 9.645 \times 10^{28} s^2 + 1.139 \times 10^{31} s + 3.682 \times 10^{32}}{\cdots (s^2 + 402.875 s + 7.761 \times 10^5)(s^2 + 488.301 s + 8.567 \times 10^5)} \quad (4.6)$$

Since the voltage and current at the output terminal are known, it is now possible to find the remaining unknown currents and voltages of the MSCDN components. In fact, the first quantity traced here is the main capacitor (C1) current, which is the same as the output current obtained above.

$$I_{out}(s) = I_{c1}(s) \quad (4.7)$$

The currents or voltages in time-domain can be found using inverse Laplace transformation, which is essentially required for plotting the calculated results. Taking the inverse Laplace transform of the main capacitor current establishes the following expression in the time domain:

$$i_{c1}(t) =$$

$$0.26\, e^{-2.567 \times 10^{13} t} - 97.148\, e^{-3.555 \times 10^3 t} - 1.186 \times 10^3\, e^{-63.753 t} + 1.198 \times 10^3\, e^{-63.756 t} \cdots$$

$$\cdots + 685.702 \cos(857.626 t) e^{-201.438 t} + 1.046 \times 10^3 \sin(857.626 t)\, e^{-201.438 t} \cdots$$

$$\cdots - 2.448 \cos(892.799 t)\, e^{-244.15 t} + 1.524 \sin(892.799 t)\, e^{-244.15 t} \quad (4.8)$$

Subsequently, the associated voltage at the main capacitor was calculated. The voltage is expressed as:

$$V_{c1}(s) = \frac{1.309 \times 10^8 s^7 + 3.359 \times 10^{21} s^6 + 2.157 \times 10^{25} s^5 + 3.551 \times 10^{28} s^4 + \cdots}{(s + 3.555 \times 10^3)(s + 2.567 \times 10^{13})(s + 63.753)(s + 63.756) \cdots}$$

$$\frac{\cdots + 3.111 \times 10^{31} s^3 + 2.111 \times 10^{34} s^2 + 2.492 \times 10^{36} s + 8.056 \times 10^{37}}{\cdots (s^2 + 402.875 s + 7.761 \times 10^5)(s^2 + 488.301 s + 8.567 \times 10^5)} \quad (4.9)$$

Again, by taking the inverse Laplace transformation of Equation (4.9), the time-domain main capacitor voltage is obtained as:

$$v_{c1}(t) = 3.267 \times 10^5 + 5.969 \times 10^3 e^{-3.555 \times 10^3 t} + 4.642 \times 10^6\, e^{-63.753 t} \cdots$$

$$\cdots - 4.683 \times 10^6\, e^{-63.756 t} - 2.916 \times 10^5 \cos(857.626 t) e^{-201.438 t} \cdots$$

$$\cdots 1.066 \times 10^5 \sin(857.626 t)\, e^{-201.438 t} - 453.504 \cos(892.799 t)\, e^{-244.15 t} \cdots$$

$$\cdots - 914.073\ \sin(892.799t)\ e^{-244.15t} \qquad (4.10)$$

The responses of the main capacitor current and voltage are plotted in Figure 4.4. The results show that the maximum value of the capacitor current is approximately 1000 kA. The peak of the capacitor voltage can be computed from Equation (4.10) and is found to be about 458 kV or 140% of the steady state voltage. The frequency of oscillation, can be determined from Equations (4.9) and (4.10), and is found to be approximately 142 Hz.

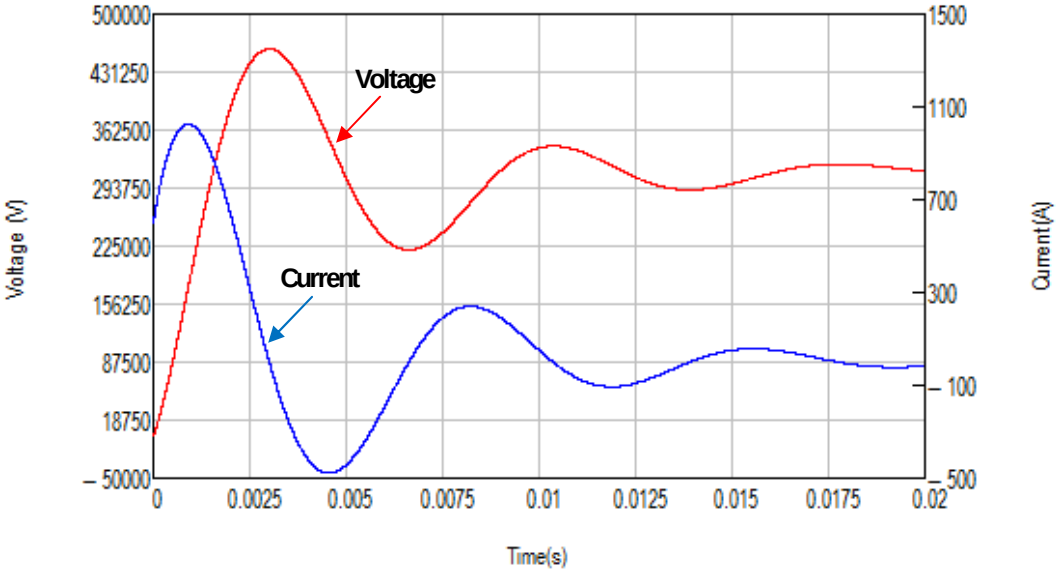

Figure 4.4: Main capacitor voltage and current using equivalent circuit and Laplace transform method

4.3.2 Damping Resistor Voltage and Current

By inspection of the simplified circuit shown in Figure 4.3, the current that flows through the main capacitor (I_{c1}) will be the same current of the equivalent impedance representing the parallel branches of the C_2-Z_{eqL} and Z_{eqR}. The resulting voltage is equal to the damping resistor voltage, and is expressed as follows:

$$V_R(s) = \frac{(2.369 \times 10^5 s^{10}) + (1.216 \times 10^{19} s^9) + (1.560 \times 10^{32} s^8) + (1.002 \times 10^{36} s^7) \cdots}{(s + 1.355 \times 10^3)(s + 3.555 \times 10^3)(s + 72.947)(s + 2.567 \times 10^{13})^2 \cdots}$$

$$\frac{\cdots + (1.665 \times 10^{39} s^6) + (1.544 \times 10^{42} s^5) + (1.143 \times 10^{45} s^4) + (2.581 \times 10^{47} s^3) \cdots}{\cdots (s + 63.753)(s + 63.756) \cdots}$$

$$\frac{(1.005 \times 10^{50} s^2) + (1.144 \times 10^{52} s) + 3.698 \times 10^{53}}{\cdots (s^2 + 402.875s + 7.761 \times 10^5)(s^2 + 488.301s + 8.567 \times 10^5)} \quad (4.11)$$

Taking the inverse Laplace transformation of the equation above yields the resistor voltage in time domain:

$$v_R(t) = 159.336\, e^{-2.567 \times 10^{13} t} - 185.496\, e^{-1.355 \times 10^{3} t} - 6.394 \times 10^4\, e^{-1.355 \times 10^{3} t} \cdots$$

$$\cdots - 1.118 \times 10^7\, e^{-63.753t} + 1.122 \times 10^7\, e^{-63.756t} - 4.515 \times 10^3\, e^{-72.947t} \cdots$$

$$\cdots + 2.608 \times 10^5 \cos(857.626t) e^{-201.438t} - 8.57 \times 10^4 \sin(857.626t)\, e^{-201.438t} \cdots$$

$$\cdots - 412.254 \cos(892.799t)\, e^{-244.15t} + 812.555 \sin(892.799t)\, \mathrm{e}^{-92.7995} \cdots$$

$$\cdots + 1.644 \times 10^{15} t e^{-2.567\, 10^{13} t} \quad (4.12)$$

Subsequently, the resistor current is obtained by dividing the calculated voltage by the resistance of 396 Ω. The current expression in s-domain is found as:

$$I_R(s) = \frac{2.369 \times 10^5 s^{10} + 1.216 \times 10^{19} s^9 + 1.560 \times 10^{32} s^8 + 1.002 \times 10^{36} s^7 \cdots}{396(s + 1.355 \times 10^3)(s + 3.555 \times 10^3)(s + 72.947)(s + 2.567 \times 10^{13})^2 \cdots}$$

$$\frac{\cdots + 1.665 \times 10^{39} s^6 + 1.544 \times 10^{45} s^5 + 1.143 \times 10^{45} s^4 + 2.581 \times 10^{47} s^3 \cdots}{\cdots (s + 63.753)(s + 63.756)}$$

$$\frac{\cdots 1.005 \times 10^{50} s^2 + 1.144 \times 10^{52} s + 3.698 \times 10^{53}}{\cdots (s^2 + 402.875s + 7.761 \times 10^5)(s^2 + 488.301s + 8.567 \times 10^5)} \quad (4.13)$$

Again, taking the inverse Laplace transformation gives the resistor current in time-domain as:

$$i_R(t) = 0.402 e^{-2.567 \times 10^{13} t} - 0.468\, e^{-1.355 \times 10^{3} t} - 161.461\, e^{-1.355 \times 10^{3} t} \cdots$$

$$\cdots - 2.822 \times 10^4\, e^{-63.753t} + 2.833 \times 10^4\, e^{-63.756t} - 11.402\, e^{-72.947t} \cdots$$

$$\cdots + 658.616 \cos(857.626t) e^{-201.438t} - 216.408 \sin(857.626t)\, e^{-201.438t} \cdots$$

$$\cdots - 1.041 \cos(892.799t)\, e^{-244.15t} + 2.052 \sin(892.799t)\, \mathrm{e}^{-244.15\mathrm{t}} \cdots$$

$$\cdots + 4.152 \times 10^{12} \mathrm{te}^{-2.256 \times 10^{13} \mathrm{t}} \quad (4.14)$$

Figure 4.5 presents the time domain voltage and current responses obtained at the damping resistor. The current that flows through the damping resistor is shared with

the parallel-connected filter reactor. From Equation (4.14), the highest magnitude of the resistor current reached approximately 600 A. The resistor voltage has magnitude of 238 kV. Based on Equations (4.13) and (4.14), the oscillation frequency is calculated to be around 142 Hz.

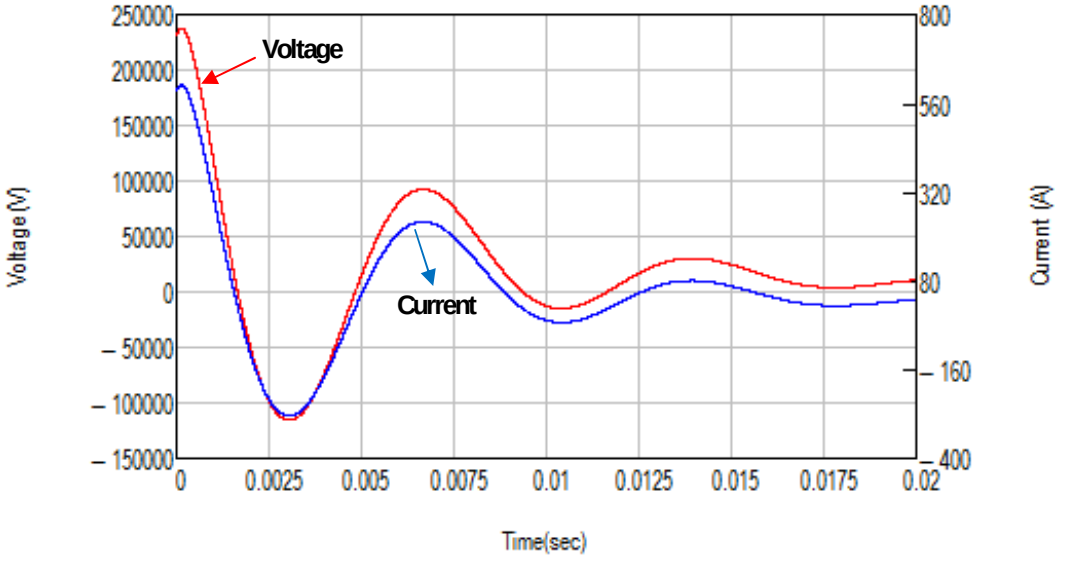

Figure 4.5: Damping resistor voltage and current using equivalent circuit and Laplace transform method

It is also possible to determine the current flow of the resistor arrester based on the information obtained previously. With reference to the circuit in Figure 4.2, the voltage across the resistor arrester (ArrR) is the same as the resistor voltage (R_d), since the arrester is placed across the resistor. Therefore, the current flow of the arrester can be found by dividing the resistor voltage by the resistance of the arrester. The arrester current is expressed as:

$$I_{arrR}(s) = \frac{2.369 \times 10^5 s^{10} + 1.216 \times 10^{19} s^9 + 1.566 \times 10^{32} s^8 + 1.002 \times 10^{36} s^7 \cdots}{(s + 72.947)(s + 1.355 \times 10^3)(s + 2.567 \times 10^{13})^2 (s + 63.753)(s + 63.756) \cdots}$$

$$\frac{\cdots + 1.665 \times 10^{39} s^6 + 1.544 \times 10^{45} s^4 + 1.143 \times 10^{45} s^4 + 2.581 \times 10^{47} s^3 \cdots}{\cdots (s + 3.555 \times 10^3)\left({}^{3s}/_{(1 \times 10^6)} + 7.7 \times 10^7\right) \cdots}$$

$$\frac{\cdots 1.005 \times 10^{50} s^2 + 1.144 \times 10^{52} s + 3.698 \times 10^{53}}{\cdots (s^2 + 402.875 s + 7.761 \times 10^5)(s^2 + 488.301 s + 8.567 \times 10^5)} \quad (4.15)$$

Applying the inverse Laplace transformation to Equation (4.15) above yields the time-domain form of the resistor arrester current, and is found as follows:

$$i_{arrR}(t) = 49.338e^{-2.567\times10^{13}t} - 49.341\, e^{-2.567\times10^{13}t} - 0.145\, e^{-63.753t} + 0.146\, e^{-63.756t} \ldots$$

$$\cdots +3.3876 \times 10^{-3}\cos(857.626t)e^{-201.438t} - 1.113 \times 10^{-3}\sin(857.626t)\, e^{-201.438t} \ldots$$

$$\cdots 1.644 \times 10^{11}\mathrm{te}^{-2.256\times10^{13}\mathrm{t}} \qquad (4.16)$$

The response of the resistor arrester current is plotted as shown in Figure 4.6. As can be seen from the figure, only a small current of approximately 4 mA flowing through the arrester of the damping resistor for this case.

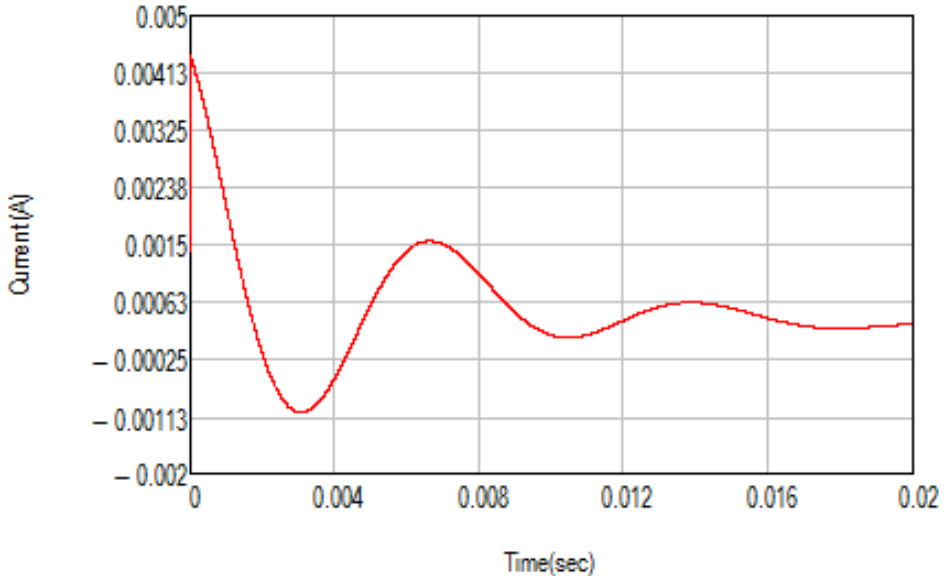

Figure 4.6: Current of the resistor arrester using equivalent circuit and Laplace transform method

4.3.3 Filter Reactor Voltage and Current

The next MSCDN component considered in analytical computations is the filter reactor. With reference to the simplified circuit shown in Figure 4.3, the impedance of the combined reactor and its arrester (Z_{eqL}), is in series with the tuning capacitor (C_2); hence, the same current will flow through this branch. This current can be calculated using the resistor voltage obtained previously, since the series C_2-Z_{eqL} and

the equivalent impedance Z_{eqR} are in parallel. The current was calculated using the resistor voltage and the impedance of the C_2-Z_{eqL} branch. Accordingly, the voltage across the filter reactor can be obtained, and is given as:

$$V_L(s) = \frac{3.186\times10^7 s(2.369\times10^5 s^{10} + 1.216\times10^{19}s^9 + 1.56\times10^{32}s^8 + 1.002\times10^{36}s^7)\cdots}{(s+1.355\times10^3)(s+2.567\times10^{13})^2(s+63.753)(s+63.756)\cdots}$$

$$\frac{\cdots + 1.665\times10^{39}s^6 + 1.544\times10^{42}s^5 + 1.143\times10^{45}s^4 + 2.581\times10^{47}s^3\cdots}{\cdots(0.277s+1.15\times10^8)(s+3.555\times10^3)\left(\frac{2.741\times10^4}{s}\right)\left(\frac{3.186\times10^7 s}{0.277s+1.15\times10^8}\right)\cdots}$$

$$\frac{\cdots + 1.005\times10^{50}s^2 + 1.144\times10^{52}s + 3.698\times10^{53}}{\cdots(s+72.947)(s^2+402.875s+7.761\times10^5)(s^2+488.301s+8.567\times10^5)} \quad (4.17)$$

Taking the inverse Laplace transformation, the reactor voltage in time domain is obtained:

$$V_L(t) = 159.336e^{-2.567\times10^{13}t} - 176.011\,e^{-1.355\times10^3 t} - 6.3445\times10^4\,e^{-3.555\times10^3 t}\cdots$$

$$\cdots - 4.41\times10^5\,e^{-63.753t} + 4.428\times10^5\,e^{-63.756t} - 63.756\,e^{-72.947t}\cdots$$

$$\cdots + 100.378\cos(314.543t) - 14.543\sin(314.543t)\cdots$$

$$\cdots + 2.994\times10^5\cos(857.626t)e^{-201.438t} - 201.43\times10^4\sin(857.626t)\,e^{-201.438t}\cdots$$

$$\cdots 514.449\cos(892.799t)\,e^{-244.15t} + 868.682\sin(892.799t)\,\mathrm{e}^{-92.7992}\cdots$$

$$\cdots + 1.644\times10^{15}\mathrm{te}^{-2.256\times10^{13}\mathrm{t}} \quad (4.18)$$

Following the calculated voltage of the reactor, the associated current can be found based on its impedance. The following equation provides the reactor current:

$$I_L(s) = \frac{1.149\times10^8 s(2.369\times10^5 s^{10} + 1.216\times10^{19}s^9 + 1.56\times10^{32}s^8 + 1.002\times10^{36}s^7)\cdots}{(s+1.355\times10^3)(s+2.567\times10^{13})^2(s+63.753)(s+63.756)\cdots}$$

$$\frac{\cdots + 1.665\times10^{39}s^6 + 1.544\times10^{42}s^5 + 1.143\times10^{45}s^4 + 2.581\times10^{47}s^3\cdots}{\cdots(0.277s+1.15\times10^8)(s+3.555\times10^3)\left(\frac{2.741\times10^4}{s}\right)\left(\frac{3.186\times10^7 s}{0.277s+1.15\times10^8}\right)\cdots}$$

$$\frac{\cdots + 1.005\times10^{50}s^2 + 1.144\times10^{52}s + 3.698\times10^{53}}{\cdots(s+72.947)(s^2+402.875s+7.761\times10^5)(s^2+488.301s+8.567\times10^5)} \quad (4.19)$$

Again, by taking the inverse Laplace transformation, the reactor current in time domain can be expressed as in Equation (4.20).

$$i_L(t) =$$

$$0.468\, e^{-1.355\times10^3 t} + 64.359\, e^{-3.555\times10^3 t} + 2.495\times10^4\, e^{-63.753t} - 2.505\ \times10^4\, e^{-63.756t} \cdots$$

$$\cdots + 11.393\, e^{-72.947t} - 0.847\cos(314.543t) - 1.151\ \sin(314.543t) \cdots$$

$$\cdots + 28.853\cos(857.626t) e^{-201.438t} + 1.266\times10^3\ \sin(857.626t)\, e^{-201.438t} \cdots$$

$$\cdots - 2.736\cos\ (892.799t)\, e^{-244.15t} - 2.826\sin(892.799t)\, \mathrm{e}^{-244.15\mathrm{t}} \cdots$$

$$\cdots - 230.99\ \mathrm{te}^{-2.256\times10^{13}\mathrm{t}} \qquad (4.20)$$

The plots of the reactor voltage and current are shown in Figure 4.7. The reactor voltage has a magnitude of approximately 240 kV; oscillating at a frequency of 142 Hz. The amplitude of the current flow through the reactor is approximately 800 A.

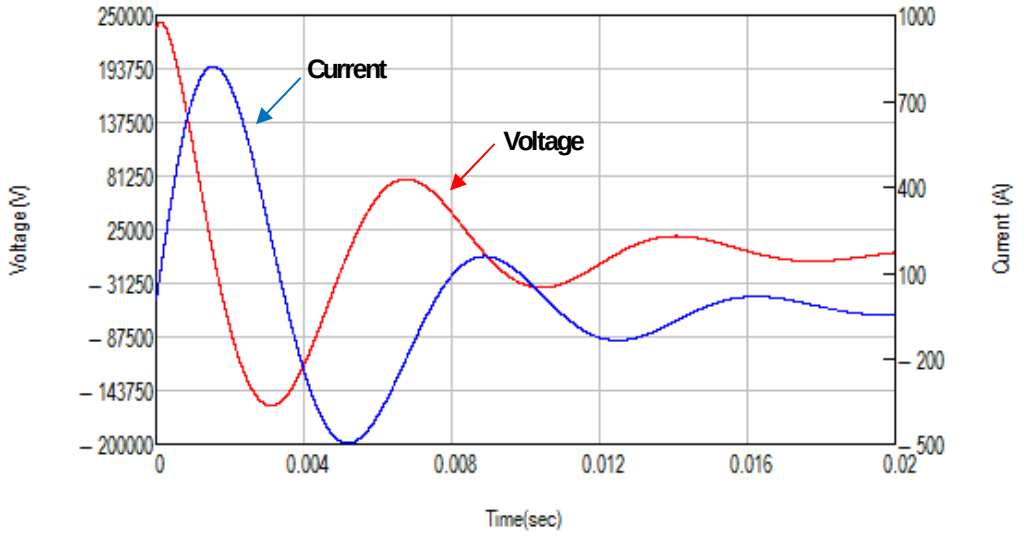

Figure 4.7: Filter reactor voltage and current using equivalent circuit and Laplace transform method

Using the reactor voltage that was just obtained, the current flow through the reactor arrester can be determined using Equation (4.21).

$$I_{arrL}(s)$$

$$= \frac{3.186\times10^7 s(2.369\times10^5 s^{10} + 1.216\times10^{19} s^9 + 1.56\times10^{32} s^8 + 1.002\times10^{36} s^7)\cdots}{(s+1.355\times10^3)(s+2.567\times10^{13})^2(s+63.753)(s+63.756)(0.277s+1.15\times10^8)\cdots}$$

$$\frac{\cdots + 1.665\times10^{39} s^6 + 1.544\times10^{42} s^5 + 1.143\times10^{45} s^4 + 2.581\times10^{47} s^3 \cdots}{\cdots (s+3.555\times10^3)\left(\frac{2.741\times10^4}{s}\right)\left(\frac{3.186\times10^7 s}{0.277s+1.15\times10^8}\right)\left(\frac{s}{5\times10^5}+1.15\times10^8\right)\cdots}$$

$$\frac{\cdots + 1.005 \times 10^{50} s^2 + 1.144 \times 10^{52} s + 3.698 \times 10^{53}}{\cdots (s + 72.947)(s^2 + 402.875s + 7.761 \times 10^5)(s^2 + 488.301s + 8.567 \times 10^5)} \quad (4.21)$$

To obtain the time response of the current, the inverse Laplace transform is used, and the current is expressed as follows:

$$i_{arrL}(t) = -2.06 \times 10^{-3}\, e^{-5.75 \times 10^{13} t} - 3.835 \times 10^{-3}\, e^{-63.753t} + 3.85 \times 10^{-3}\, e^{-63.756t} \cdots$$

$$\cdots + 2.603 \times 10^{3} \cos(857.626t) e^{-201.438t} + 2.583 \times 10^{7}\, \mathrm{t}\, \mathrm{e}^{-2.256 \times 10^{13} \mathrm{t}} \quad (4.22)$$

The plot of the reactor arrester current is presented in Figure 4.8. The result shows that a current magnitude of approximately 2 mA is obtained at the instant of closing operation. This small current magnitude is expected; since the resistance, representing the reactor arrester has a high value of 115 MΩ. The waveform obtained also demonstrates a sudden change in current occurred at the reactor arrester due to the switching operation. Particularly for reactor arrester, such an event gives rise to transient oscillations, which in turn can cause high overvoltages, unless suitably damped.

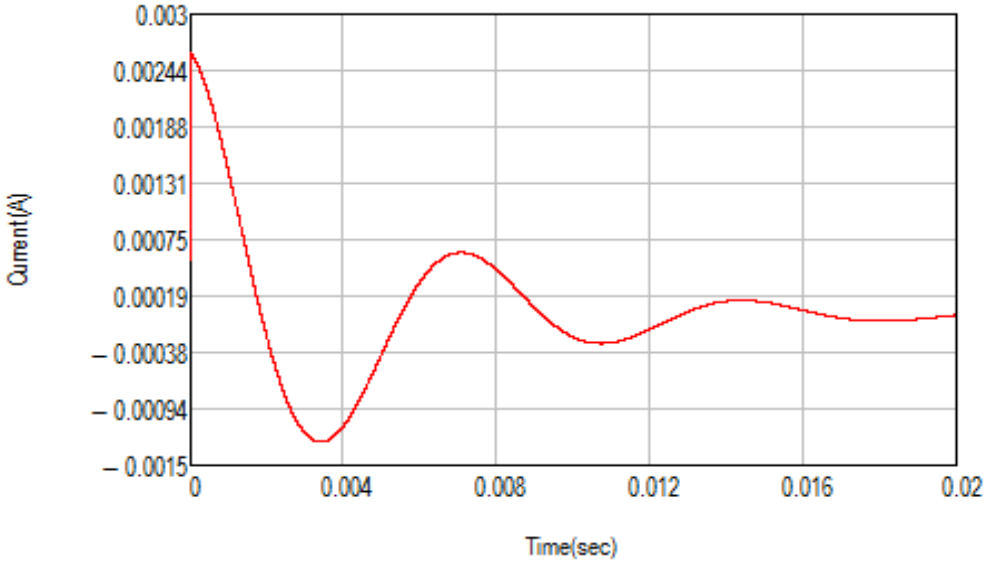

Figure 4.8: Current of the reactor arrester using equivalent circuit and Laplace transform method

4.3.4 Single-phase ATP/EMTP Simulation

In the previous section, an analytical approach that considers the switching of a circuit with zero initial conditions to a DC source was used to estimate the transient overvoltages of the MSCDN. In order to verify the calculated voltages and currents obtained, the circuit shown in Figure 4.2 is simulated in the ATP/EMTP program under the same switching condition. The current and voltage waveforms obtained by using analytical equations were compared with the waveforms computed by means of ATP/EMTP single-phase simulation.

Figure 4.9 shows current and voltage responses of the main capacitor computed from the simulation during the MSCDN energisation. The main capacitor current computed using ATP/EMTP simulation is obtained approximately 970 A. The computed main capacitor voltage has a magnitude of approximately 464 kV or 1.4 p.u. Furthermore, the oscillation frequency is determined around 147 Hz. These results illustrate that the main capacitor current and voltage predicted using analytical Equations (4.8) and (4.10), as well as the oscillation frequency are in good agreement with the data computed from the ATP/EMTP simulations.

Next, Figure 4.10 presents the simulated results of voltage and current of the damping resistor. Comparing these results with the corresponding waveforms obtained by analytical calculations as shown in Figure 4, suggests that the simulated voltage of approximately 219 kV is less than the calculated value of 238 kV obtained using Equation (4.12). Likewise, the computed resistor current of approximately 550 A is also less than 600 A, which is the current estimated using Equation (4.14). Reporting discrepancies are common and expected, and are believed to be due to

approximation made in solving those analytical equations, especially when analytical circuits are complicated and comprised of many L-C elements.

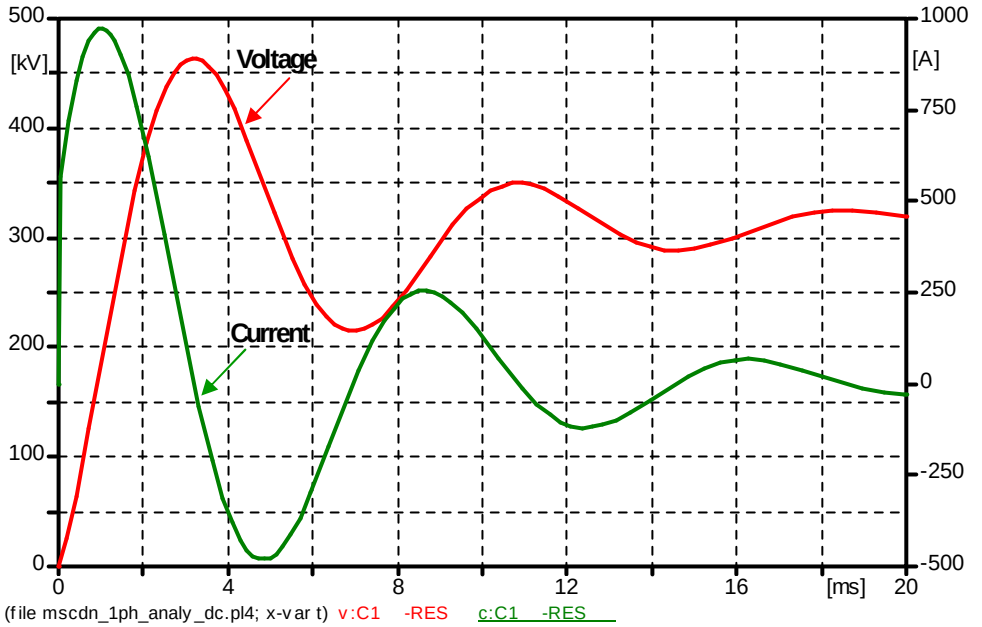

Figure 4.9: Main capacitor voltage and current computed by ATP/EMTP

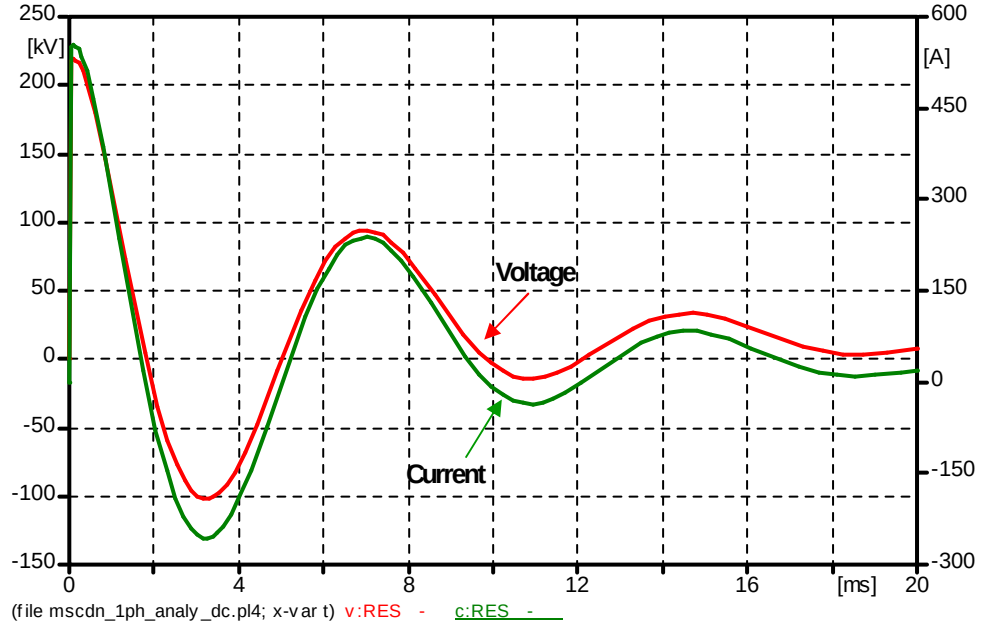

Figure 4.10: Damping resistor voltage and current computed by ATP/EMTP

Furthermore, the response of the resistor arrester current obtained using Equation (4.16) is compared with the ATP/EMTP waveform. Figure 4.11 depicts the simulation result of the arrester current. The resistor arrester current obtained from ATP/EMTP simulation is approximately 2.8 mA, which indicates a good agreement with the analytically calculated value.

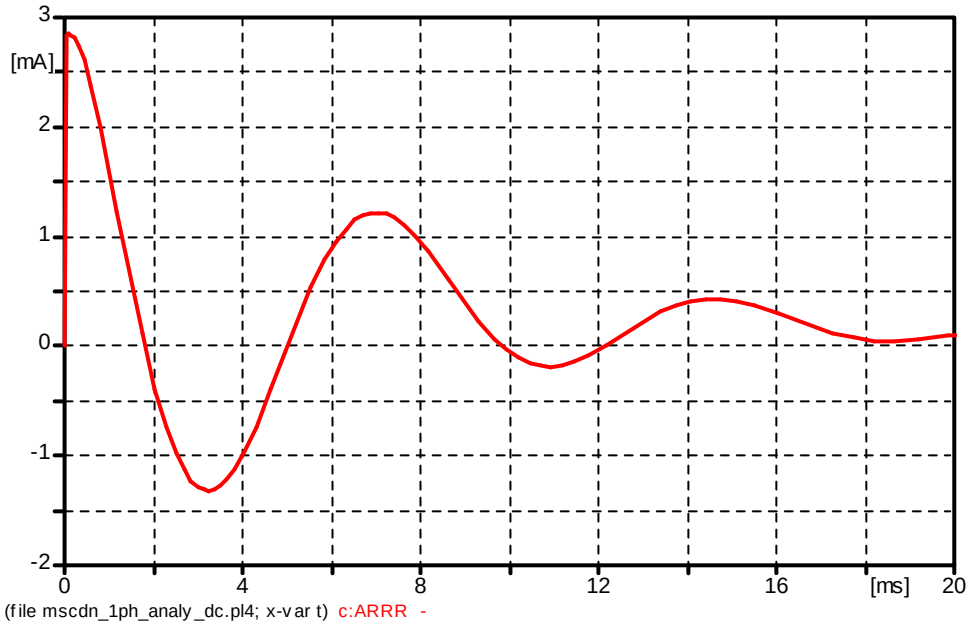

Figure 4.11: Resistor arrester current computed by ATP/EMTP

Finally, the voltage and current details at the filter reactor obtained by means of ATP/EMTP single-phase simulation are presented in Figure 4.12. These simulation results are compared with those waveforms calculated by analytical approach. The computed reactor current has a magnitude of 790 A, which is very close to the value calculated using Equation (4.20).

Furthermore, a different response was observed at the reactor voltage produced by the ATP/EMTP simulation. As can be seen, the transient voltage obtained has both high magnitude and high rate-of-rise. Following the closing of the switch, the reactor

voltage reaches a maximum peak of 217 kV within a time period of approximately 0.1 µs. The voltage magnitude is higher than 240 kV, which is the value of the reactor voltage calculated using Equation (4.18).

Figure 4.13 presents the response of the reactor arrester current. The current obtained has a magnitude of approximately 2 mA, increased rapidly from its minimum value in a short time period of 1 µs after the closing operation. The reactor arrester current obtained from ATP/EMTP simulation is found to be very close to the value calculated using Equation (4.22).

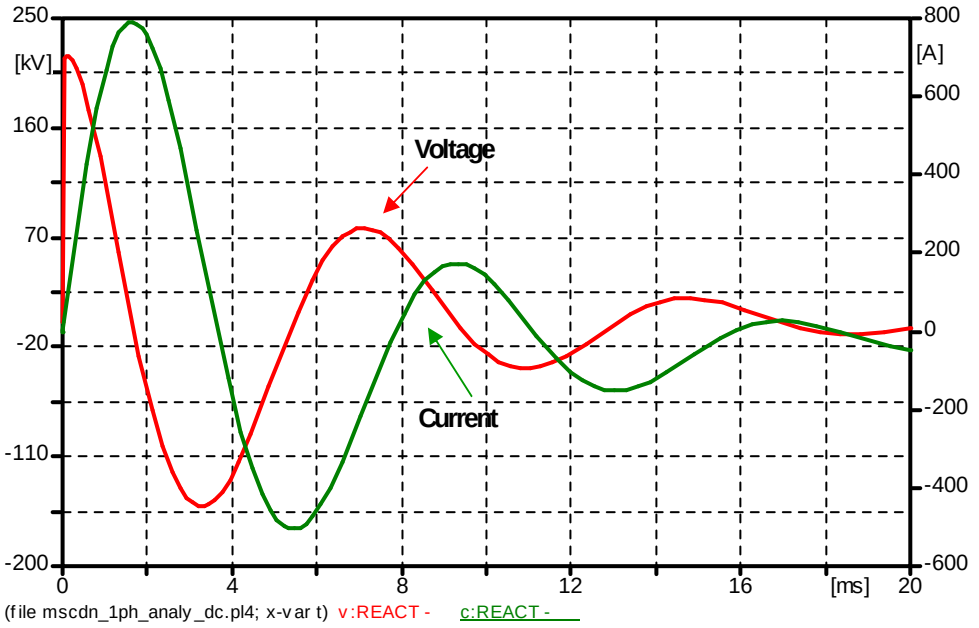

Figure 4.12: Filter reactor voltage and current computed by ATP/EMTP

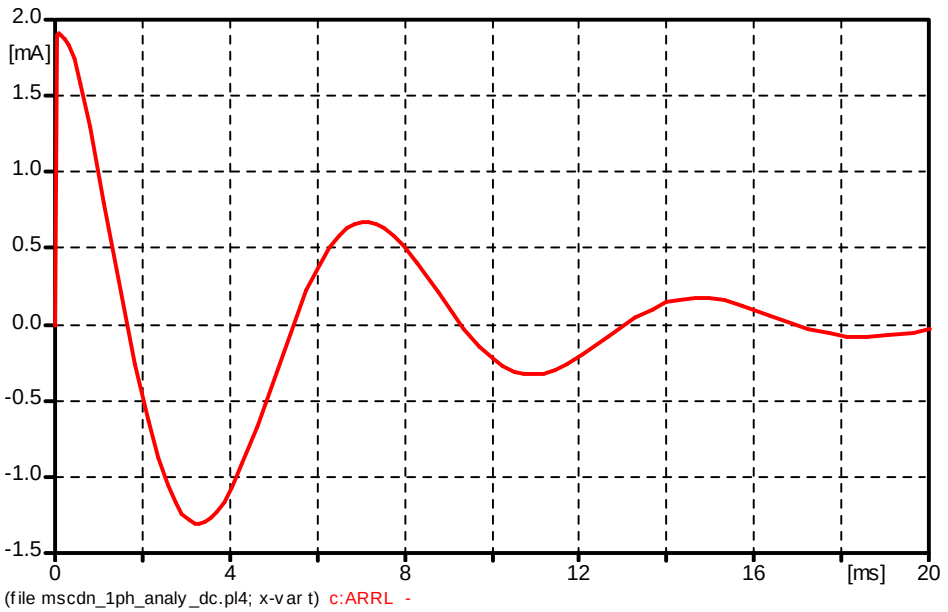

Figure 4.13: Reactor arrester current computed by ATP/EMTP

As shown, the single-phase circuit can also be used for analysing the maximum overvoltages taking place in the three-phase network. The maximum overvoltages during simultaneous closing of all three phases will occur on the phase where the voltage reaches its peak value at the closing instant [4.5]. It was shown that when the circuit in Figure 4.2 was subjected to DC voltage, high overvoltages and current transients were established, oscillating at a frequency determined by the main components of the MSCDN. The comparison of voltage and current responses obtained from the two calculation procedures (analytical and simulation) has produced satisfactory results, which indicates the satisfactory representation of the model. It was found that the analytical approach gives a better understanding of the whole interrupting process and gives a clear explanation of such complicated shapes of transient voltages. However, ATP/EMTP simulation gives more complete results considering all boundary conditions automatically. More importantly, chance to

make a mistake when putting in the input variables is also much smaller when using ATP/EMTP program.

4.4 Simulation of Transient Overvoltages in Three-phase MSCDN Networks in ATP-EMTP Program

A full simulation of the MSCDN routine energisation is performed by means of the ATP/EMTP program. The simulations were established through consideration of previous works surveyed in the literature review [4.7-4.11]. The objectives of the simulation are two-fold. First, this simulation study is intended to determine the worst-switching transients produced during the MSCDN energisation. In a practical application, a point-on-wave (POW) synchronised circuit breaker is usually employed to perform the switching duty of MSCDN [4.9]. However, in order to produce more conservative simulation results, the closing times of the circuit breaker are randomly specified, and the results are examined particularly when the circuit breaker is set to close at the instants corresponding to maximum and minimum phase A supply voltage [4.9].

The other objective of this simulation is to study the effect of transient stresses on the MSCDN components particularly, the filter reactor [4.1, 4.7, 4.8, 4.12]. The steady-state voltage across the reactor is usually low, since it is connected to the lower part of the MSCDN circuit. However, the reactor is usually susceptible to fast-fronted voltage transients, which will usually arise during filter start-up [4.12]. Furthermore, the rate of voltage change across the reactor is an important factor that influences the non-linearity of voltage distribution [4.7, 4.13]. Of equal importance is the current flow through the reactor. This current must be monitored as it will

potentially increase both the losses in the reactor and the voltage across the reactor winding [4.7].

4.4.1 Modelling Procedures

The values of each passive element of the MSCDN are assigned according to the values as shown in Figure 4.2. Accordingly, the ATP/EMTP simulation circuit of the MSCDN in a three-phase network is constructed as in Figure 4.14. The network components which are included in the modelling consist of a 225 MVar MSCDN connected directly to a 400 kV terminal through a circuit breaker.

The 400 kV supply network is represented by a three-phase voltage source behind a parallel combination of its short-circuit impedance and surge impedance seen from the capacitor banks terminal. The surge impedance is taken at the typical value of 150 Ω. The short-circuit impedance is estimated based on the short-circuit current level of 21 kA (rms) at a 400 kV substation and a typical value of X/R ratio of 10 [4.14]. The switching device is assumed to be an ideal circuit breaker, and is represented by a three-phase time-controlled switch of the ATP component. Finally, the MSCDN is represented by lumped elements, i.e. R,L and C in accordance with the topology shown in Figure 4.1.

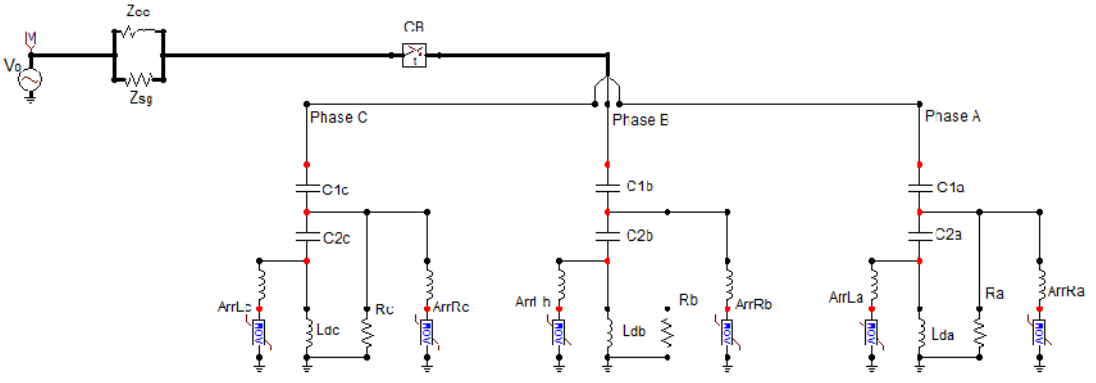

Figure 4.14: ATP/EMTP three-phase simulation circuit

In order to limit the required insulation levels of the equipment below the main capacitor, a surge arrester is placed across both the reactor and the resistor [4.9]. These arresters are the zinc-oxide (ZnO) gapless type. In the simulated model, the surge arrester is represented by the non-linear resistor model Type-92 of ATP components. Table 4.1 presents the main electrical data of the arresters.

Table 4.1: Main electrical data of the surge arresters

Parameters	Reactor arrester	Resistor arrester
Type designation	EXLIM-P (ABB)	EXLIM-P (ABB)
No. of parallel columns	1	1
Rated Voltage	144 kV (rms)	96 kV (rms)
TOV capability (1 sec)	167 kV (rms)	111 kV (rms)
Energy capability	7 kJ/kV of rated voltage	7 kJ/kV of rated voltage
Protection Level (Switching)	290 kV (at 2 kA)	194 kV (at 2 kA)
Protection Level (8/20 µs)	332 kV (10 kA)	221 (10 kA)

4.4.2 Simultaneous Closing of all Three Poles at Instants of Voltage Maximum and Minimum

Using the system representation described in the previous section, a computation of switching transients on the MSCDN was conducted using the ATP/EMTP program. In the simulations, all three poles of the circuit breaker are assumed to close simultaneously. The first simulation investigated is the ideal switching case. The simulation investigates transient stresses resulting from the energisation of the MSCDN at the instant coinciding with the minimum value of phase A supply voltage. The second simulation investigates the worst switching case; this simulation aims to determine the worst transients produced when the MSCDN is energized at the moment coinciding with the maximumvalue of phase A supply voltage.

4.4.3 Voltage and Current Responses of the Main Capacitor

Figure 4.15 and 4.16 respectively show the voltage and current responses generated at the main capacitor. Note that the waveforms generated in the worst switching cases are represented by the red line, while the green line represents waveforms obtained for the ideal switching cases. The current flows through the shunt-connected capacitor bank, and any devices connected in series with this capacitor bank are directly affected by the magnitude and shape of the voltage waveform as well as by the manufacturer's capacitance tolerance. The ATP computed waveform in Figure 4.15 shows that the main capacitor current reached approximately 1 kA during the worst switching case; this magnitude is twice the value attained in the ideal switching case. However, transient overcurrents are generally not a concern, since the capacitor units are usually designed to handle much higher currents than those resulting from filter switching [4.1, 4.15].

Figure 4.16 shows the voltage responses obtained at the main capacitor. As can be seen, transient overvoltages are barely noticeable in both switching cases and the voltage magnitudes remain well within the specified voltage limit.

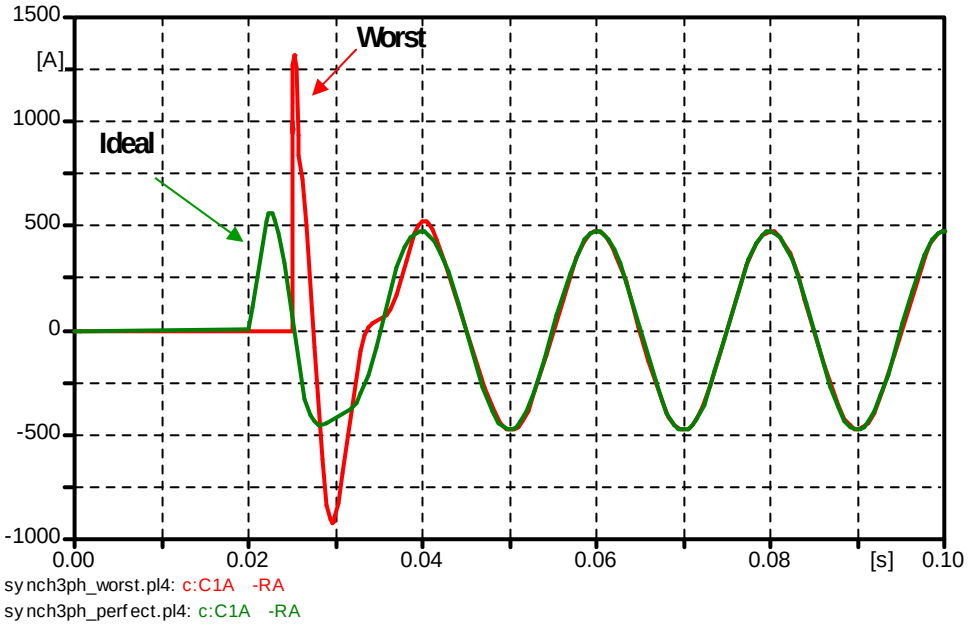

Figure 4.15: Main capacitor current for ideal and worst switching cases

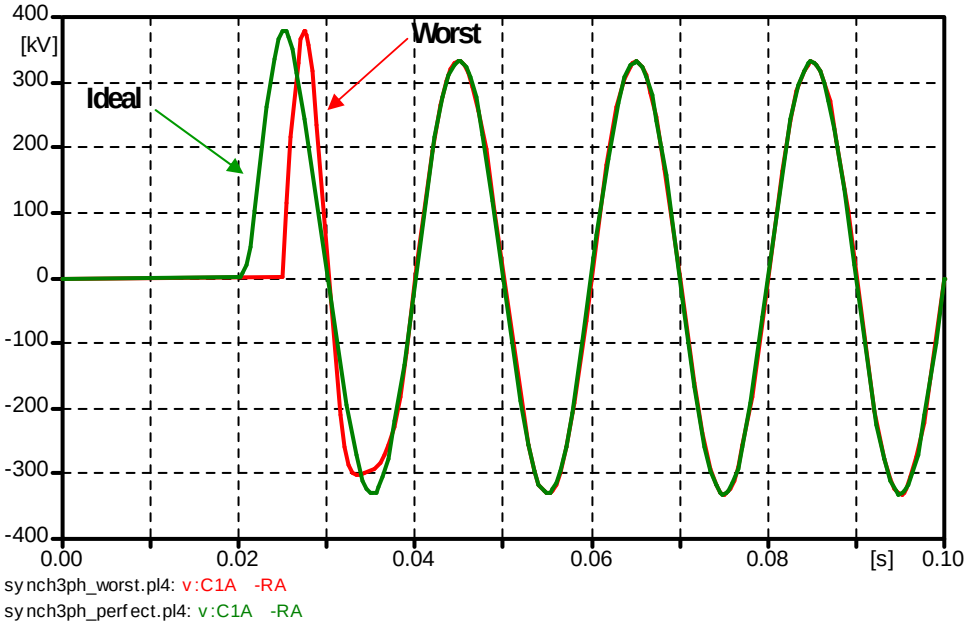

Figure 4.16: Main capacitor voltage for ideal and worst switching cases

4.4.4 Voltage and Current Responses of the Damping Resistor

Ideally, there is very little current flowing through the damping resistor at steady state, since it is placed across the series C_2-L_f branch, which is tuned to the

fundamental frequency. However, there might be some losses that arise from detuning of the filter caused by component tolerances [4.9]. The currents that flow through the resistor as a result of the switching operation are shown in Figure 4.17. During the ideal switching case, the current obtained is about 170 A. This value is greatly increased to 470 A in the worst switching case. Figure 4.18 presents the computed resistor voltage for both switching cases. As expected based on the observations above, a magnitude of 200 kV is the highest overvoltage at the resistor obtained during the worst switching case.

Furthermore, energy dissipation in the damping resistor during the worst switching case is presented in Figure 4.19. The result shows that the energy dissipation is approximately 160 kJ during the 5 ms duration.

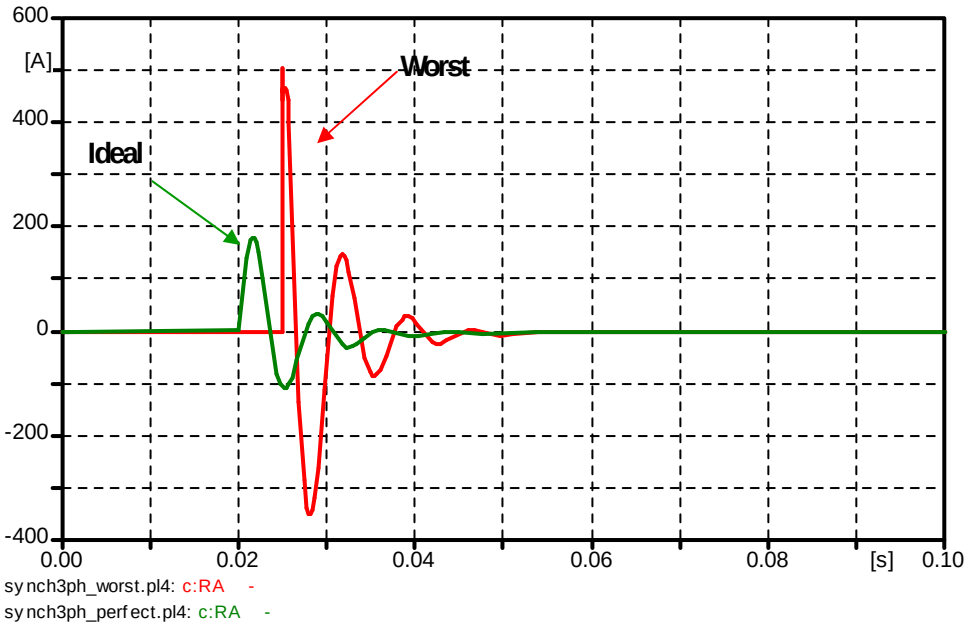

Figure 4.17: Damping resistor current for ideal and worst switching cases

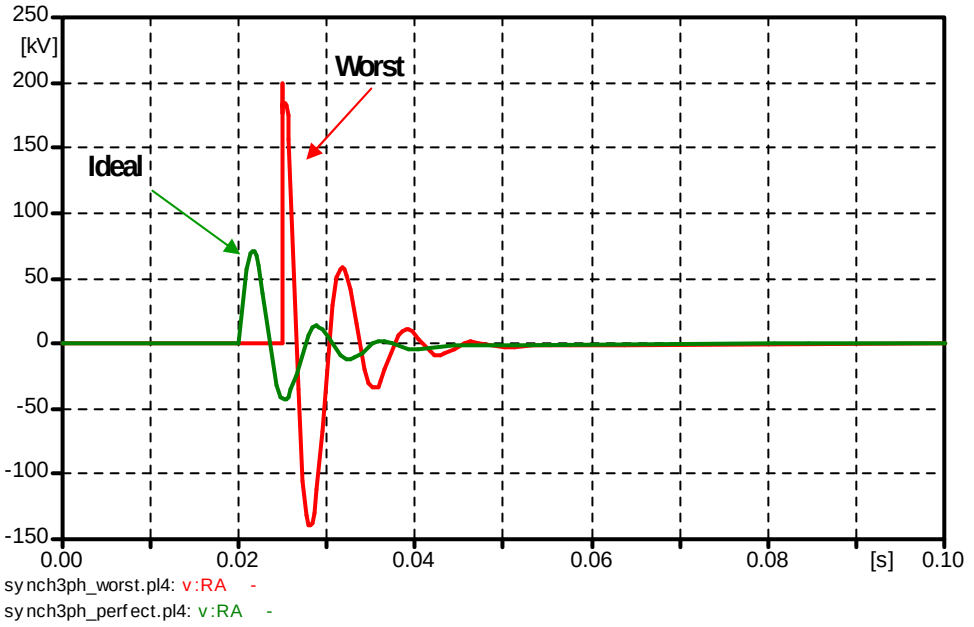

Figure 4.18: Damping resistor voltage for ideal and worst switching cases

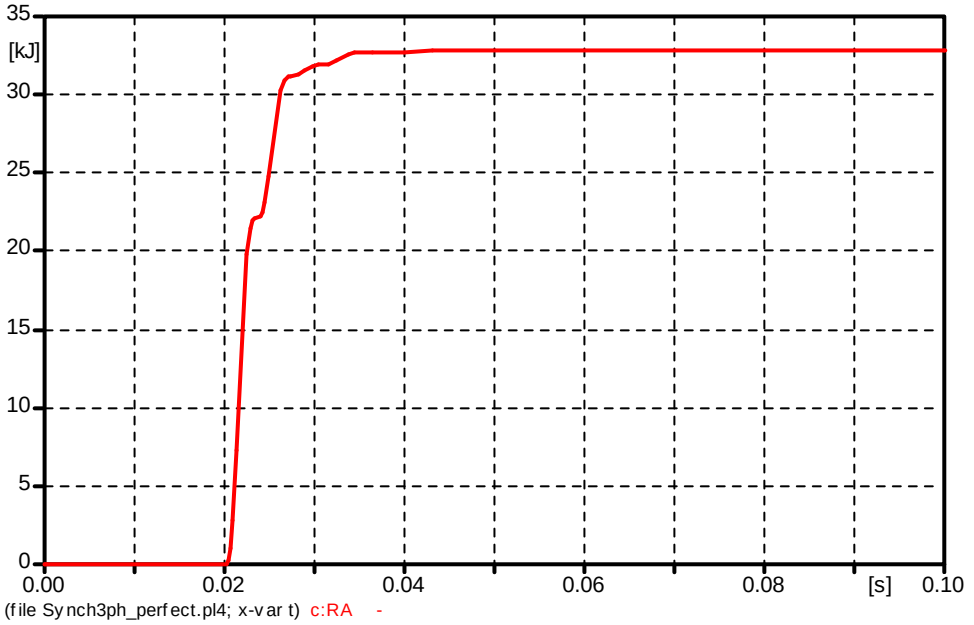

Figure 4.19: Energy dissipation in the damping resistor for worst switching case

4.4.5 Energy Dissipation in the Resistor Arrester

In this study, the rated energy capability of the arrester based on the maximum single-impulse energy stress is given as 7 kJ/kV (U_r) [4.4]. This is the maximum permissible energy to which an arrester may be subjected in a single pulse of 4 ms or

longer, and remain thermally stable against the specified TOV capability and the continuous operating voltage (U_c) [4.4]. Accordingly, the energy dissipation capability of the resistor arrester used is calculated as 7x96=672 kJ [4.4].

Referring to the simulation results shown in Figure 4.18, the resistor voltage is determined and its value is about 60 kV in the ideal switching case. The energy dissipation in the arrester obtained for this case is small, as shown in Figure 4.20. However, when energising the MSCDN at the worst time instant, the highest overvoltage approximately 200 kV was obtained at the damping resistor. As a result, the energy dissipation in the resistor arrester is increased to around 60 J, as shown in Figure 4.20.

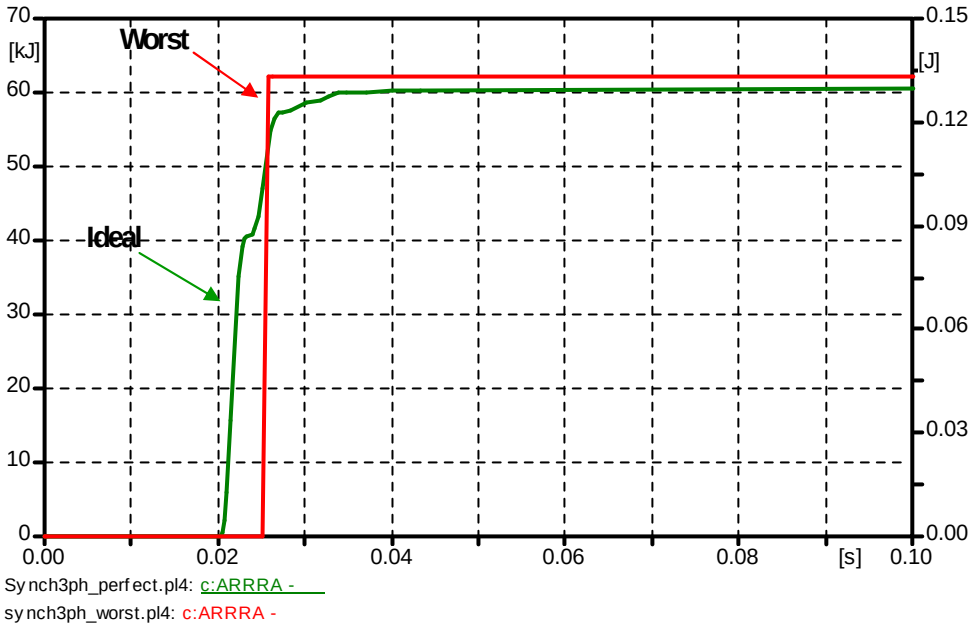

Figure 4.20: Energy dissipation in the resistor arrester for ideal (right scale) and worst (left scale) switching cases

4.4.6 Voltage and Current Responses of the Filter Reactor

In any operating state of the reactor, the voltage stress across the reactor surface should be maintained at a level well below the voltage that could lead to

deterioration of the external insulation [4.13]. Likewise, it is also important to keep the turn-to-turn voltage stress well below the level that could lead to internal insulation damage [4.1].

Figures 4.21 and 4.22 present the current and voltage occuring at the filter reactor during the energisation of MSCDN. The voltage responses presented in Figure 4.22 show that the reactor voltage is kept well below the rated value when the energisation was made at an ideal time. However, if the MSCDN is energised at the worst time instant during the cycles, the resulting voltage has the highest magnitude of 196 kV. More importantly, the generated transient manifests itself in the form of a voltage spike and persists for a short period of nanoseconds. The voltage spike plotted with reduced time scale is shown in Figure 4.23.

Aside from the voltage magnitude, the rate of rise and duration of the voltage spike are also crucial parameters in ensuring a reactor's safe service condition. The rate of voltage rise defined in BS 62068-31 [4.13] is expressed as:

$$\frac{dV}{dt} = \frac{0.8 \times V_m}{(t_{90\%} - t_{10\%})} \tag{4.23}$$

where V_m is impulse voltage magnitude and $t_{90\%}$ -$t_{10\%}$ is the time interval between the 10% and 90% magnitude of the zero-to-peak impulse voltage. Accordingly, the rate-of-rise for the voltage spike shown in Figure 4.23 can be expressed as:

$$\frac{dV_{reactor}}{dt} = \frac{0.8(199.523\ kV)}{(90ns - 10ns)} = 1995.23 \tag{4.24}$$

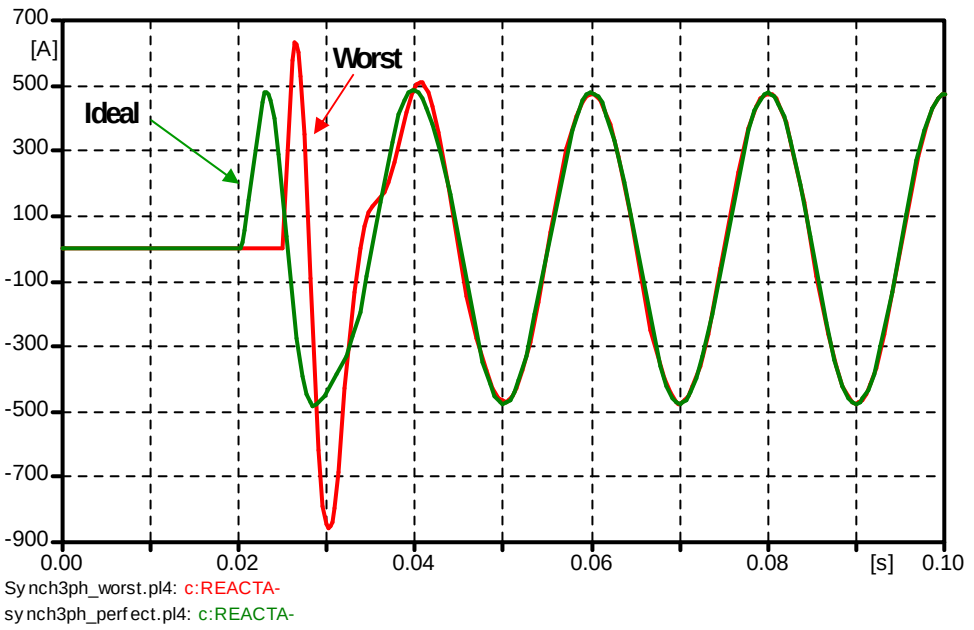

Figure 4.21: Filter reactor current for ideal and worst switching cases

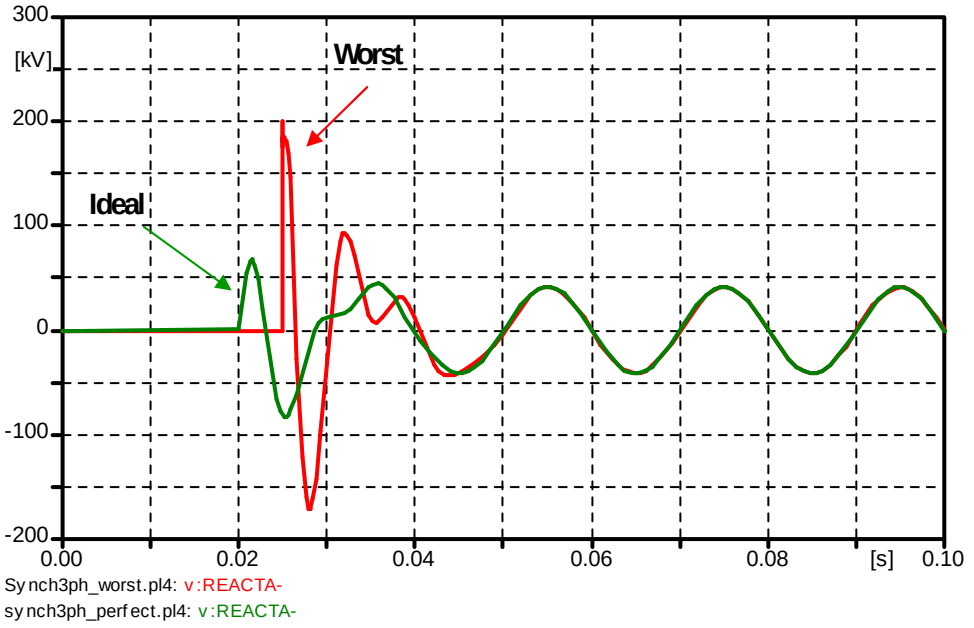

Figure 4.22: Filter reactor voltage for ideal and worst switching cases

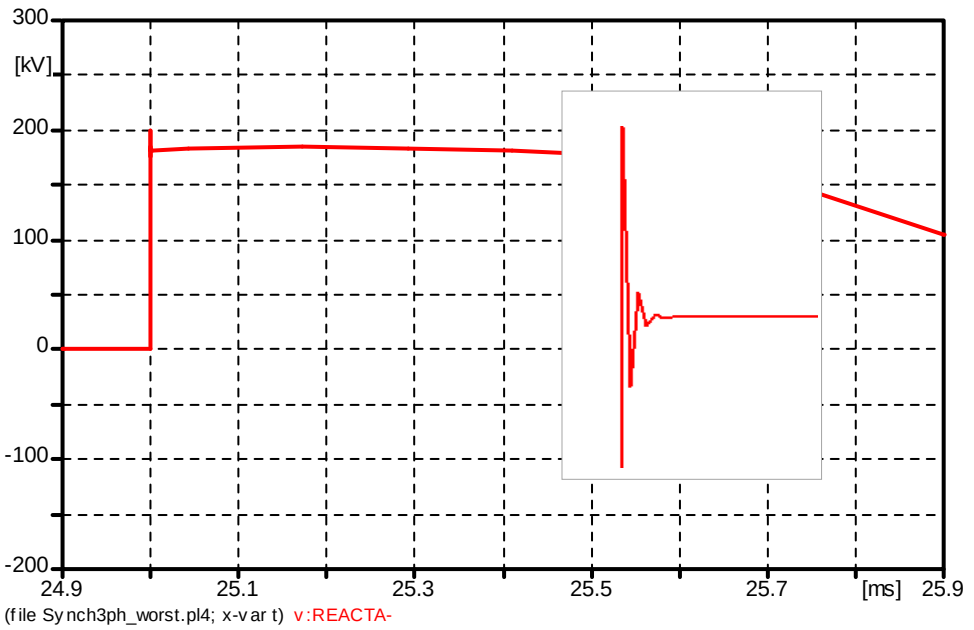

Figure 4.23: Voltage spike at the filter reactor in worst switching case

4.4.7 Energy Dissipation in the Reactor Arrester

Figure 4.24 shows the energy dissipation in the surge arrester installed across the filter reactor. The actual maximum steady-state voltage across the arrester is approximately 42 kV. It is known that the dimensioning voltage across the reactor arrester is the voltage peak that occurs when the MSCDN undergoes energisation [4.9] . With reference to the results presented in Figure 4.22, the reactor voltage in ideal switching case is approximately 60 kV. In worst transient case, the reactor voltage increases to the highest magnitude of about 200 kV. In the simulation, the selected rated voltage of the arrester is above 144 kV. Therefore, there is negligible energy dissipation in the reactor arrester for both switching operations, as presented in Figures 4.24.

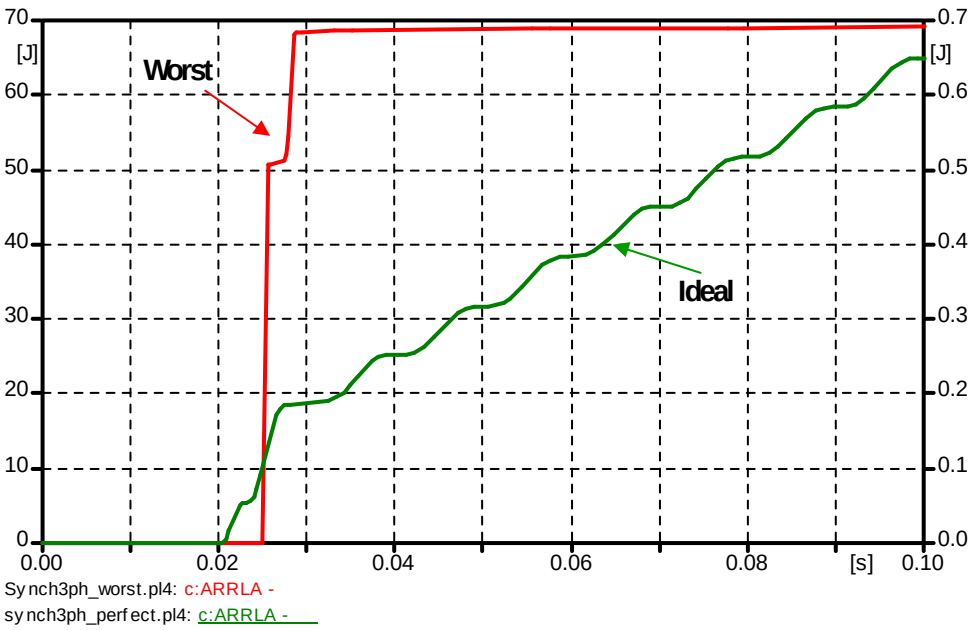

Figure 4.24: Energy dissipation in the filter reactor arrester for ideal (right) and worst (left) switching cases

4.5 Conclusion

In this chapter, computation of transient voltages and currents at the main capacitor, the damping resistor, and the reactor were determined using both an analytical approach and ATP/EMTP simulations. The results show that energisation of MSCDN at unfavourable instants produced the worst transients at almost all components. As a result of these switching investigations, the filter reactor is identified as one location that experiences the maximal overvoltage. The reactor voltage obtained in the worst switching case will be investigated in more detail in Chapter 5. The analysis will include detailed modelling of the reactor by taking into account high-frequency elements of the reactor.

Chapter 5: A New Proposal for the MSCDN Air-core Reactor Modelling

5.1 Introduction

In chapter 4, a voltage spike at the air-core filter reactor when the circuit breaker closed at unfavourable point-on-wave instants was observed. This voltage transient was computed at the reactor HV terminal; however, the prediction of the voltage distribution along the windings is difficult to achieve. Hence, the developed transients require a more complex model to represent the reactor. In Chapter 5, a proposal for the MSCDN air-core reactor modelling based on an equivalent circuit model is described. The chapter is organised as follows: after a brief discussion of the fast transients in the winding is described, Section 5.3 introduces a modelling technique for reactor winding based on a lumped parameter equivalent circuit. A proposed model is then described in Section 5.4, where an equivalent circuit model of an MSCDN reactor is shown. This is accompanied with derivations of analytical expressions that are used to obtain the circuit components of the model. Section 5.5 presents the evaluation of transient performances of the reactor model by means of the ATP/EMTP program.

5.2 Fast-Fronted Transient Waveforms

For AC system voltages of power frequency, the voltage distribution is linear with respect to the number of turns and can be calculated exactly. For the calculation of the impulse voltage distribution in the windings, they are required to be simulated in terms of an equivalent circuit consisting of lumped R,L, and C elements. Chapter 4 demonstrated that a fast transient overvoltage at the filter reactor was produced when

the MSCDN was energised at an unfavourable time instant. In order to address the identified problem, a detailed modelling of air-core reactor, which accounts the effect of stray inductances and capacitances of the winding, is required.

Fast-front switching overvoltages are observed when equipment is connected to or disconnected from the system via short connections, mainly within a substation [5.1]. The transferred surge has both the capacitively and inductively transferred components superimposed on the power frequency voltage [5.1]. Initially, the winding responds as a system of capacitances, producing mainly capacitively-transferred components, which typically lie within the MHz-range frequencies [5.1]. The inductively-transferred components are evident afterward, and they are changed in time by the shape and amplitude because the distribution of the voltage along the winding is time-dependent [5.1].

At lower frequencies, the effect of the stray capacitances of the winding is negligible [5.2-5.4]. This means that the same current is flowing through all turns, resulting in the same voltage drop and uniform voltage distribution across the winding. A different situation is observed when the winding is subjected to high-frequency transients. The capacitances of the reactor winding at high frequencies have lower impedance than its inductances; this difference in levels causes a variation in currents for each winding turn [5.3]. The result of this will be different voltage drops across each winding segment, and a nonlinear voltage distribution along the reactor length can be seen [5.3].

5.3 Detailed Modelling of the Air-core Reactors

Perhaps the simplest transient model of the reactor is that which consists of an inductance and a certain capacitance-to-ground [5.2]. Such a model can only provide

information about the overvoltages generated at the reactor terminals. The degree of detail in modelling of any power equipment is highly dependent upon the type of study being conducted, as is emphasised by Greenwood [5.2]:

> "A comprehensive, detailed model is not desirable or tractable, what is needed is something sufficient to answer the specific questions being asked (p. 327)".

An internal model is required in order to understand how the reactor winding will behave when it is subjected to a transient injection. However, a model that will reveal these internal stresses should not be so comprehensive that it is not easily dealt with, nor should it require confidential design parameters to develop the model [5.2]. Furthermore, the model should not be so unwieldy that it is impractical to apply it to full-scale power devices, for example, a model that requires very long simulation times [5.2]. Generally, all of the criteria are fulfilled with the use of lumped circuit models [5.5-5.10].

Many papers concerned with the modelling of a winding have been published. Detailed modelling of a winding would require that every turn be represented and that all inductive and capacitive mutual couplings with every other turn be included [5.2, 5.3]. Popov, et. al [5.11] described the formulation of a transmission-line model for very fast transient solutions. This model is purely mathematical and takes into account the frequency dependent core and copper losses. The model has been successfully applied to evaluate fast transient voltages in distribution transformer windings with a rating of 15 kVA. Popov, et. al [5.12] have formulated a lumped parameter model based on discrete telegraphist's equations. The model was used to study voltage transients along transformer windings during circuit breaker

prestriking. Enohnyaket [5.4] presented a detailed distributed model of air-core reactors based on the partial elements equivalent circuits (PEEC), which can be used in both time and frequency domain analysis. This model considers in detail the electromagnetic couplings between parts of the individual windings. Each winding turn is modelled as finite number of interconnected bars. The model parameters mainly the partial inductances, the coefficients of potential, and the resistances are computed from the geometry of the bars using analytical routines. The PEEC approach to create electromagnetic models involves five computational phases, and is computationally expensive.

As the development of a model to calculate the voltage distributions in windings of complex apparatuses, such as three-phase transformers is very complex, the approach used in this thesis is to develop an accurate model representing a simple single-layer air-core reactor. A lumped parameter model approach is chose to represent a detailed model of an air-core reactor [5.5-5.10]. Due to close similarity in the physical construction, the derivation of a detailed model of an air-core reactor can be made according to works described for transformers [5.13-5.17]. The lumped components of an equivalent circuit are estimated using a set of analytical equations, which are derived based on the physical geometry, the winding, and the insulation material of the air-core reactor. Once all the RLC elements of the windings are obtained, the model is then implemented in the ATP/EMTP simulations to establish the voltage distribution along the reactor winding.

5.4 Derivation of Lumped Parameter Equivalent Circuit

To model the circuit using a lumped parameter approach, the winding is divided into sections that are so short, that the conductive current through the section is

approximately constant [5.2]. The air-core reactor investigated in this study has a height of 2.65 m and an inner diameter of 0.9 m. The reactor was placed in a vertical position at a distance of approximately 0.1 m above the ground plane. The aluminum conductor of the windings has a diameter of 2 mm, and is individually insulated by Mylar polyester film of 50 µm thickness. To account for the relatively large size of the coil, in the following analysis, it is assumed that the reactor winding is physically subdivided into *k* sections of equal length and radius [5.15]. Figure 5.1 illustrates the division of the reactor winding and the physical location of the sections above ground. Assuming that all sections are of sufficiently short length, it is possible to use a lumped parameter approach to analyse the winding response.

In this computation, the reactor length was subdivided into 10 sections having equal axial length along the reactor column. An equivalent circuit model to represent the winding of a vertically-mounted reactor is presented in Figure 5.2. For each winding section, the winding-turns inductance L_{wk}, the inter-turn shunt capacitance C_{tk}, the stray capacitance-to-ground C_{gk}, the winding series resistance R_{wk}, and the inter-turn insulation shunt resistance R_{pk} are considered [5.15].

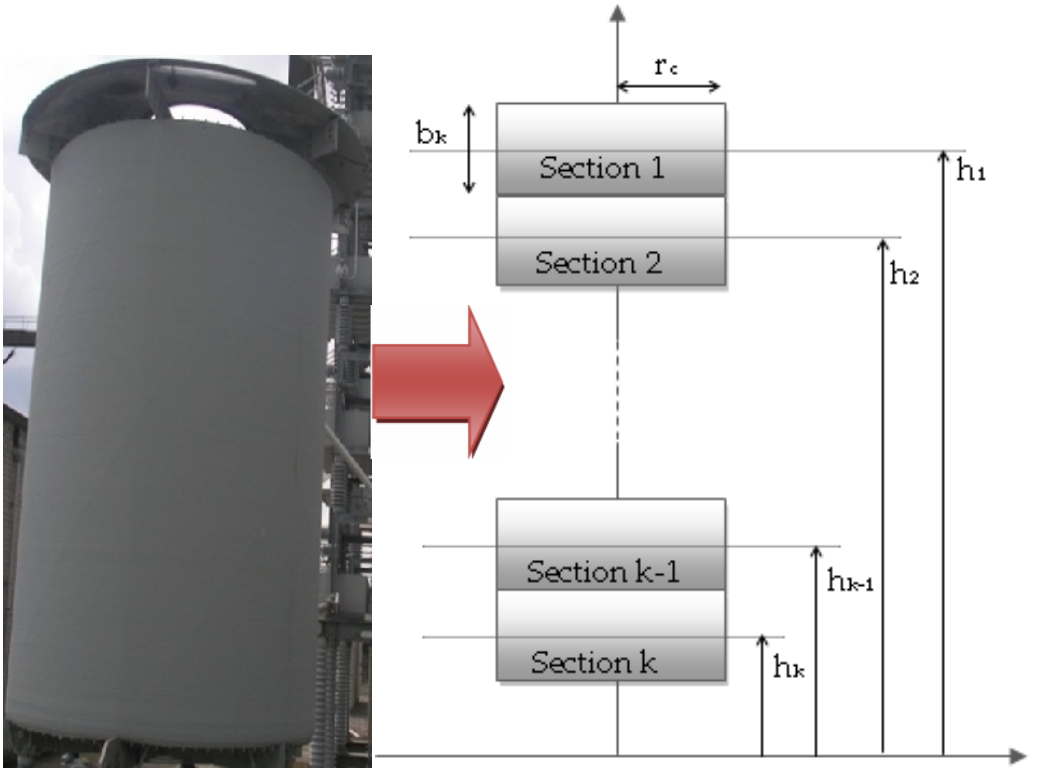

Figure 5.1: Division of air-core reactor winding

where,

h_k: distance from the ground to the centre of section k

r_c: radius of the reactor

b_k: length of section k

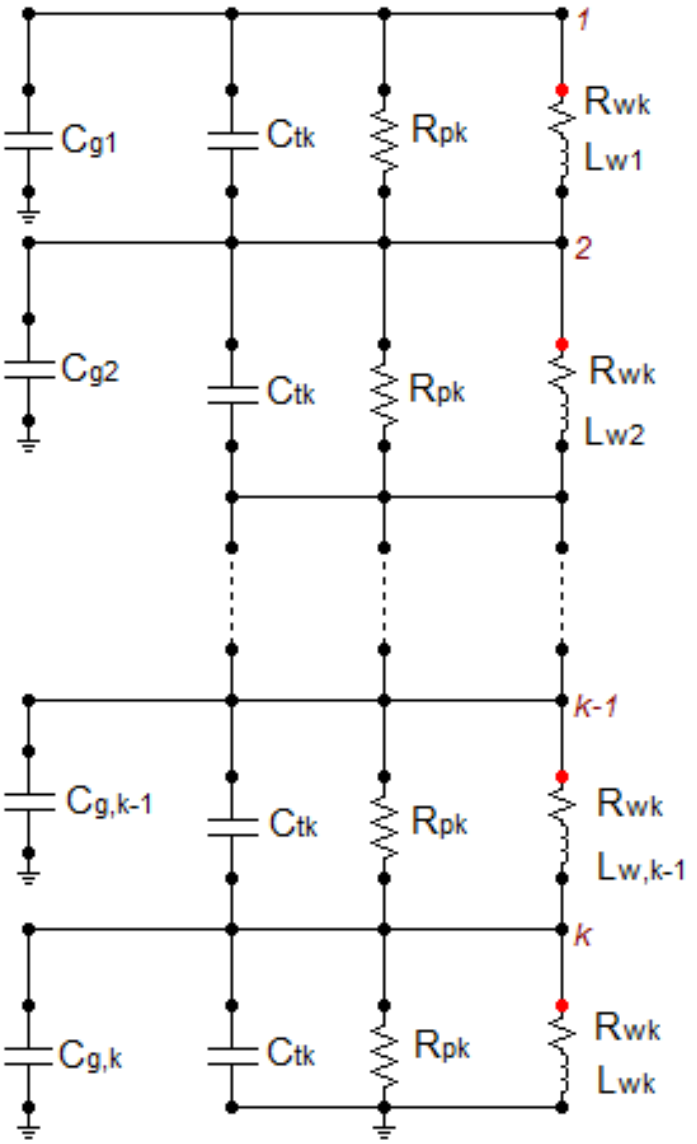

Figure 5.2: An equivalent circuit model of *k* sections reactor winding

where,

L_{wk}: winding-turns inductance

R_{wk}: winding series resistance

R_{pk}: inter-turn insulation shunt resistance

C_{tk}: inter-turn shunt capacitance

C_{gk}: stray capacitance-to-ground

5.4.1 Computation of Self and Mutual Inductances of the Winding

Any conductor, whether straight or wound in a coil, has inductance [5.18]. The magnetic field around the winding conductors and between the winding sections respectively were represented by the self and mutual inductances [5.18]. In this thesis, both self and mutual inductances were estimated using a well-established equation as cited by Grover [5.19]. For the self inductance, a formula devoted for single-layer coils on cylindrical winding forms was used and applied for all winding sections shown in Figure 5.2, given their similarity in construction.

Self inductances are the same for turns belonging to the same layer of winding. Equation (5.1) allows estimation of the section self inductance [5.19]:

$$L_{sw} = \frac{0.002\pi^2 a_t^2 N_k^2 K}{b_k/2a_t} \qquad (5.1)$$

where

L_{sw} self-inductance of section *k* (mH)

a_t mean radius (cm)

N_k number of turns of section *k*

K Nagaoka's constant

b_k length of section *k* (cm)

Variable *K* in Equation (5.1), termed Nagaoka's constant, can be obtained from a set of the lookup tables provided by Grover [5.19]. The tabular value of the Nagaoka's constant ranges from 0 to 1, and is functions of the diameter ($2a_t$) and length (b_k) of the coils. There are a case where interpolation of the Nagaoka's constant is needed; however, for approximate calculation, simple interpolation in the tables will suffice. For better accuracy of the results, the second-order differences should be considered

when interpolating the values [5.19]. In this work, the interpolation of the required value is carried out in the MATLAB program using the Newton interpolation method, up to the second difference.

For the mutual inductances, Grover's formula for calculating the mutual inductance of the coaxial single-layer coils was used [5.19]. The formula derived for the mutual inductances was obtained based on the geometry shown in Figure 5.3, where $2m_1$ is the axial length of coil 1, $2m_2$ is the axial length of coil 2, and S is the separation of the two coil centers [5.19]. The parameter S indicates whether, the coils are partially inside, completely inside, or completely outside each other [5.19]. The parameter a_t is the radius of the smaller coil 1, while parameter A_t represents the larger coil 2 radius.

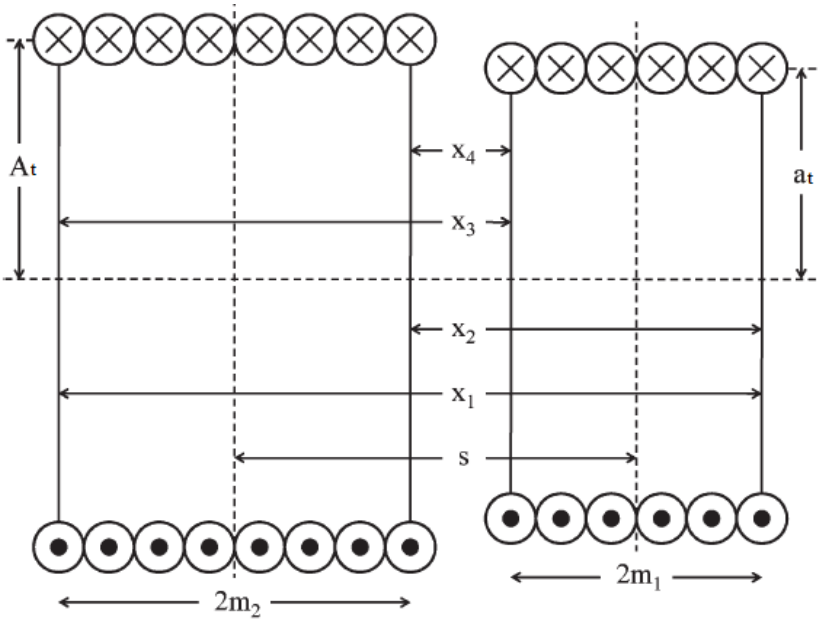

Figure 5.3: Basic geometry of two coaxial single-layer coils [5.19].

First, the mutual inductance is given by the sum of four elliptic integrals, which are functions of the four distances measured between the coils [5.19].

$$x_1 = s + (m_1 + m_2)$$

$$x_2 = s + (m_1 - m_2)$$

$$x_3 = s - (m_1 - m_2) \quad (5.2)$$

$$x_4 = s - (m_1 + m_2)$$

Second, in addition to the four axial distances, the diagonal distance of the coils should be considered when calculating the mutual inductances. The following equations provide the diagonal distances between the coils [5.16].

$$r_1 = \sqrt{x_1^2 + A_t^2}$$

$$r_2 = \sqrt{x_2^2 + A_t^2} \quad (5.3)$$

$$r_3 = \sqrt{x_3^2 + A_t^2}$$

$$r_4 = \sqrt{x_4^2 + A_t^2}$$

Finally, the mutual inductance between adjacent and non-adjacent sections of the reactor winding is performed using Grover's general formula [5.19]:

$$M_{k,k+1} = 0.002\,\pi^2 a_t^2\, n_k^2 [r_1 B_1 - r_2 B_2 - r_3 B_3 + r_4 B_4] \quad (5.4)$$

where

$M_{k,k+1}$ mutual inductance between section k and section k-1 (mH)

a_t mean radius (cm)

n_k winding density (turns/cm)

r_n diagonal distances between sections (cm)

B elliptic integral values

The variable B in this equation is the elliptic integral values and is given in Grover's tables according to the two look-up constants represented in Equations (5.5) and

(5.6):

$$\rho_n^2 = \frac{A_t^2}{r_n^2} \tag{5.5}$$

$$\alpha = \frac{a_t}{A_t} \tag{5.6}$$

For two equal radius coils, the value of α in Equation (5.6) is equal to 1; hence, the variable *B* is determined only from the axial and the diagonal distances between the two mutual coils. For this case, a specific lookup table of variable *B* for coils having equal radius and length is provided [5.19]. Again, a simple linear interpolation method is needed to approximate the value of parameter *B*, which is not directly available from the lookup table.

In this work, MATLAB mathematical analysis software is used to calculate Grover's self and mutual inductances given by Equations (5.1) and (5.4), respectively. Ultimately, the total inductance of one section, L_{wk} is obtained as the sum of the self-inductance of the section and the contributions of mutual inductances due to all of the other sections [5.19]. Table 5.1 presents the calculated self and mutual inductances obtained for each section of the reactor winding. The diagonal elements of the table represent the self inductance of each winding section. The off-diagonal elements show the mutual inductance between adjacent and non-adjacent winding sections.

Table 5.1: Computation of self and mutual inductances (mH) using Equations 5.1 and 5.4 respectively

	Coil 1	Coil 2	Coil 3	Coil 4	Coil 5	Coil 6	Coil 7	Coil 8	Coil 9	Coil 10
Coil 1	18.245	7.713	2.896	1.359	0.720	0.418	0.260	0.172	0.119	0.086
Coil 2	7.713	18.245	7.713	2.896	1.359	0.720	0.418	0.260	0.172	0.119
Coil 3	2.896	7.713	18.245	7.713	2.896	1.359	0.720	0.418	0.260	0.172
Coil 4	1.359	2.896	7.713	18.245	7.713	2.896	1.359	0.720	0.418	0.260
Coil 5	0.720	1.359	2.896	7.713	18.245	7.713	2.896	1.359	0.720	0.418
Coil 6	0.418	0.720	1.359	2.896	7.713	18.245	7.713	2.896	1.359	0.720
Coil 7	0.260	0.418	0.720	1.359	2.896	7.713	18.245	7.713	2.896	1.359
Coil 8	0.172	0.260	0.418	0.720	1.359	2.896	7.713	18.245	7.713	2.896
Coil 9	0.119	0.172	0.260	0.418	0.720	1.359	2.896	7.713	18.245	7.713
Coil 10	0.086	0.119	0.172	0.260	0.418	0.720	1.359	2.896	7.713	18.245
Sum (mH)	31.901	39.528	42.305	43.492	43.952	43.952	43.492	42.305	39.616	31.989

5.4.2 Computation of the Winding Series Resistance

Although the current distribution in the winding conductor is non-uniform at high frequency due to skin and proximity effects, the difference between the cross-section of each conductor compared to the cross-section of the whole winding is small. Hence, it is assumed that the current distribution in the whole winding cross-section is uniform.

The series resistance, R_{wk}, represents the total current-dependent losses of the reactor, which include the winding ohmic losses, the proximity effect, and the stray field losses caused by the large transverse magnetic field to which the conductors are subjected [5.15]. Under impulse condition, the dielectric or shunt losses of the reactor are more dominant than the series losses; therefore, the latter can be adequately represented by the ohmic losses of winding only [5.15].

The winding losses vary as square of the r.m.s. current in the winding and directly proportional with the resistance of the winding. Assuming that the current remains constant at a dominant frequency, the series resistance of the winding can be estimated using Equation (5.7):

$$R_{wk} = \frac{2N_k \rho_{al} r_c}{r_w^2} \tag{5.7}$$

where

R_{wk} winding resistance of section k (Ω)

N_k number of turns of section k

ρ_{al} conductor resistivity (Ω-m)

r_c coil radius (m)

r_w conductor radius (m)

5.4.3 Computation of the Dielectric Resistance for the Inter-turn Insulation

When a sufficiently high voltage is applied to a dielectric between two electrodes, a current flow consisting of three main components will be observed [5.20]. The first component is the charging or capacitive current that represents the fast response associated with a change in the electric field amplitude [5.20]. The second component is known as the absorption current, and is related to the polarization effect experienced by the molecules of the dielectric due to the applied voltage stress [5.20]. The third component is the conduction or leakage current, which is the actual electron current flow that passes through the insulation [5.20].

Leakage current represents the steady state of the dielectric current that relies upon the applied electric field and temperature. In practice, no insulation is perfect; therefore, even new insulation will have some leakage current, albeit small. The total

dielectric loss for solid insulating materials can be adequately represented as the loss in an additional resistance connection between the two electrodes [5.18]. It follows that the dielectric losses can be modelled either as a small resistance in series with an ideal capacitor or as the large resistance in parallel with an ideal capacitor [5.18]. In this thesis, the resistance representing the dielectric losses of the inter-turn winding insulation, R_{pk} is estimated using the following equation:

$$R_{pk} = \frac{(N_k - 1)\rho_m t_m}{\pi^2 r_c r_w} \tag{5.8}$$

where

R_{pk} shunt resistance of a section (Ω)

ρ_m resistivity of insulating material, Mylar (Ωm)

t_m thickness of insulating material (m)

In the calculation, the resistance R_{pk} is computed along the length defined by the thickness of the inter-turn insulation. The effective area is taken as half of the area of the conductor surface of the inter-turn winding. The equivalent resistance of a section is obtained by multiplying the resistance R_{pk} with N_k-*1*.

In work presented by Dahab [5.15], the shunt resistance representing the inter-turn dielectric losses is computed using a dissipation factor (tanδ) of Mylar, for which the value is stated at a dominant frequency of 1 MHz. The formula used is provided by Equation (5.9):

$$R_{pk} = \frac{N_k}{2\pi f C_{tt} \tan\delta} \tag{5.9}$$

where

R_{pk} shunt resistance of a section (Ω)

$tan\delta$ dissipation factor for Mylar = 0.016 at 1 MHz

C_{tt} turn-to-turn capacitance (F)

f dominant frequency (Hz)

In this thesis, both Equations (5.8) and (5.9) are used for the calculation of the shunt resistances. The calculated resistances obtained from these equations are presented in Table 5.2.

5.4.4 Computation of the Inter-turn Capacitances

The shunt capacitance is the capacitance-to-ground of the winding turns, which represents the electrical field between windings and the ground plane. The series capacitance is the capacitance between different turns in a winding section, which influences the electrostatic voltage distribution along the winding axial length. In this thesis, the series (C_{tk}) and the shunt capacitances (C_{gk}) are estimated analytically based on a well known parallel-plate principle.

Assuming a small thickness of the insulation coatings, it is possible to approximate the capacitance of the cylindrical shell, as in the case of an air-core reactor, with the capacitance of a parallel-plate capacitor. The following equation is derived for the calculation of inter-turn capacitance:

$$C_{tk} = \frac{\left(2\pi^2 \varepsilon_o \varepsilon_m r_c r_w\right) / t_m}{N_k - 1} \tag{5.10}$$

where

C_{tk} inter-turn capacitance of section k (F)

ε_o permittivity of vacuum (F/m)

ε_m relative permittivity of dielectric Mylar (F/m)

In deriving Equation (5.10), the effective area of the plate is taken as the surface area of half of the conductor surface facing the other winding conductor surface over the turn length of the winding conductor. For each of the winding sections, there are *N-1* elements of the turn-to-turn capacitance. Hence, the inter-turn capacitance of one section is obtained by first computing the capacitance turn-by-turn, and the values are lumped according to each section size. The total turn-to-turn capacitance of one section is obtained by taking the equivalent capacitance of a series connected turn-to-turn capacitances of that section.

Table 5.2 presents the inter-turn capacitance (C_{tk}), the series resistance (R_{wk}), and the dielectric resistance (R_{pk}) calculated for one winding section. All of these values are the same for all winding sections (refer Figure 5.2), given their similarity in construction.

Table 5.2: Computation of the inter-turn capacitance, the series resistance, and the dielectric resistance of a winding section

Inter-turn Capacitance (C_{tk})	Series Resistance (R_{wk})	Dielectric Resistance (R_{pk}) eqn.(5.8)	Dielectric Resistance (R_{pk}) eqn.(5.9)
19.159 pF	3.069 Ω	1.386×10^{16} Ω	5.192×10^{5} Ω

5.4.5 Computation of the Capacitance-to-ground

The calculation of the stray capacitances-to-ground of the reactor winding is performed according to the physical configuration described in Figure 5.1. As can be seen, each section is placed at a different height from the ground; hence, the winding capacitance-to-ground varies along its length. To calculate this capacitance, the following formula is derived,

$$C_{gk} = \frac{2\pi\varepsilon_o\varepsilon_a r_c b_k}{h_k} \tag{5.11}$$

where

C_{gk} capacitance-to-ground of section k (F)

ε_a relative permittivity of air (F/m)

b_k length of section k (m)

h_k distance from the centre of section k to the ground (m)

The capacitance-to-ground given by Equation (5.11) is obtained by considering the effective area as the product of the section circumference and height. The section circumference is equal to the perimeter of the cylinder with radius r_c, and the value is identical for all sections. For a vertically-mounted reactor, the height h_k is not constant, but it is a function of the location of a section measured from the ground plane to the centre of that section. The calculated capacitances-to-ground using Equation (5.11) are given in Table 5.3. As expected, the value is larger for sections closer to the ground, and decreases as height increases.

Another calculation method of the capacitances-to-ground proposed by Maruvada, et al. [5.20] was also investigated in this thesis. In the study, their proposed calculation procedures of capacitances-to-ground were thoroughly applied for a number of electrode configurations namely: spheres, horizontal and vertical toroids, horizontal and vertical cylinders, circular discs, horizontal and vertical plates, and a rectangular box. Derivations of analytical equations of the capacitance-to-ground are explained briefly for all electrodes. All electrodes considered in the computation are characterised by four main dimensions [5.20]:

- horizontal length of the object

- horizontal width of the object
- height of the object
- smallest distance between the object and ground

In a particular vertical cylinder configuration, the horizontal length of the cylinder is the same as its horizontal width, and the value is given by the diameter of the cylinder [5.20]. The capacitance-to-ground of any object is regarded as being composed of two capacitance values, as follows:

$$C_{gc} = C_{ge} + C_{gp} \tag{5.12}$$

where

C_{gc} capacitance-to-ground of a vertical cylinder

C_{ge} capacitance of the object well above ground

C_{gp} additional capacitance due to the proximity of ground

In this thesis, however, the influence of capacitance (C_{ge}) in Equation (5.12) is omitted; thus, the value of that capacitance was not calculated. The reason for this omission is because the reactor used in this work is assumed to be subdivided into a number of short sections that are placed very closely to each other and to the ground plane. Therefore, only additional capacitance due to the proximity of ground (C_{gp}) is considered, when the capacitances-to-ground of the reactor were calculated according to Maruvada, et al. [5.20].

In order to fully understand the derivations involved, the equation for calculating the capacitance (C_{gp}) of a vertical cylinder, as proposed by Maruvada, et al. [5.20] is re-calculated. The capacitance C_{gp} is derived based on Equation (5.13) below:

$$C_{gp} = \varepsilon_o \int_s \frac{dA}{h_k} \tag{5.13}$$

where:

dA elementary surface area (m^2)

h_k height above ground (m)

ε_o permittivity of vacuum (F/m)

The integration in Equation (5.13) is carried over the part of surface facing the ground plane. Furthermore, the calculation is made by taking into consideration the surface areas of the bottom, as well as the side of a vertical cylinder. This is given as:

$$C_{gp} = \varepsilon_o \int_s \frac{dA_{bottom}}{h_k} + \varepsilon_o \int_s \frac{dA_{side}}{h_k} \tag{5.14}$$

where, dA_{side} is the side elementary surface area of the side, and dA_{bottom} is the bottom elementary surface area of a cylinder. By applying this equation to a vertical cylinder, the following equation is derived:

$$C_{gp} = \pi \varepsilon_o d_c \left[\frac{d_c}{4h_k} + \ln\left(1 + \frac{b_k}{h_k}\right) \right] \tag{5.15}$$

Equation (5.15) obtained above is similar to the one provided by Maruvada, et al. [5.20]. It should be emphasised that here Equation (5.15) is derived by considering the surface area of the bottom cylinder to be equivalent to the surface area of a sphere. However, this is not applicable to a hollow cylinder representing the air-core reactor used in this work. Therefore, Equation (5.15) is modified to account for a hollow vertical cylinder configuration. Accordingly, the surface area of the bottom cylinder is re-calculated, and a new equation is derived as:

$$C_{gp} = \pi \varepsilon_o d_c \left[\frac{\pi d_c}{2h_k} + \ln\left(1 + \frac{b_k}{h_k}\right) \right] \tag{5.16}$$

Equation (5.16) is used to compute the capacitance-to-ground of the reactor windings shown in Figure 5.2, where d_c is the diameter of the winding conductor. For comparison, the calculated capacitances-to-ground obtained from Equations (5.11) and (5.16) are shown in Table 5.3. Based on these results, discrepancies of less than 10% are obtained between the capacitances-to-ground calculated from the two capacitance formulae. A fairly large difference was noticed only in the capacitance of the lowest section, which has the shortest distance to the ground plane.

Table 5.3: Computation of capacitances-to-ground based on two different formulae

	Equation (5.11)-pF	Equation (5.16)-pF	Difference (%)
$\mathbf{Cg_1}$	2.516	2.426	3.6
$\mathbf{Cg_2}$	2.796	2.683	4.0
$\mathbf{Cg_3}$	3.146	3.000	4.6
$\mathbf{Cg_4}$	3.597	3.403	5.4
$\mathbf{Cg_5}$	4.199	3.931	6.4
$\mathbf{Cg_6}$	5.042	4.653	7.7
$\mathbf{Cg_7}$	6.309	5.701	9.6
$\mathbf{Cg_8}$	8.427	7.363	12.6
$\mathbf{Cg_9}$	12.684	10.413	17.9
$\mathbf{Cg_{10}}$	25.637	17.964	29.9

5.5 Evaluation of an Air-core Reactor Detailed Model in ATP/EMTP Program

Dry-type air-core reactors intended for high voltage applications are designed with essentially zero radial voltage stress and with uniformly-graded axial voltage distribution between terminals [5.21]. Components discussed in the previous section; inductances, resistances, and capacitances determine the response of the reactor model to a switching transient stimulus. To obtain this, the ATP/EMTP program has been employed to simulate the MSCDN network during routine energisation. Figure 5.4 shows a full ATP/EMTP simulation circuit with a detailed model of the reactor added to the MSCDN network.

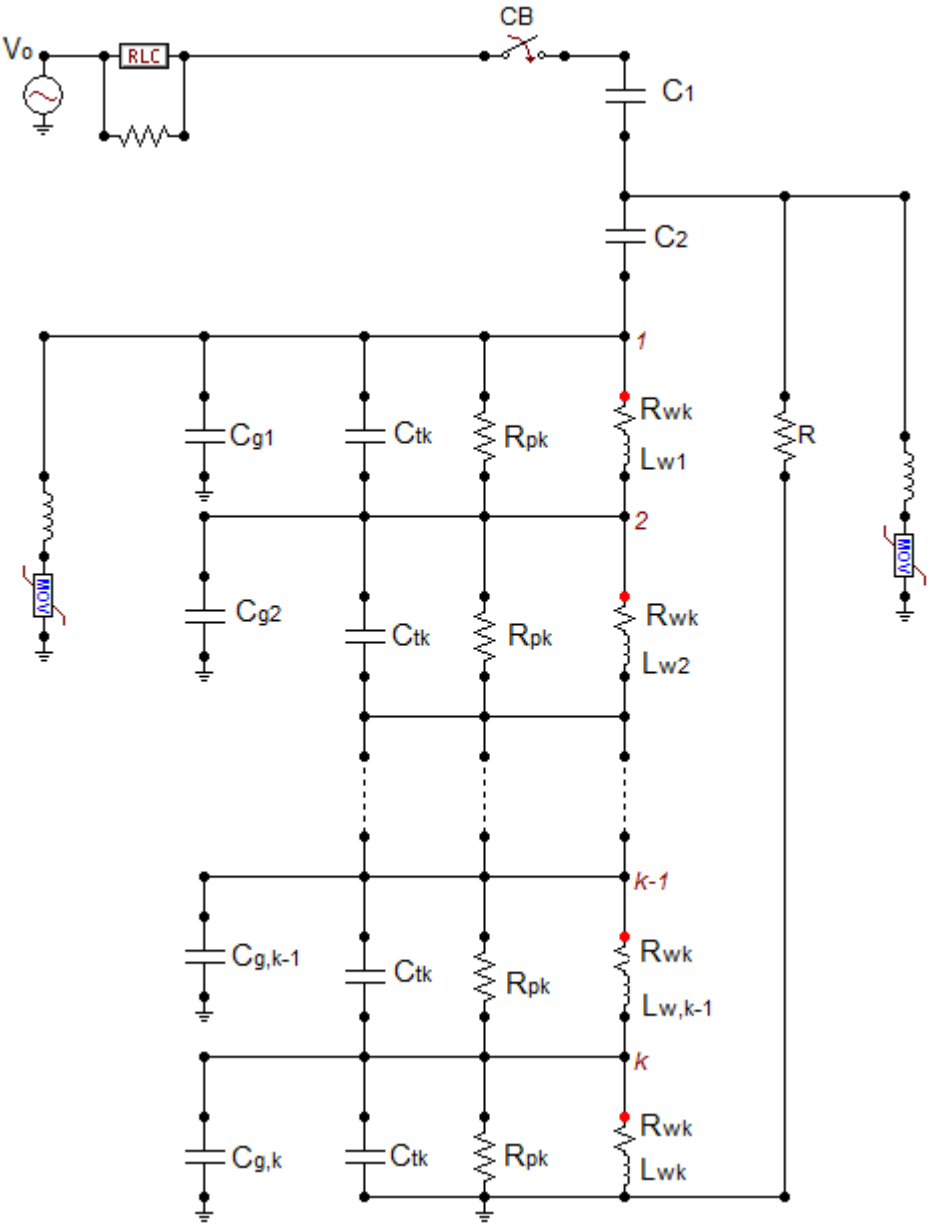

Figure 5.4: ATP/EMTP simulation circuit for the MSCDN

5.5.1 Simulation Procedures

To investigate surge voltage distribution, the circuit breaker is specified to close at the instant of voltage maximum, replicating worst switching conditions. All components of the simulation circuit are modelled in the same way as described in

Chapter 4. In the simulation, the time step of the ATP/EMTP program is specified as 10 ns, and the simulations are performed for a total time of 10 ms. The closing time of the switch representing the circuit breaker is specified at 2 ms, which has been adjusted correspondingly to the time of maximum supply voltage. Following the closing of the switch, the voltages to ground of various nodes on the reactor winding were obtained directly from the ATP/EMTP simulation outputs. In addition, the voltages across the sections of the reactor windings, as well as the currents of each component are also computed.

5.5.2 Distribution of Node to ground Voltage

The voltage-to-ground magnitude gives information on what possible maximum voltage amplitude could be generated during MSCDN energisation. For the windings, however, not only the magnitude of the voltage variation but also the rate of voltage changes determines the severity of the transient stress. Furthermore, the capacitive current of the dielectric is another important parameter in assessing insulation stresses generated by energising transients [5.22]. All of this information can be determined from the inter-turn voltage of the windings.

Figure 5.5 shows the voltage-to-ground computed at five different locations on the reactor winding. The voltage waveform V_{sec1} is the voltage-to-ground measured at the reactor terminal, which reaches the highest magnitude of approximately 225 kV. The actual steady state reactor voltage is approximately 50 kV. The waveform V_{sec2} gives the voltage-to-ground measured at 10% of the winding length. Similarly, V_{sec3} to V_{sec5} represent the node voltages occurring at 30% to 50% of the reactor winding, and so on.

The voltage to ground distribution throughout the winding at various times after the switching is presented in Figure 5.6. As can be seen from this figure, at the beginning of the impulse, the highest stresses were observed at the top of the winding. As the impulse propagates along the winding, the stress is redistributed towards the middle of the coil and away from the top. The results also show that the highest voltage at the reactor was occurred at the instant 5 ns following the MSCDN energisation.

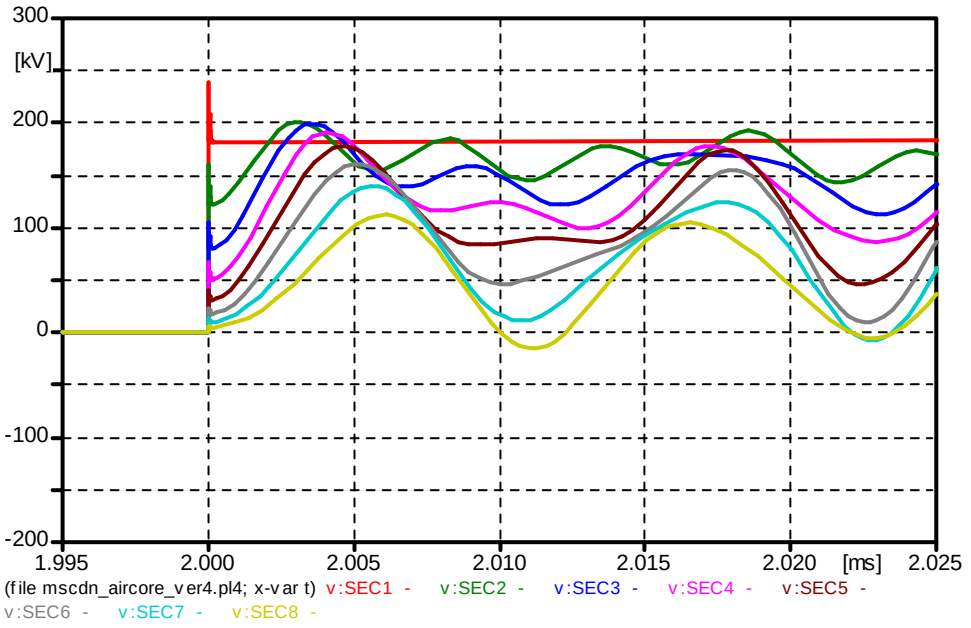

Figure 5.5: Node voltage to ground (V_{sec1} to V_{sec8} indicate the computed voltages at the 0%, 10%, 20% up to 70% along the winding away from the top HV terminal)

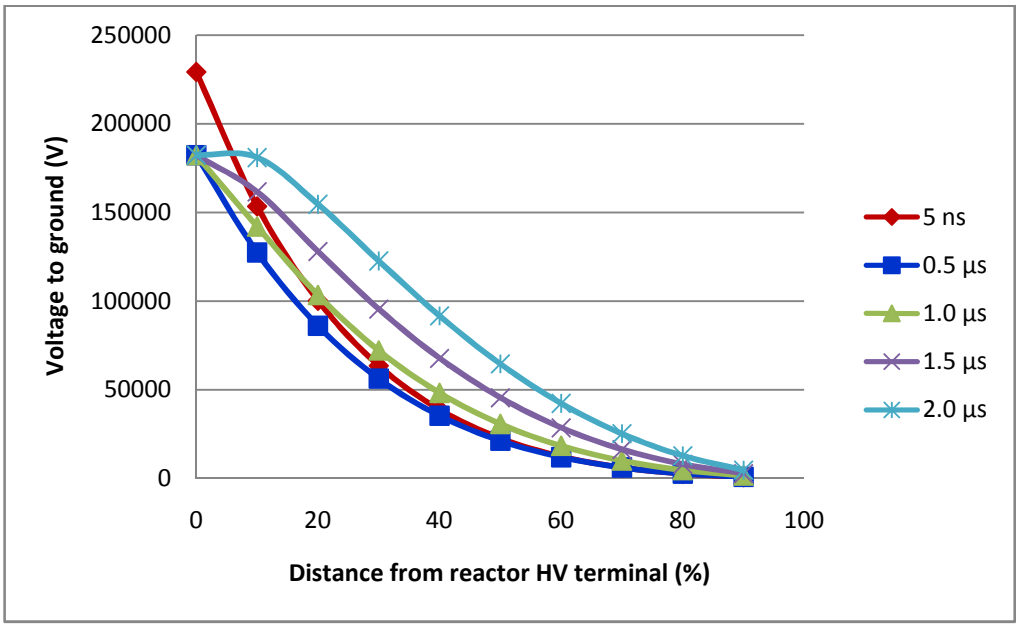

Figure 5.6: Distribution of node to ground voltages at different times following energisation of the MSCDN

A detailed equivalent circuit of air-core reactor obtained using a lumped parameter approach has been successfully simulated to establish the voltage distribution as shown in Figure 5.6. As can be seen, the voltage distribution along the reactor winding is not uniform because of the effect of stray capacitances to both inter-turn and ground couplings. This non-uniformity should be kept to a minimum to avoid damage to upper parts of the reactor winding, which are inevitable more stressed. Comparing the voltage distribution obtained in Figure 5.6 with the calculated and measured voltage profiles of air-core reactors published by Salama [5.13] and Dahab, et.al. [5.15] provides a further check of the validity of the computed equivalent circuit.

5.5.3 Distribution of Node-to-node Voltage

In addition to the voltage to ground, it is also very important to evaluate the voltages that appear within and across the sections of the reactor winding. Such voltages give

information about the stresses applied to the inter-turn winding insulation, as a result of the switching operation. The voltage differences between part-winding sections are presented in Figure 5.7. These voltages are labeled as V_{sec1}-V_{sec2}, V_{sec2}-V_{sec3}, V_{sec3}-V_{sec4}, V_{sec4}-V_{sec5}, and V_{sec5}-V_{sec6}, which correspond respectively to the voltages across the first five winding sections of the circuit shown in Figure 5.4 (i.e. section 1, section 2, up to section 5).

Furthermore, the distribution of maximum voltages appearing across each of all ten sections in the model is shown in Figure 5.8. In this computation, the maximum values of the voltages across sections are calculated, and as can be seen from Figure 5.8, the highest magnitude is found across the first section at the top of the reactor winding.

In addition, Figure 5.9 shows the voltage developed across the top 10%, 20%, and 50% sections of the winding length, starting from the top high-voltage terminal of the reactor. These are labeled as V_{sec1}-V_{sec2}, V_{sec1}-V_{sec3}, and V_{sec1}-V_{sec6} respectively. With reference to Figure 5.7, Figure 5.8, and Figure 5.9, the inter-section voltage V_{sec1}-V_{sec2} indicates that a magnitude of approximately 80 kV is imposed across the first section measured from the HV reactor terminal. Most importantly, this voltage is applied across a fraction of winding that stretches out to only one-tenth of the total length. This significant change in voltage magnitude along a small distance produces a strong electric field, resulting in high stress on the turn-to-turn insulation.

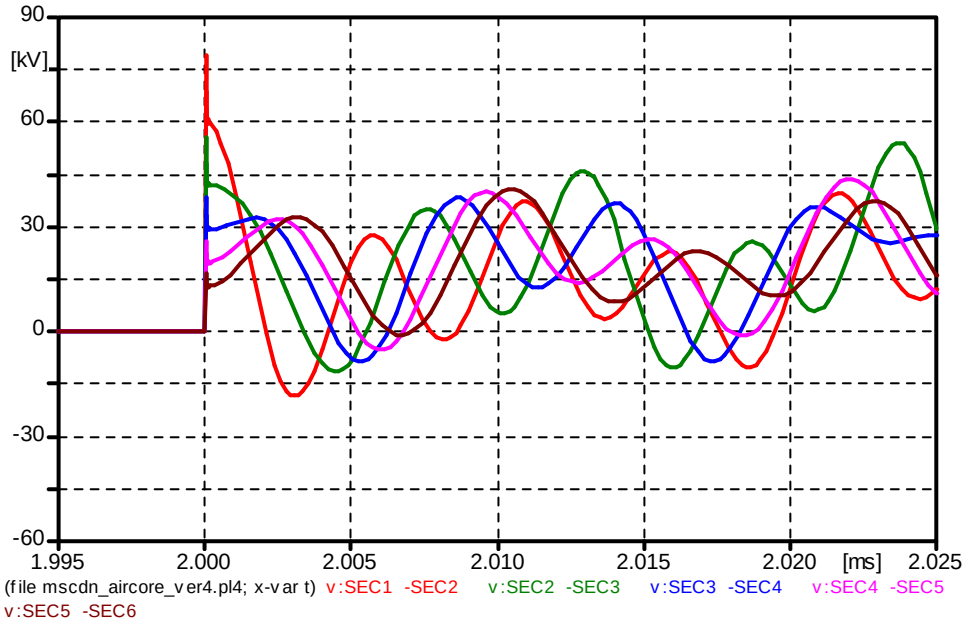

Figure 5.7: Voltage differences between part-winding sections along the reactor length

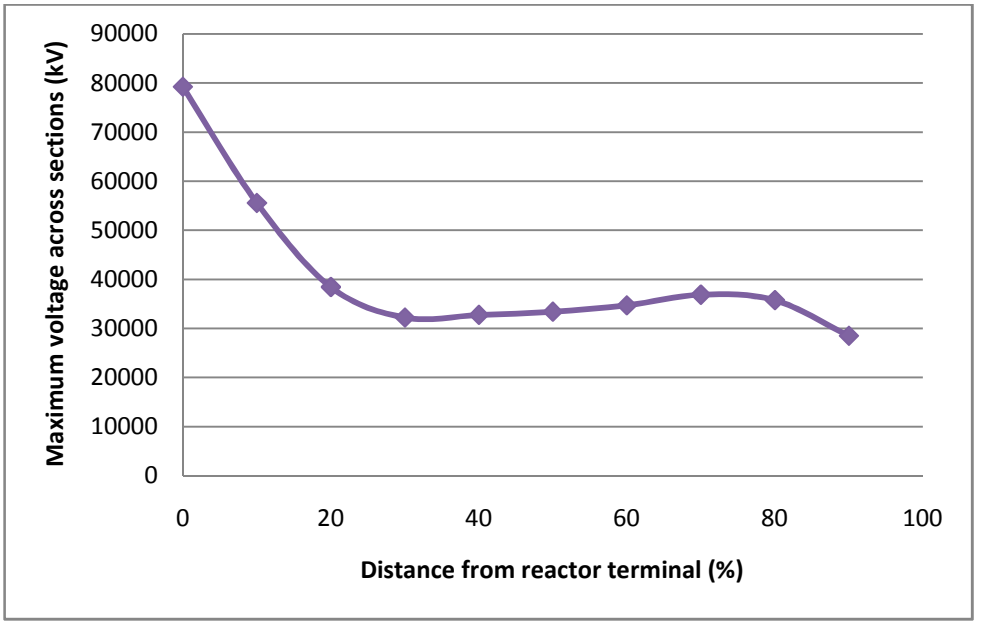

Figure 5.8: Distribution of maximum section voltages following energisation of the MSCDN.

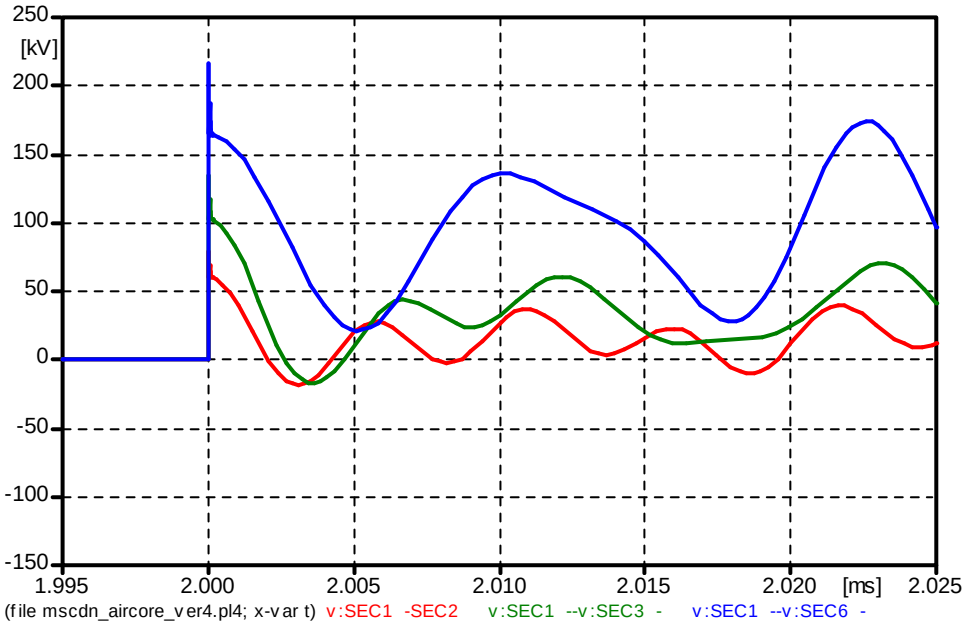

Figure 5.9: Section voltages (V_{sec1}-V_{sec2}, V_{sec1}-V_{sec3},and V_{sec1}-V_{sec6} correspond respectively to first 10%, 20%, and 50% of winding starting from the top)

5.5.4 Capacitive and Inductive Currents

Figure 5.10 presents the current flow through the reactor winding (I_L) and the current through the winding insulation (I_C) after the energisation of MSCDN. The current, I_C is the capacitive current flow through the stray inter-turn capacitances of the reactor winding. The magnitude of this current is merely dependent on the switching instant of the closing circuit breaker and the size of the voltage change at the reactor terminal.

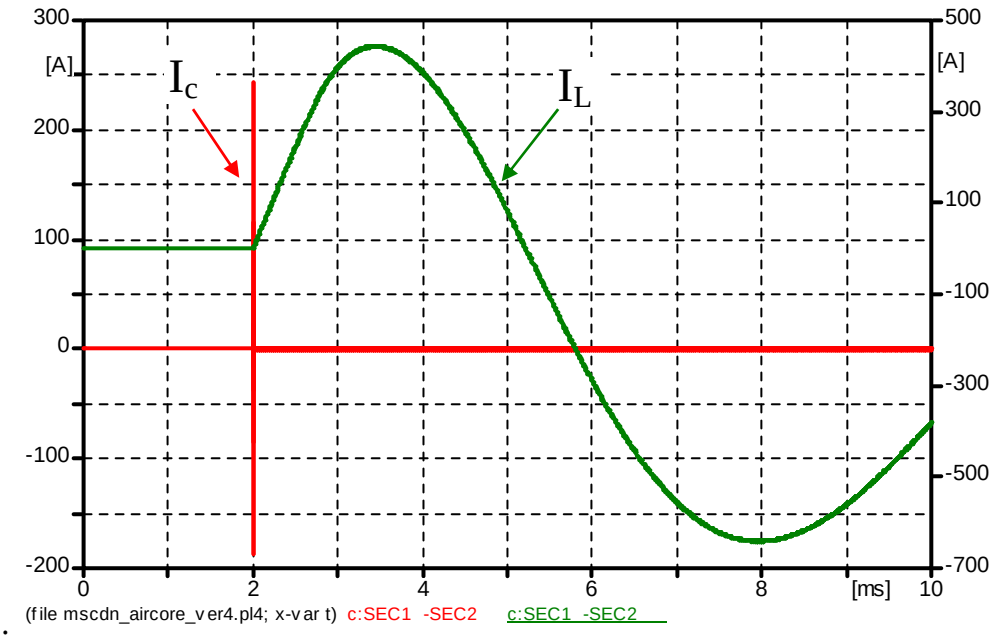

Figure 5.10: Capacitive current, I_C (left scale) through the inter-turn capacitance and current in the reactor winding I_L (right scale)

Figure 5.11 presents the current response on expanded time-scale. As can be seen, the capacitive current spike, which attained its highest value in a very short period of time, is clearly noticeable. The capacitive current reaches a magnitude of more than 200 A in just a few microseconds following energisation, during which time the circuit's current through the reactor winding is almost negligible. The main outcome of this high initial inter-turn capacitive current is the degradation that it can cause to the insulation, leading to weak points in the insulation. These may then be further damaged through thermal effects on application of main voltage during in-service duties. It is proposed that such mechanism is contributing to the failures experienced in service.

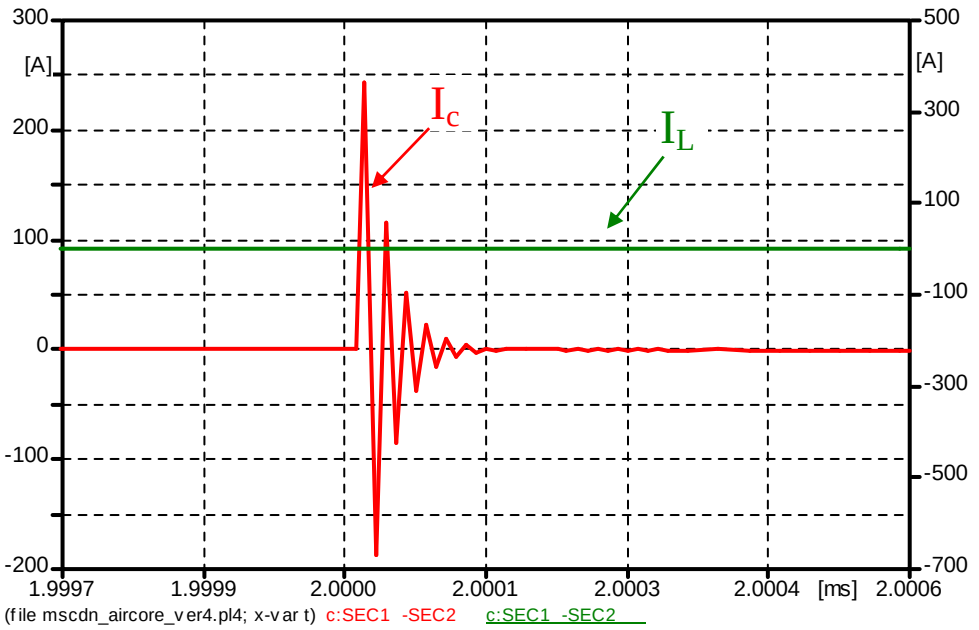

Figure 5.11: Close-up capacitive current, I_C (left scale) and current in the reactor winding, I_L (right scale)

5.6 Conclusion

It is generally known that very fast transient overvoltages are not dangerous because of their amplitude, but also because of their rate of rise. When the reactor insulation is frequently exposed to fast switching surges such as during MSCDN energisation, it deteriorates and finally can fail. This chapter proposed a new detailed model of a vertically-mounted single-layer air-core reactor using a lumped parameter model approach. The advantage of the lumped parameter model is that it can be easily implemented in simulation software. All important winding parameters were considered in developing the model and the derivation of their values was performed using analytical equations. The evaluation of the derived reactor model was conducted by means of ATP/EMTP simulations, which demonstrated that following energisation, the voltages appearing across the reactor corresponded to fast-front overvoltages with significant rates of change. Finally, it was shown that by

subdividing the reactor height into a number of sections, the voltage distribution within the winding deviates excessively from linearity. It was shown that the top coil turns experience very high voltages compared with other parts of the reactor winding. This leads to excessive capacitive currents through the inter-turn insulation of the winding. From this result, it is proposed that degradation of the insulation may result from such spike of current and when followed by thermal effects due to steady state operation, failure of the reactor may occur. Detailed investigation of these stresses is presented in Chapter 6.

Chapter 6: Distribution of Electric Field Stress along MSCDN Air-core Reactors and Possible Failure Mechanisms

6.1 Introduction

Chapter 5 presented the derivation of a detailed air-core reactor model based on a lumped parameter approach. This chapter builds on that derivation by detailing the key implementation of the reactor model. The general degradation problems experienced by some of the reactors during field service are discussed and this is followed by derivations of new analytical equations for calculating the electric field strength on the reactor winding. This also includes an analytical computation of dielectric stress on the reactor winding insulation following MSCDN energisation. The effect of the fast voltage change at the reactor terminal on the dielectric current of its winding insulation is quantified. Furthermore, a parametric analysis conducted to evaluate the effect of reactor design parameters on the generated dielectric stress during switching. Finally, a proposal is made for a failure mechanism applicable to such reactor designs and which results from switching operations.

6.2 Failure of the Electrical Insulation

The health of electrical power devices, such as high voltage transformers, cables, reactors or capacitors usually depend on the operating state of its electrical insulation [6.1]. Generally, life expectancy of electrical insulation is about 40 years [6.2], so failure before the insulation reaches that age is considered unacceptable. In the worst case, failure of the insulation may be immediate, especially if the operating conditions are not within the specified margins. It is well known that voltage waveforms in power transmission systems cannot be considered to be sinusoidal at all times, due to the presence of harmonics [6.3]. In fact, even in a well-designed

system where the harmonic content is limited to about 2% of the rated frequency, the harmonic content may reach or occasionally exceed the 5% level [6.3]. As a result, additional phenomena are likely to occurs on the system, which may influence the energy withstand behavior of the dielectric, and possibly impair the system reliability [6.3].

In high-voltage system, insulation failures due to direct, alternating, and impulse high voltages are often related to electrostatic and electrical conduction fields [6.5]. For reactors, turn-to-turn insulation failure at the HV end of the reactor is the most common problem encountered during their service operation [6.6]. Such a failure may cause short circuit of turn-to-turn insulation, which consequently damages the reactor due to excessive overvoltages. Dielectric breakdown is one of the phenomena concerned with the failure of solid and liquid insulating materials used inside high-voltage equipment. This problem may occur if the applied electric field is high enough that it exceeds the dielectric strength of the insulation [6.7-6.10]. Factors that influence the dielectric strength include the magnitude, shape, duration and polarity of the applied voltage, the operating temperature, and other physical states of the insulation [6.11]. For solid dielectric materials, destructive stresses in electrical insulation systems are usually caused by one or any combination of electrical, mechanical, thermal, and environmental factors [6.11]. In this thesis, only the effect of electrical stresses on the air-core reactors is considered.

6.3 Analytical Calculation of the Electric Field Strength in the Inter-turn Insulation of the Reactor Winding.

As explained in the detailed MSCDN simulation presented in Chapter 5, the highest overvoltage is found to occur at the top 10% of the reactor winding length. In this

chapter, the results obtained are used to study the influence of such non-uniform voltage distribution on the electrical field characteristics at the winding insulation. This section describes the derivations of analytical equations for calculating the electric field strength at the identified worst stressed locations. In addition, proposals for optimum designs of the reactor are briefly discussed in this chapter. The derivation of the electric field strength is performed based on procedures described in the flowchart in Figure 6.1.

6.3.1 Estimation of the Thickness of Insulation

The critical field intensity or dielectric strength is the point at which a certain insulator loses its insulating property and is subjected to an electrical breakdown [6.6, 6.12]. In the case of a uniform electric field, this value can be determined from the ratio of the breakdown voltage to the distance of the electrodes [6.12]. The following analysis seeks to establish the thickness of insulating materials surrounding the winding layers at a particular location along the winding surface. In this analysis, it was assumed that the thickness of insulation in one turn layer (insulation between two successive turns of the winding) is equal to twice the thickness of the insulating material surrounding the conductor of the winding, and is referred to as $2t_m$.

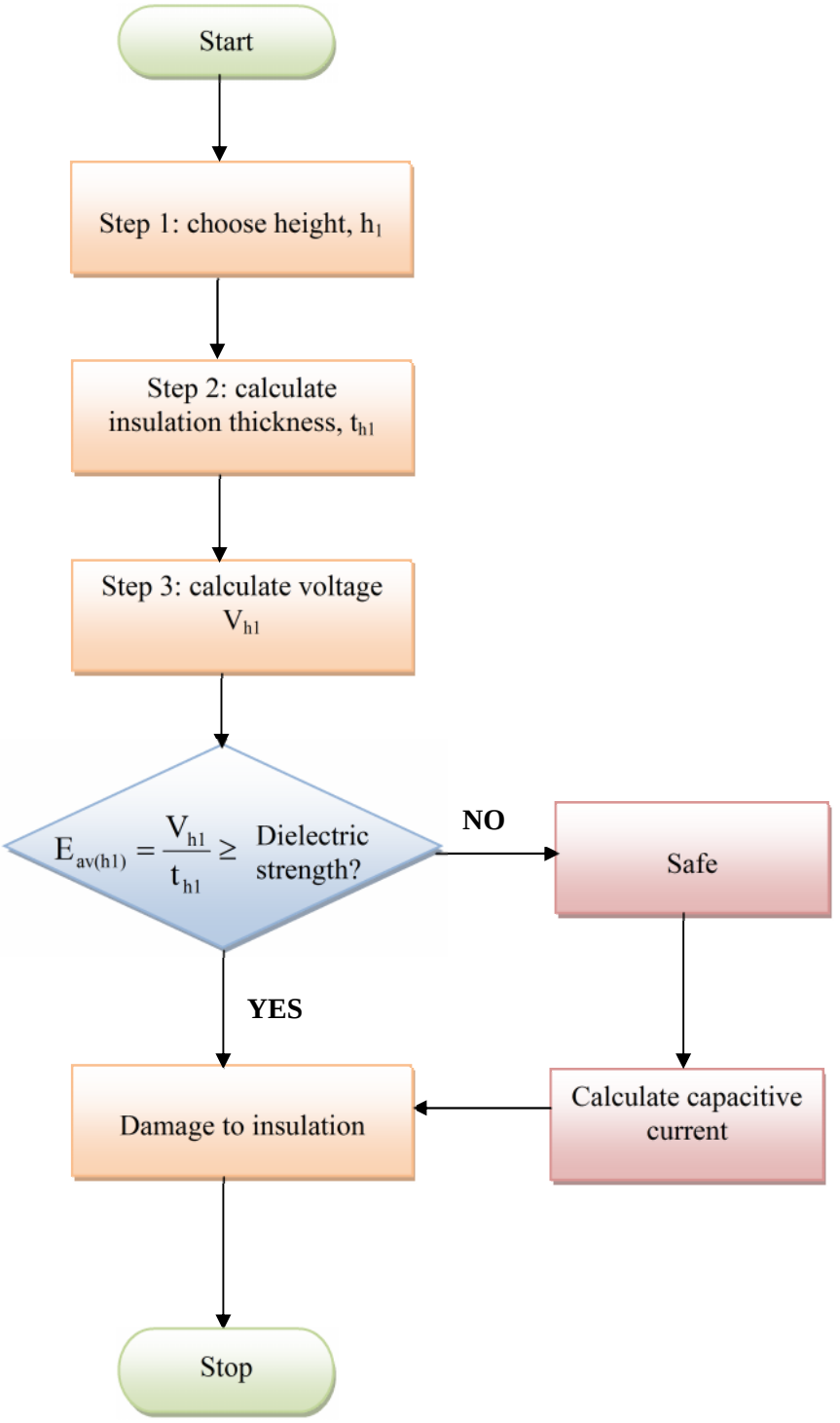

Figure 6.1: Flowchart of electric field strength calculation procedures

For a coil having *N* turns of conductors, the total insulation thickness in the coil is obtained by multiplying the number of turns with $2t_m$. This can be expressed as:

$$t_h = N \times 2t_m \tag{6.1}$$

Equation (6.1) can be further expanded to obtain the relationship between the coil height and the thickness of insulating material. In this case, the height of a coil can be obtained by the sum of the insulation thickness in a layer and the size of the winding conductor. This relationship can be written as:

$$h_x = N(2t_m + 2r_w) \tag{6.2}$$

By rearranging and simplifying Equations (6.1) and (6.2), a new expression is obtained that provides the total insulation thickness as a function of the conductor radius and the insulating material thickness:

$$t_h = \frac{h_x}{1 + \left({}^{r_w}/_{t_m}\right)} \tag{6.3}$$

where,

h_x the height of any locations from the HV terminal end (cm)

t_h total insulation thickness (cm)

r_w the conductor radius (cm)

t_m thickness of insulating material (cm)

6.3.2 Determination of the Inter-turn Voltage Distribution

The computation of the potential difference and resulting electric field between the winding turns is quantified using the winding geometry and the computed voltage obtained in Chapter 5. With reference to Figure 5.6 of Chapter 5, the highest voltage magnitude due to MSCDN energisation was occurred at time interval 5 ns. In this

chapter, the normalised values of the voltage distribution shown in Figure 5.6 are calculated and presented as in Figure 6.2. For each time interval, the normalised value is obtained by dividing the voltages by the highest voltage magnitude of the time considered. Furthermore, the normalised voltage distribution obtained at 5 ns is used in the calculation of electric field strength on the reactor winding.

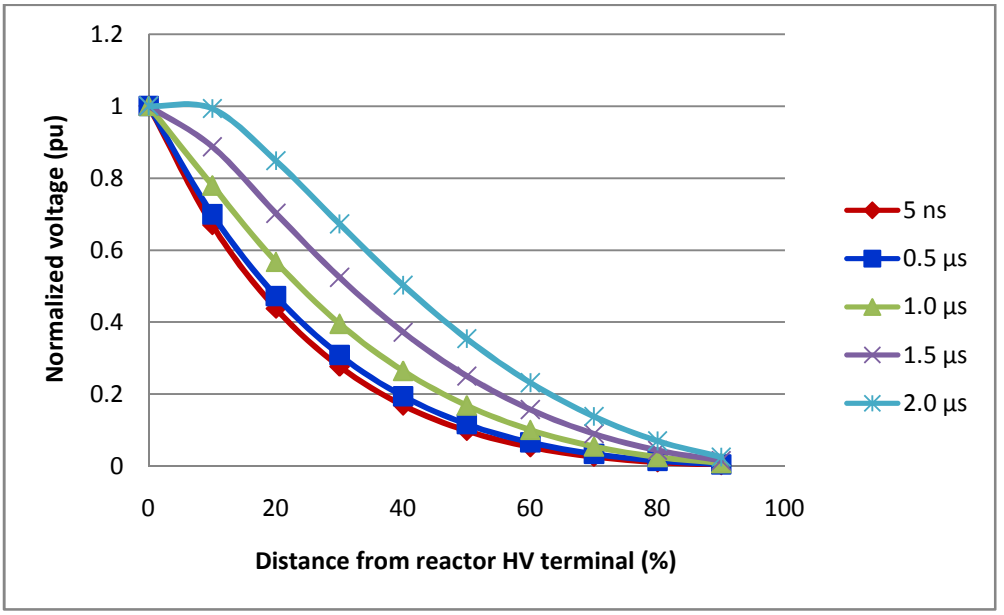

Figure 6.2: Normalised voltage distribution at different times following energisation of the MSCDN

In the following analysis, a simple derivation is performed to establish a relationship between the voltage and the winding length based on the voltage distribution obtained at time 5 ns, which is the assumed worst energising transient. It is assumed that an exponential function is the mathematical function that fits the computed voltage distribution more or less. With reference to Figure 6.2, a mathematical expression describing the voltage distribution at 5 ns is derived using an exponential function. A general exponential form is given as:

$$y = ce^{-bx} \tag{6.4}$$

where,

y normalized voltage (p.u)

x height of reactor (%)

b,c exponential coefficients

Equation (6.4) is elaborated to obtain other voltages along the reactor winding, whose values were not provided in Figure 6.2. It is particularly important to obtain the unknown voltages at the top 10% of the winding, which is the most stressed location during the energising operation. In order to identify these voltages, the coefficients *b* and *c* in Equation (6.4) are determined using the known voltages at points 0% and 10% respectively. Through simple mathematical manipulation, the following equation is obtained:

$$y = e^{-0.04013x} \tag{6.5}$$

Ultimately, Equation (6.5) can be used to estimate the voltage to ground (in p.u.) at any desired points on the reactor winding. However, this equation is derived to predict the voltages within the most affected winding locations, which is up to 10% of the total height measured from the HV terminal. Figure 6.3 shows the good fit obtained for the time 5 ns calculated using Equation (6.5) and the ATP/EMTP simulation. This allows confidence that Equation (6.5) can be used to obtain the voltage with sufficient accuracy, at least within the constituted parts of the winding.

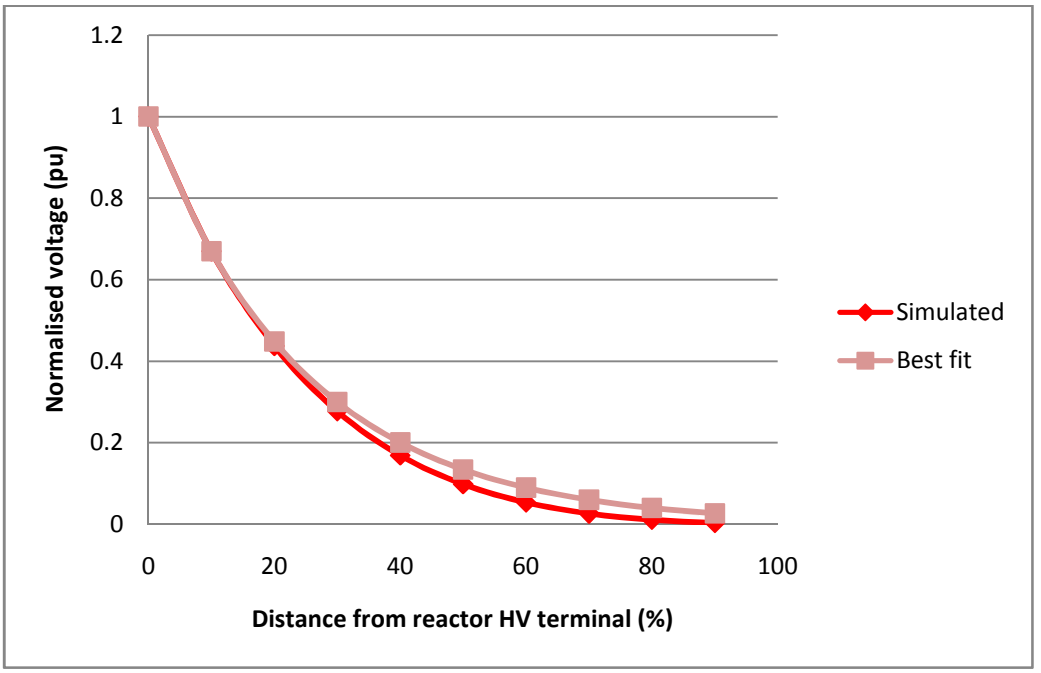

Figure 6.3: Normalised voltage distribution at time interval 5 ns obtained by ATP simulation and analytical calculation

In order to determine the electric field applied on the winding, a voltage difference appearing across two points on the winding location must be obtained. Expanding Equation (6.5) allows the calculation of the inter-turn voltage along the reactor winding. Assuming that the applied electric field is examined at a distance x% on the winding vertical length, the voltage difference at this particular location (V_h) with respect to the reactor HV end can be expressed as:

$$V_h = V_m(1 - e^{-0.04013x}) \tag{6.6}$$

where,

x distance x from the reactor terminal (%)

V_h potential difference at any location on the winding (V)

V_m maximum voltage occurred at time 5 ns (V)

6.3.3 Derivation of a Simplified Expression for Inter-turn Electric Field Strength

A few assumptions are made regarding the reactor winding geometry under calculation in order to calculate the electric field applied at the top 10% winding locations. First, it is assumed the electric field is constant at every point within the small winding areas. This means that the field intensity in the dielectric is uniform throughout the solid insulation between the two plates and that the potential varies linearly in the gap. This is true since the computation of the electric field was performed over a relatively small area that stretched about one-tenth of the total winding length. Thus, the electric field can be approximated by placing two conducting plates parallel to each other and maintaining a potential difference between them. This assumption is made in order to nullify the effect of field distortion at the edges of the plates, i.e. fringing effect of the line forces, thus simplifying the calculation procedures. Ignoring such effects, the equation for the magnitude of the average electric field strength, E_{av} is given as:

$$E_{av} = \frac{V_h}{t_h} \tag{6.7}$$

The voltage, V_h can be calculated using Equation (6.6) and the insulation thickness, t_h is provided by Equation (6.3) derived in the previous sections. In total, there are three steps involved in calculating the electric field strength using Equation (6.7). This computation can be further simplified if only one equation is involved to determine the electric field. Substituting Equations (6.3) and (6.6) into Equation (6.7), a new relationship between the electric field strength, the applied voltage, and the winding parameters is obtained as shown in Equation (6.8):

$$E_{av}(h_x) = \frac{V_m}{h_x}\left(1 + \frac{\mathrm{r_w}}{\mathrm{t_m}}\right)\left(1 - \mathrm{e}^{-\mathrm{bx}}\right) \quad (6.8)$$

where, $E_{av}(h_x)$ is the applied average electric field strength on location h_x measured from the HV terminal of the reactor. Equation (6.8) shows that for a particular voltage distribution, the calculated electric field strength is influenced by several parameters such as the maximum voltage (V_m), the distance from the reactor HV terminal (h_x), the thickness of insulating materials (t_m), and the size of the winding conductors (r_w). The physical geometry of the reactor winding, such as the diameter of the conductor and the insulation thickness are fixed parameters therefore, the average electric field only depends on the time at which the maximum overvoltage occurs and the location along the reactor winding.

6.3.4 Computation of Electric Field Strength in the Inter-turn Reactor Winding

The calculation of electric field strength using Equation (6.8) just derived is performed for five time intervals, and the calculated results obtained are shown in Figure 6.4. It the calculations, different equations of the average electric field were obtained, which dictated by the maximum overvoltage occurred in each respective time. Table 6.1 gives the values of V_m and b determined from the analysis carried out in Section 6.3.2. Using Equation (6.8) and the data in Table 6.1, the, the average electric field strength for five time intervals are obtained as shown in Table 6.2. Figure 6.4 shows the average field obtained for the upper 10% section of the winding length. The results indicate that the highest field of approximately 73 kV/cm was occurred at time 5 ns following the energisation. The calculated field obtained was computed based on an insulation thickness of 100 µm. This high magnitude of

electric field may have significant effect on the insulation after a large number of switching operation.

Table 6.1: The calculated values of constant b and V_m of Equation (6.8) for all time intervals considered

Time / Constant	5 ns	0.5 µs	1 µs	1.5 µs	2 µs
b	0.04	0.036	0.025	0.012	0.001
V_m (kV)	229.209	182.234	182.248	182.263	182.279

Table 6.2: Computation of electric field strength along the reactor winding at different time intervals following the switching

x (%)	h_x (cm)	t_h (cm)	E (kV/cm)				
			5 ns	0.5 µs	1.0 µs	1.5 µs	2.0 µs
0.08	0.212	0.010	72.706	51.865	35.892	17.308	1.443
1	2.65	0.126	71.381	51.016	35.484	17.212	1.442
2	5.3	0.252	69.977	50.114	35.048	17.110	1.442
3	7.95	0.379	68.610	49.233	34.619	17.008	1.441
4	10.6	0.505	67.279	48.373	34.196	16.907	1.440
5	13.25	0.631	65.982	47.533	33.781	16.807	1.440
6	15.9	0.757	64.719	46.713	33.373	16.707	1.439
7	18.55	0.883	63.489	45.912	32.971	16.609	1.438
8	21.2	1.010	62.290	45.129	32.575	16.511	1.437
9	23.85	1.136	61.122	44.365	32.187	16.414	1.437
10	26.5	1.262	59.984	43.618	31.804	16.317	1.436

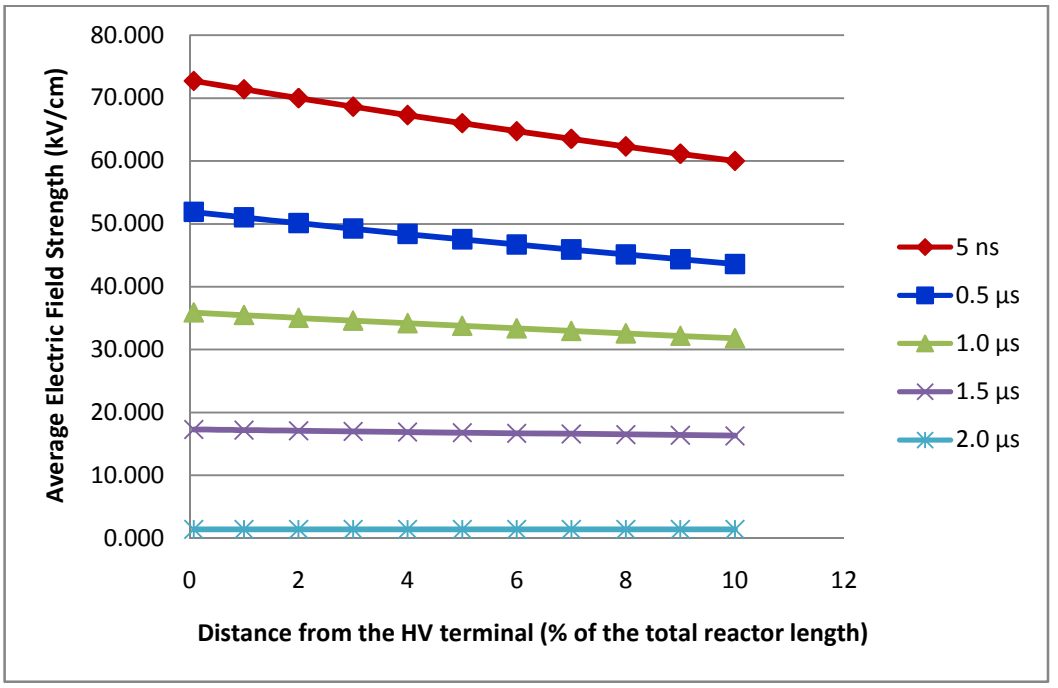

Figure 6.4: Average electric field strength on reactor winding at different times following MSCDN energisation

6.4 Estimation of Dielectric Current Flow in the Inter-turn Insulation

Degradation of electrical insulation may be incurred due to effects of temperature, applied electric field strength, and current flow through the insulation that usually emerges during transient events [6.4-6.5, 6.11, 6.13- 6.17]. The resistive or leakage current is the electron flow that passes through the insulation. For a good insulator, this current is small and constant, and could simply be due to the dielectric not being a perfect insulator, which has some non-zero conductivity [6.11]. The capacitive or displacement current represents the fast response associated with a change in the electric field amplitude [6.11]. The capacitive current of the inter-turn insulation can be expressed as:

$$i_{ct} = C_{tt}\left(\frac{dV_{tt}}{dt}\right) \tag{6.9}$$

where,

i_{ct} capacitive current of the insulation (A)

C_{tt} turn-to-turn capacitance (F)

V_{tt} turn-to-turn voltage (V)

dt voltage transition time (s)

Since the capacitive current is voltage-dependent, an abrupt change in the voltage may produce a short burst of capacitive current. In this present work, the effect of the capacitive part of the dielectric current is examined during the worst MSCDN energising case. With reference to Figure 6.4, it is shown that the transition time *dt* can be as fast as 5 ns when the MSCDN energisation takes place at unfavourable instants. The voltage difference *dV* across the inter-turn winding is estimated using Equation 6.6. Using this equation, the voltage difference of 0.735 kV was obtained for the top inter-turn winding (measured from the reactor HV terminal). Furthermore, referring to the computation performed in the Chapter 5, the inter-turn capacitance of the winding C_{tt} was obtained as 2.362 nF. Substituting these values into Equation (6.9), the capacitive current flowing through the turn-to-turn winding insulation is obtained as:

$$i_{ct} = C_{tt}\left(\frac{dV_{tt}}{dt}\right) = 347.21 \text{ A} \tag{6.10}$$

It was shown that high *dV/dt* results in a current surge of magnitude of nearly 350 A flowing through the reactor winding insulation and remains for the duration of the surge. In addition to this current is the steady-state current that flows during normal MSCDN operation. The combined effect of these currents could lead to excessive dielectric heating in the winding insulation. Furthermore, the occurrence of these currents is possible at every MSCDN energisation, which is performed several times

per day. Over time, degradation in the insulation system due to the cumulative effect of high dielectric current and applied electric field may be evident.

6.5 Effect of Air-core Reactor Parameters on Inter-turn Field and Current

To determine the influence of reactor winding parameters on the maximum values of the electric field strength, the base case result of electric field distribution is used as control case. A parametric analysis is conducted on the severely stressed areas using the circuit model developed in Chapter 5 as shown in Figure 5.4. Systematic variations of all important parameters shown in Table 5.2 and Table 5.3 of Chapter 5 are performed, in which only one of the parameters was varied within its specified low and high values. These calculated results are then compared with the base case.

6.5.1 Effect of Dielectric Resistances (insulation losses, R_{pk})

For the reactor winding, the damping of the surge is introduced by both the conductor and the dielectric losses. Based on the analysis conducted, it was observed that the time response of the reactor voltage is not sensitive to the series or winding conductor losses. This is mainly due to the large Q factors for the reactors, which results in time constants for the series branches that are much larger than the time periods considered in the transient analysis [6.18]. However, the reactor voltage was found to be more sensitive to the shunt or insulation losses [6.18].

The variations of the electric field strength across the upper 10% of the reactor considered for low and high shunt resistances are shown in Figure 6.5. As expected, a high value of dielectric resistance would reduce losses and allow high electric field magnitude to appear across the inter-turn insulation. If this resistance is lowered, significant losses will occur and lower fields will result. It is shown that the maximum voltage decreased by approximately 40% of the base case voltage for ten

order-of-magnitudes reduction in the shunt resistance. As a result, the maximum electric field strength applied on the winding insulation also decreased.

The shunt resistance, representing the losses between winding turns is dictated by a number of design factors such as type of dielectric material, insulation thickness, and the reactor diameter. Low shunt resistances represent the cases where insulating materials were used that have lower resistivity than Mylar polyester film. However, in real applications of the reactor, the dielectrics used for wrapping the winding conductors are usually made of high-quality materials, which result in substantially higher resistivity. Increasing the thickness of the insulation is another aspect of design that can also increase the shunt resistance.

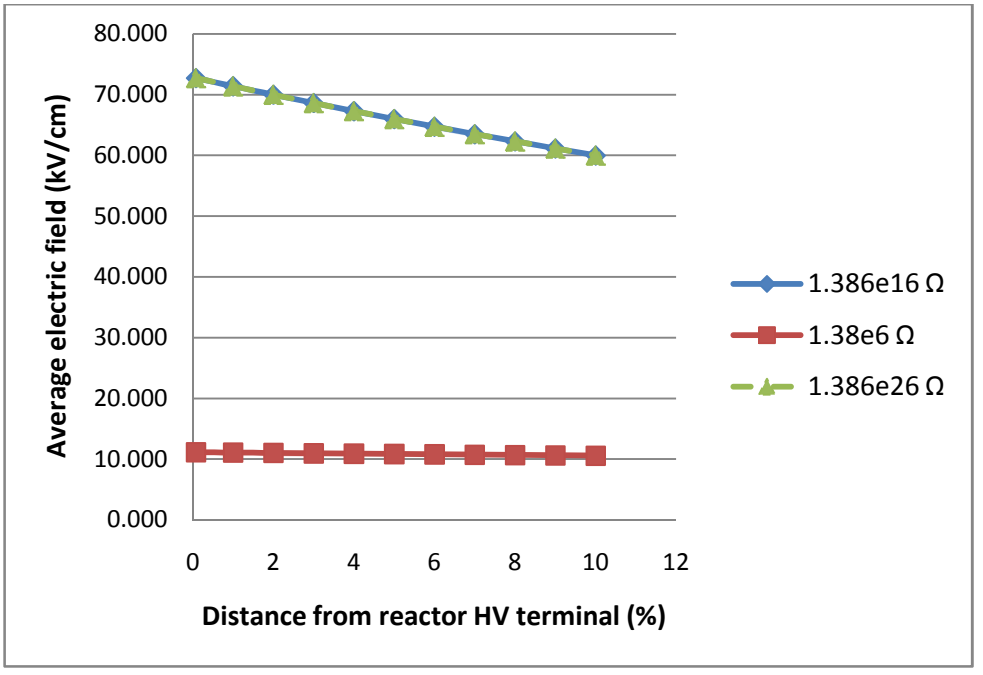

Figure 6.5: Effect of inter-turn insulation resistance on electric field

6.5.2 Effect of Winding Turn

Figure 6.6 shows the effect of winding inductance on the maximum electric field strength. In the computation, the effect of high inductance on the electric field strength was determined by increasing the inductance of each winding section by 50% of its base case value. Similarly, a reduction of the base case inductance by an equal percentage was done in order to determine the effect of low winding turn on the electric field strength. Based on the results shown in Figure 6.6, increasing and decreasing the inductance from the base case value has no significant effects on the maximum voltage generated. As can be seen from this figure, the calculated electric field strength remains the same as in the base case for increasing and decreasing values of the winding turn. This is expected because the magnetic field of the inductance requires a certain time to build up, whereas transient analysis conducted in this work lasted for a short duration of time. Usually, when the applied voltage is maintained for a sufficient time, appreciable currents begin to flow in the inductances, leading to nearly uniform voltage distribution [6.19].

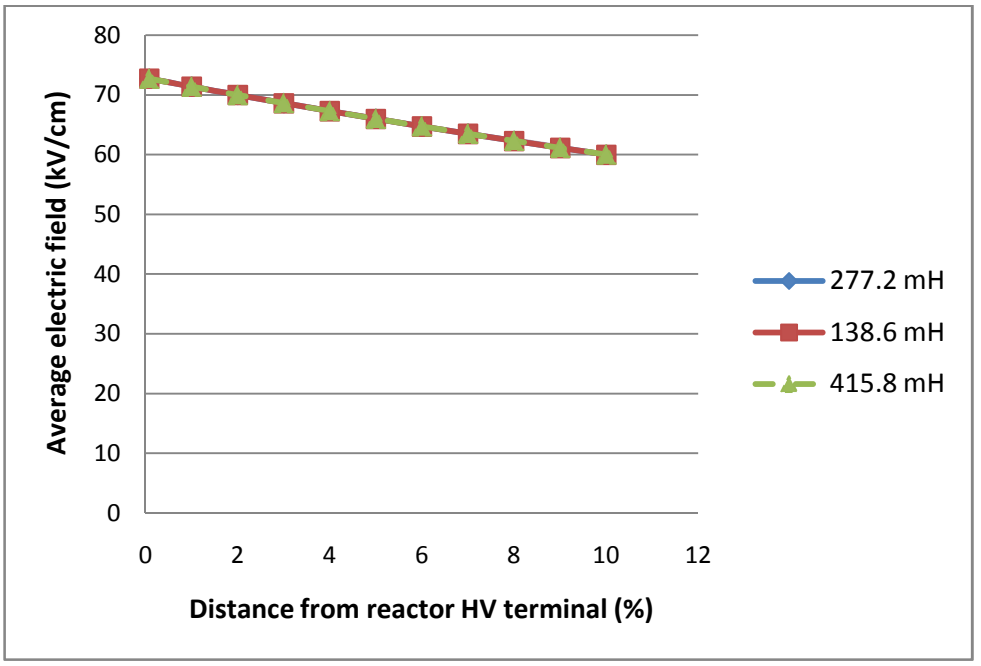

Figure 6.6: Effect of winding turn inductance on electric field

6.5.3 Effect of Inter-turn Capacitances on Electric Field

The effect of inter-turn capacitance on the electric field strength was considered for lower and higher inter-turn capacitances, relative to its base case value of approximately 19 pF (refer Table 5.3 in Chapter 5). Low and high inter-turn capacitances were obtained by reducing and increasing the base case value by one order of magnitude. Figure 6.7 presents the variation of the electric field strength across the upper 10% of the reactor winding considered for low and high inter-turn capacitances.

Based on the analysis conducted, as the inter-turn capacitance decreases, the voltage uniformity along the reactor winding is aggravated. For one order of magnitude decrease in the inter-turn capacitance, the voltage across the uppermost inter-turn winding was increased approximately 200% from its base case value. Since the electric field applied on the inter-turn winding insulation is directly related to the

voltage across it, the resultant electric field strength reached a highest magnitude of about 220 kV/cm. This calculated value exceeded the manufacturer-specified dielectric strength for Mylar polyester film of 170 kV/cm [6.25]. Furthermore, it was found that low inter-turn capacitance may reduce the capacitive current that is flowing through the inter-turn winding insulation. Using Equation (6.9), the capacitive dielectric current obtained in this case was approximately 260 A. This current is less than 350 A, which is the value calculated in the base case.

On the other hand, the voltage distribution on the upper 10% of the reactor winding is greatly improved for increasing inter-turn capacitance. In the computation, the inter-turn voltage decreases by approximately 60%, resulting solely from one order of magnitude increase in the inter-turn capacitance. As a result, the electric field strength was also reduced. This is somehow expected as increasing the inter-turn capacitance is one of the main strategies for improving the transient response of transformer windings [6.11, 6.18, 6.20]. For transformers, interleaving is the most commonly used but costly method of winding, which can increase the inter-turn capacitance to achieve a better voltage distribution.

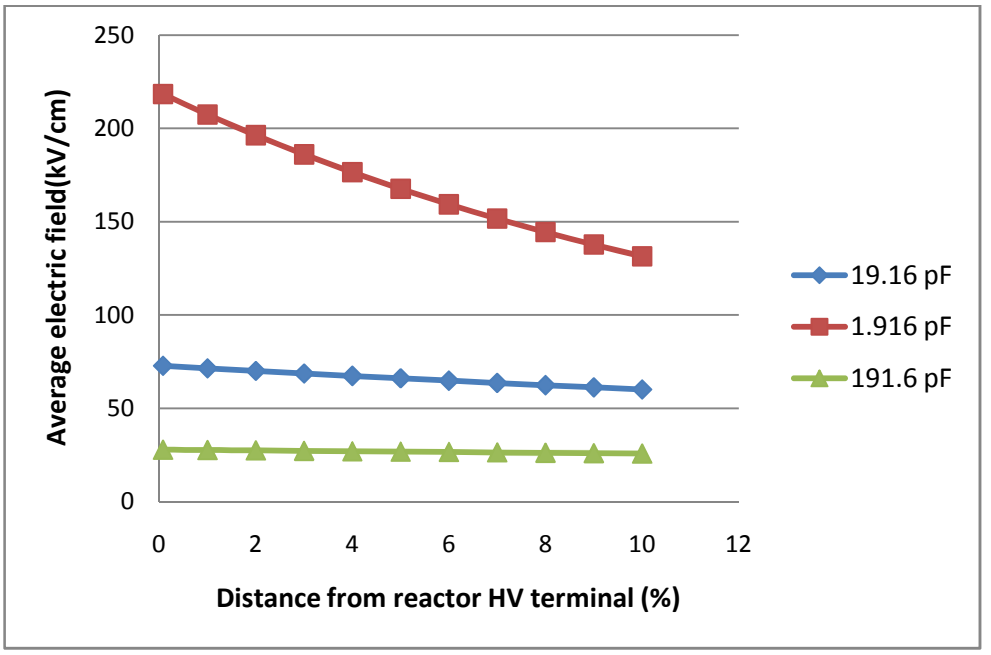

Figure 6.7: Effect of inter-turn capacitance on electric field.

6.5.4 Effect of Capacitance-to-ground on Electric Field

In order to determine the effect of capacitance-to-ground on the calculated average field strength, the corresponding capacitances of each winding section were decreased and increased respectively, by one order of magnitude from its base case value. Figure 6.8 shows the electric field strength distribution on the upper 10% of the reactor winding considered for low and high capacitances-to-ground. For high capacitance-to-ground, the calculated inter-turn voltage obtained was extremely high. As a result, the maximum electric field strength increases by approximately 180% from the base-case value. Furthermore, increasing capacitance-to-ground may also increase the capacitive dielectric current flow of the inter-turn insulation. In this case, the capacitive current obtained using Equation (6.9) was approximately 380 A. As reactor ratings get larger, there will be a tendency for the capacitance-to-ground to get smaller relative to the inter-turn capacitance, due to increase in physical size

and increased clearances. With reference to Figure 6.8, a decrease in the ground capacitance has little or no influence on the voltages and the calculated electric field strength. Based on this investigation, it is expected that if the ground capacitance is reduced, more current will flow through the inter-turn capacitances, which will lead to uniform voltage distribution along the winding, which agrees with the theories in [6.20, 6.21].

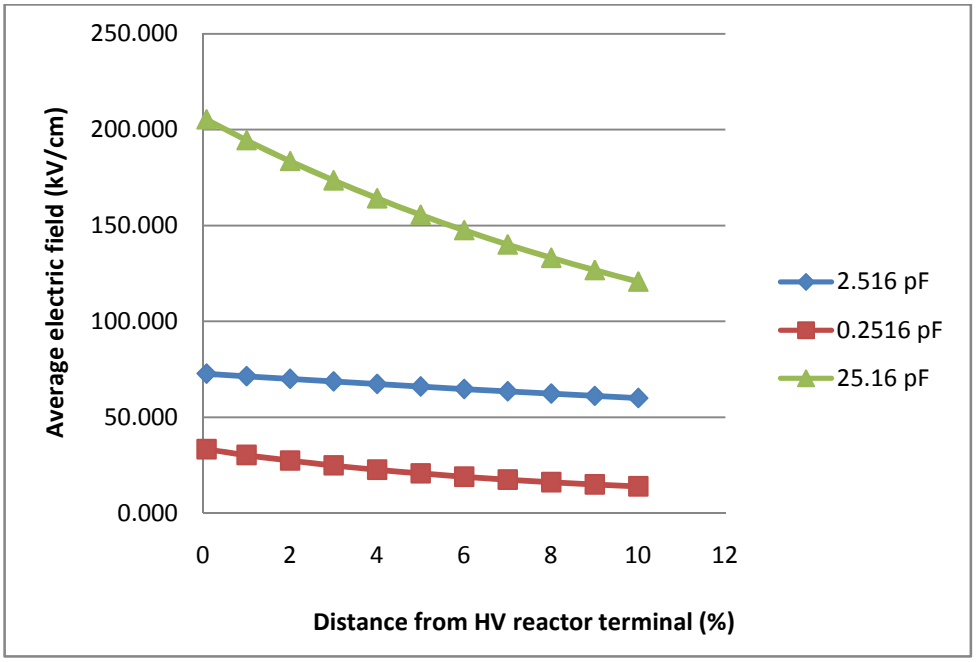

Figure 6.8: Effect of capacitance-to-ground on electric field

The parametric analysis conducted in this section shows that, a reduction of the electric field strength is obtained by a) increasing the inter-turn capacitance, and b) reducing the capacitance-to-ground of a reactor. However, such a requirement of high inter-turn capacitance and low capacitance-to-ground is commonly associated with the reactor cost and design, as well as other electrical and mechanical factors to be considered. For instance, the insulation thickness and/or permittivity could be changed in order to increase the inter-turn capacitance. However, this decision is not

practically feasible as it may affect safety issues of the reactor design. A somewhat better alternative to improve the voltage distribution across the reactor winding, and consequently the inter-turn electric field strength is by controlling the capacitance-to-ground (C_g). This is predominantly achieved by controlling the height of a reactor above the ground. The capacitance-to-ground is also dependent on electrodes configuration, such radial gap and the circumferential areas between the windings. These parameters are usually fixed according to optimum electrical design considerations.

6.6 Possible Failure Mechanism of MSCDN Reactors

Analyses conducted in the previous sections demonstrate the dominating factors of the reactor failures that happen during service operation. Solid insulating materials are subjected to various failure mechanisms such as tracking, surface and partial discharges, thermal ageing, heat distortion, thermal instability due to electrical losses, and so on [6.2,6.11]. In order to develop a failure, each of these mechanisms requires its own set of particular conditions. In some cases, more than one failure mechanism can occur at the same time or sequentially [6.2].

In this thesis, analysis was carried out to determine the electric field strength applied at the winding insulation during the worst condition of MSCDN energisation. The outcome of this analysis points to the following parameters as possible influential factors that lead to transient overvoltages and insulation failures of the air-core reactor.

6.6.1 High Electric Field Strength

The filter reactor was exposed to high magnitude and steep transient overvoltages produced by energisation of the MSCDN bank. Such a voltage surge resulted in large

potential difference across the inter-turn windings at the reactor HV terminal, which subsequently generates high electric field on the insulation. Analytical computation of electric field strength was performed in Section 6.3. This revealed that a high electric field strength of 72 kV/cm was obtained on the winding turns located at a distance of approximately 0.1% from the reactor HV terminal. Although the calculated electric field is higher than its steady-state value, it is still below the dielectric strength of Mylar film specified by the manufacturer, which is 170 kV/cm [6.22]. It is postulated that the electric field alone may not be the dominating factor that causes insulation failures in the reactor winding, but a repeated switching overvoltage at this level may help degrade the insulation.

6.6.2 High Rate of Change of Voltage (dV/dt)

The analysis was performed, as described in Section 6.4, to investigate the fast-changing voltage induced by the energisation, and the subsequent effect of this voltage change on the displacement current of the inter-turn insulation. In the computation, the capacitive current due to the fast rising of the voltage was obtained approximately 350 A. This current by itself is not harmful to the insulation until it reaches a sufficiently high level, and leads for some energy losses [6.2]. A synergistic effect of dielectric stress and dielectric heating is proposed to be the influencing failure mechanism of the reactor insulation failure.

Energisation of MSCDN results in high electric field strength, a very steep inter-turn voltage, and consequently an extremely high capacitive current on the inter-turn insulation of the reactor winding. Although not all of these factors are overwhelming, they are recurring phenomena and followed by the continuous steady

state currents and voltages, and as a result, they are damaging to the insulation, which may lead to failure after a number of months or years in service.

6.6.3 Effect of the Surge Arrester Operation

With reference to the MSCDN simulation circuit shown in Chapter 4 (refer Figure 4.14), surge arresters were installed across the filter reactor and the damping resistor, respectively to provide necessary protection against overvoltages. Figure 6.9 shows the maximal voltage across the filter reactor obtained when the MSCDN was switched in at the instant of the voltage maximum. The current flow through the surge arrester connected parallel to the filter reactor is also computed, as shown in Figure 6.10. As can be seen, even though the magnitude of the arrester current is small, the rate-of-rise of the current is very high. Comparison of Figures 6.9 and 6.10 shows that the surge arrester has operated at voltage maximum around t=25 ms. The limiting effect of the current through the surge arrester on the reactor voltage can be seen in Figure 6.9, at about t=25 ms. Near to the maximum peak, there is a rapid voltage deviation from the sinusoidal waveform.

For comparison, the MSCDN energisation is also simulated in the absence of the surge arresters, and the effect on the generated transient overvoltage at the reactor is observed. Figure 6.11 presents the computed reactor voltage for this simulation case. As can be seen, the reactor voltage does not show any noticeable voltage spikes when the surge arrester is not installed in the system. By comparing the results obtained in Figures 6.9 and 6.11, it is evident that the steep voltage change occurred at the filter reactor is caused by the surge arrester operation. Such a voltage course may lead to dangerous stresses in the turn-to-turn insulation of the reactor winding.

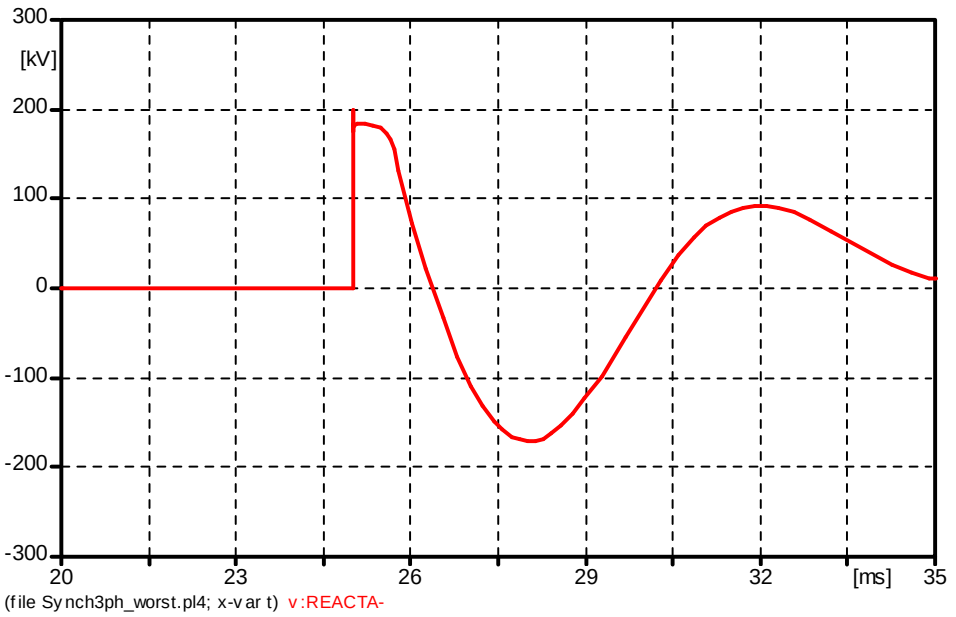

Figure 6.9: Maximal reactor voltage with the surge arrester installed across the reactor

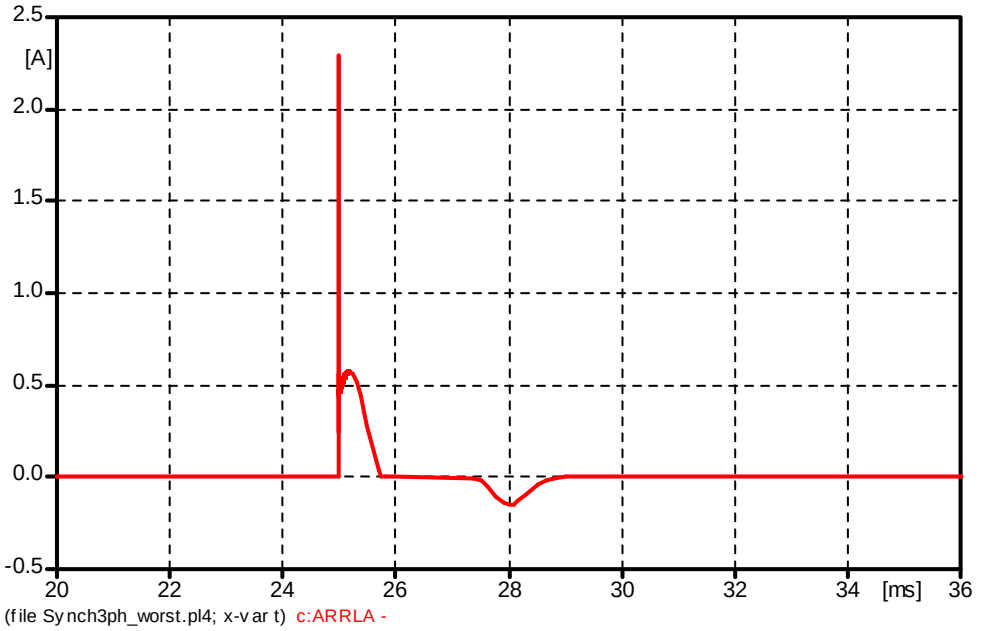

Figure 6.10: Current of the reactor surge arrester

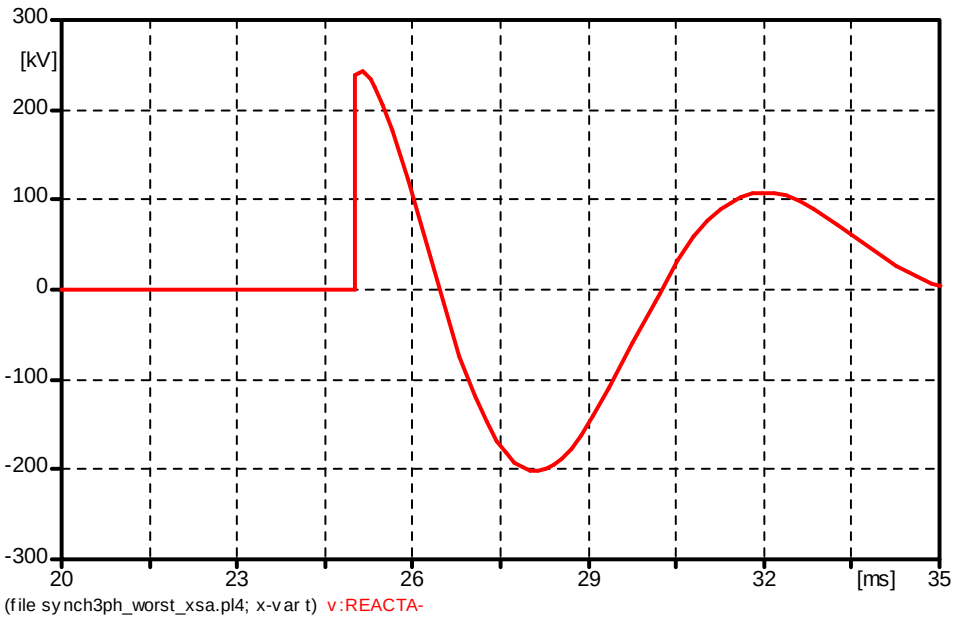

Figure 6.11: Reactor voltage without surge arrester installed across the reactor

6.7 Conclusion

This chapter described the computation of the electric field strength based on the simulation results obtained using the detailed reactor model. In the analysis, the voltage distribution along the reactor winding is examined, at times very close to the instant of switching. It is observed that the voltage distribution is highly non-uniform, in particular for the upper 10% of the reactor winding. A new relationship between the reactor design parameters and the maximum peak value of transient overvoltage was developed, which led to a simple procedure for evaluating the maximum electric field strength along the reactor winding.

Based on the investigation conducted, a proposal is put forward for the failure mechanism of the insulation as was experienced by some reactors during service operation. The first deciding factor that determines the insulation failure is the voltage distribution after the MSCDN energisation. Evidence of voltage non-

uniformity calculated at five different time intervals after the switching operation is established. High nonlinearity means that some parts of the reactor are disproportionately stressed by the high electric field strength. A parametric analysis was undertaken to ascertain the influence of the reactor parameters on the applied electric field strength. Based on this investigation, it is found that a reduction in the electric field strength can be obtained by increasing the inter-turn winding capacitance and/or reducing the capacitance-to-ground of the reactor. It is proposed that controlling the height of a reactor above the ground plane to reduce the effect of the capacitance-to-ground is practically feasible to reduce the effect of electric field.

Second, the transient stresses impressed on the insulating materials also depend on how the voltage changed in response to the filter energisation. In the MSCDN energisation studies, very steep voltage change, or high dV/dt, is observed, which causes large capacitive dielectric current to flow through the inter-turn insulation. Such a high dielectric current, combined with the follow-on steady state current contributes to excessive Joule heating imposed on the inter-turn insulation of the reactor winding, which eventually may lead to the reactor failure after repeated occurrence of the stress.

Third, while the surge arrester provides necessary protection for the reactor, the limiting effect of the current through the surge arrester induces high transient overvoltages across the reactor. Comparison of the simulations conducted with and without the surge arrester shows that a very steep voltage change was established at the reactor when the surge arrester has operated. Steep voltage change is known to cause non-linear voltage distribution along the reactor winding.

Chapter 7: General Conclusion, Discussion and Future Works

This chapter discusses the main conclusions and recalls the key parts of the work undertaken. Future work is also proposed.

The work carried out in this thesis focuses on the transient performance of reactors employed in reactive power compensation. Var compensation improves power systems performance, helping to increase reliability and the quality of power delivered to the customers. Shunt reactive compensation can be inductive or capacitive. In transmission substation, both inductive and capacitive reactive compensation is installed. At load level, at the distribution substation, and along the distribution feeder, compensation is usually capacitive.

The aim of the work presented in this thesis is to determine the transient phenomena associated with two types of reactive power compensation equipment, namely the shunt reactors and the MSCDN. In service, this equipment is frequently switched to provide the intended steady-state voltage control in the power system. During the switching operations, transient overvoltages and overcurrents are likely to develop due to sudden interruption of the reactive current by the circuit breaker. The severity of the generated transients is dictated by several factors, such as the type of circuit breaker that performed the switching operation, the point-on-wave of the switching instant, the circuit arrangements, and so on. In the present work, the determinations of transient stresses to which the shunt reactor and the MSCDN are subjected during the switching operation are conducted using ATP simulations and analytical calculations.

For shunt reactors, the objectives of transient analysis include the identification of the event’s origin, the description of the deenergising transient overvoltages, and the

interpretation of important phenomena related to the event, particularly the impact of the reactor switching on the circuit breaker grading capacitor. The first step of the analysis is the calculation of overvoltages generated during the deenergisation using the Laplace transform method. The results obtained provide a rough idea about the characteristics of the transient phenomena as well as the resulting overvoltages that occurred.

In this work, the theory of how transient overvoltages are generated was revealed for shunt reactors. A review of previous research work, including control and mitigation techniques for shunt reactor switching, were highlighted. Overvoltages associated with shunt reactor deenergisation were estimated analytically using the Laplace transform method. The calculation was performed by considering the interchange of energy between the inductance and the capacitance of the shunt reactor at the time of disconnection. In transient analysis, the Laplace transform technique is mostly used analytical method, mainly because it automatically takes the initial conditions into account. Apart from analytical calculations, accurate calculation of voltages would be impractical without the use of computer programs. In this thesis, the ATP/EMTP program was used to reproduce the shunt reactor switching overvoltages at a 275 kV operational substation.

The disconnection of the shunt reactor was particularly examined at 0° and 90°on the voltage waveform of Phase A, which are considered the most important instants for a comparative data of the switching overvoltages. With a random opening of the circuit breaker, high overvoltages are generated. Reduction of these amplitudes can be achieved with switching at current zero, which corresponds to the moment of minimum energy stored in the reactor. In addition, the influences of chopped current

on the overvoltage have been examined. Higher chopping level provokes excessive overvoltages across both the reactor and the grading capacitors of the circuit breaker.

For transient analysis of the MSCDN, the objectives include the identification of the event origin, the description of the energising transient overvoltages and overcurrents, and the interpretation of important phenomena related to the event, particularly the impact of the MSCDN switching on the air-core filter reactor.

Review of previous research works justifies the importance of transient analysis of the MSCDN. It is shown that circuit breakers that close to energise the MSCDN can induce fast-front transients as the voltage across the open contact collapses very rapidly (in 1-10 nanoseconds). This generates fast-front transients with a similar rise time travelling toward the energised MSCDN, particularly impinging on the lower voltage components (C_2, L_f, and R_d). It was clearly demonstrated that the filter reactor was severely affected by such an energising transient. Switching that occurs near the amplitude of a line-to-neutral voltage resulted in the worst energising transient across the filter reactor.

In the present work, the MSCDN configuration was simulated to include the presence of surge arresters. These simulations have shown that extremely fast transient voltages are developed across the filter reactor when the MSCDN was connected to the system at the instant of system voltage maximum. The detailed modelling of the reactor structure was then undertaken to address the identified transient voltage phenomena. A detailed lumped parameter circuit model was developed, which accounts for the inter-turn RLC parameters as well as the stray capacitances-to-ground. The calculations of RLC winding parameters were performed using a set of analytical equations derived from the winding geometry and

insulation material of the reactor winding. The derived model was then incorporated in the ATP/EMTP simulations of the MSCDN energisation and the voltage distributions across the reactor winding at different time intervals were established. Good agreements were achieved when comparing the results obtained with the calculation and measurements data published by other works.

By subdividing the reactor length into a number of sections, it was demonstrated that the top coil turns of the reactor experience very high voltages. From the simulation results obtained, it is shown that high magnitude voltages with fast rise times are developed across the inter-turn insulation located at the top of the reactor (HV side).

The computation of the applied electric field strength on the reactor winding was then undertaken, using a simplified analytical approach. A new relationship was established between the highest overvoltage and the length of the reactor winding. This expression enables a quick and simple procedure that calculates the dielectric strength at various points on the reactor winding based on the voltage distribution obtained across the winding.

The reactor parameters influence the generated overvoltages, and consequently the applied electric field, in a very complicated manner. For this reason, a parametric analysis is carried out to obtain some general tendencies that illustrate the significance of parameter variations. It is shown that the transient response of an air-core reactor is mainly dependent on the shunt losses (R_{pk}), the turn-to-turn (C_{tk}), and the turn-to-ground capacitive (C_{gk}) couplings. Some of these parameters could be controlled in practice to improve the transient response of the reactor. However, any changes made on the winding parameters intended for a better transient response

must be thoroughly planned and understood in order to avoid any adverse effect on the steady-state operation of the reactor.

A mechanism for the failure of air-core reactors, as used on the 400kV MSCDN, is proposed based on simulations of the switching operations and a detailed model of the reactor. Based on extensive calculations performed in this work, it is postulated that the combination of high field magnitude and high dielectric current constitute extreme stresses on the inter-turn insulation of the winding caused by the MSCDN energisation. Such transient stresses, followed by steady-state thermal effects, may initiate the failure process in the reactors as experienced in the field. In addition to the above factors, the influence of surge arrester operation on the overvoltage occurred at the reactor terminal is also investigated. For this purpose, simulations of the MSCDN energisation were conducted with and without the surge arresters installed across the filter reactor. No dangerous overvoltages were observed at the reactor terminal when the MSCDN was energised in the absence of the surge arresters. In contrast, it is shown that energisation of the MSCDN at an unfavourable instant has initiated the operation of the reactor surge arrester. It is proposed that the limiting effect of the current through the surge arrester results in high dV/dt of the reactor voltage, which in turn causes non-linear voltage distribution across the reactor winding.

7.1 Future Work

In this thesis, important transient issues of shunt reactors and MSCDN switching were addressed through analytical calculations and computer simulations. With regard to shunt reactor switching, an in-depth study on the electrical stresses that affected the circuit breaker grading capacitor during shunt reactor switching should

be conducted. Although there has been research carried out to determine the electrical stresses associated with grading capacitors, the calculations that were performed faced some difficulties. Voltages and currents resulting from switching operations are difficult to calculate unless the stray impedances of the circuit breakers are known more accurately. Furthermore, the level that the transient voltage may reach before the other interrupter reignites or prestrikes mainly depends on the time interval that elapses until the second reignition or prestrike occurs. However, there is also little information available on the possible intervals between reignition or prestriking of the interrupters of a pole. All of these shortcomings indicate a clear need for more research in this particular area of shunt reactor switching.

Particularly for the MSCDN, real measurements are important subject that should be considered in the transient analysis of its components. To further this investigation, the study could be extended to address such issues. Two important real measurements could be performed with regards to the MSCDN: the real measurement of voltages and currents during the MSCDN energisation at the 400 kV operational substation and a comparison between the transient response of the detailed air-core reactor model in Chapter 5 and measurements obtained in a laboratory. For the first study, the measured data could be compared with ATP/EMTP simulation results obtained in Chapter 4 of this thesis. The second study is recommended as potential future work, although good agreement of the results was achieved when comparing the response of the proposed model with other similar models in previous works.

In addition to these types of measurements, it would be beneficial to use other software, such as COMSOL for calculating the parameters of the proposed detailed

circuit model of the air-core reactor. Comparing the voltage responses of the proposed model and the COMSOL model should also be considered. It should be emphasised that a substantial and detailed parameter computation of the winding using COMSOL would require a detailed construction dimensions from manufactures. Extension of the electric field strength computation as described in Chapter 6 is also recommended as potential future work, as could the study on the dielectric behaviour of Mylar polyester films used specifically for air-core reactor winding insulation.

References

Chapter 1

1.1 NGT, *Ratings and General Requirements for Plant, Equipment and Apparatus for the NGT System and Connection Points To It*, in *National Grid Technical Specification: NGTS 1, Issue 5*. December 2003.

1.2 The National Grid Company plc, *An Introduction to Reactive Power*. Market Development, October 2001.

1.3 R.F. Dudley, M.Sharp, A.Castanheira, and B.B.Biglar, *"Reactors"*, in *Electric Power Transformer Engineering*, J.H. Harlow, 2nd ed, Tylor&Francis Group, LLC, 2007, ch. 10.

1.4 S.V.Kulkarni and S.A.Khaparde, *Transformer Engineering Design and Practice*, Marcel Dekker, Inc., 2004. Chp.7, pp.277-326.

1.5 D.M. German, and A. Haddad, *"Overvoltages and insulation coordination on transmission networks" in Advances in High Voltage Engineering", A. Haddad and D.Warne,* Eds. Stevenage, UK: IET, 2004, ch.7, pp. 309-345.

1.6 NG, *"National Electricity Transmission System Seven Year Statement"*. National Grid, Warwick, UK, May 2010.

1.7 N.M. MacLeod, J.J. Price, and I.W. Whitlock, "The Control of Harmonics Distortion on an EHV system by the use Capacitive Damping Networks", *Proc. IEEE 8th International Conference on Harmonics and Quality of Power (ICHQP-98),* 1998.

1.8 D. Jefferies, "Developing the highways of power", *Power Engineering Journal*, vol. 11, pp. 5-9, 1997.

1.9 *"Industrial A.C. Networks Affected by Harmonics-Application of Filters and Shunt Capacitors"*, International Electrotechnical Commission Standard IEC 61642-1997.

1.10 A. Haddad, 1991. *Attenuation and limitation of transient overvoltages on transmission systems*. PhD Thesis, University of Wales College of Cardiff (UWCC).

1.11 D.M. German, and A. Haddad, *"Overvoltages and insulation coordination on transmission networks" in Advances in High Voltage Engineering", A. Haddad and D.Warne,* Eds. Stevenage, UK: IET, 2004, ch.7, pp. 309-345.

1.12 J.A. Bonner, W.M. Hurst, R.G. Rocamora, R.F. Dudley, M.R Sharp, and J.A. Twiss, "Selecting Ratings for Capacitors and Reactors in Applications

involving Multiple Single-tuned Filters", *IEEE Trans. Power Delivery*, Vol.10, No.1, 1995.

1.13 A. Greenwood, *Electrical Transients in Power Systems*. 2nd ed. New York: John Wiley and Sons, Inc., 1991.

1.14 *"IEEE Application Guide for Shunt Reactor Switching"*, IEEE Std. C37.015-1993, 1993.

1.15 I. Uglešić, S. Hutter, M. Krepela, B. Filipovic-Grcic, and F. Jakl, "Transients due to Switching of 400 kV Shunt Reactor", *International conference on power system transient (IPST)*, Rio de Janeiro, Brazil, Paper No.045. 2001.

1.16 L. Prikler, G. Ban and G. Banfai, "EMTP models for simulation of shunt reactor switching transients," *Int. Journal of Electrical Power & Energy Systems*, Elsevier Science (UK),Vol 19, pp 235- 240. 1997.

1.17 Canadian/American EMTP User Group, *"Alternative Transients Program RulBook"*, 1987-1995.

1.18 *Mathcad 13 User's Guide*, Mathsoft Engineering & Education, Inc. 2005.

Chapter 2

2.1 *"Power Transformer-Part 6: Reactors"*, British Standard BS EN 60076-6, 2008.

2.2 *High-voltage Switchgear and Controlgear-Part 110: Inductive Load Switching*, British Standard BS EN 62271-110, 2005.

2.3 R.F. Dudley, M. Sharp, A. Castanheira, and B.B. Biglar, *"Reactors"*, in *Electric Power Transformer Engineering*, J.H. Harlow, 2nded, Tylor & Francis Group, LLC, 2007, ch. 10.

2.4 R. S.Vedam and M.S. Sarma, *Power Quality VAR Compensation in Power Systems*, USA, CRC Press, 2009.

2.5 *"IEEE Application Guide for Shunt Reactor Switching"*, IEEE Std. C37.015-1993, 1993.

2.6 Shunt Reactors in Power Systems, Tech News, AREVA T&D.

2.7 L. Ching-Yin, C. Chang-Jhih, C. Chao-Rong, and H. Yen-Feng, "Comparison of transient phenomena when switching shunt reactors on the line's two terminals and station busbar," *International Conference on Power System Technology (PowerCon 2004)*, Vol.2,pp. 1255-1260, 2004.

2.8 *Transformer Handbook*, ABB Group, 2004 Ch.1, pp. 37-59.

2.9 X. Wang and M. R. Iravani, "Energization transients of shunt reactors," *IEEE Transactions on Power Systems*, vol. 12, pp. 1626-1631, 1997.

2.10 A.C.O. Rocha and J.C. Mendes, "Assesment of an EHV Shunt Reactor Insulation and Mechanical Performance by Switching Surge Analyses", *Cigre Session*, A2-301, Paris, 2006.

2.11 C. D. Tsirekis, et al., "Control of shunt reactor inrush currents in the Hellenic-Interconnected Power System," *IEEE Transactions on Power Delivery*, vol. 20, pp. 757-764, 2005.

2.12 I. Uglešić, S. Hutter, M. Krepela, B. Filipovic-Grcic, and F. Jakl, "Transients due to Switching of 400 kV Shunt Reactor", *International conference on power system transient (IPST)*, Rio de Janeiro, Brazil, Paper No.045. 2001.

2.13 D. F. Peelo, et al., "Shunt reactor switching tests in BC Hydro's 500 kV system," *IEE Proceedings on Generation, Transmission and Distribution*, vol. 135, pp. 420-434, 1988.

2.14 D. F. Peelo and E. M. Ruoss, "A new IEEE Application Guide for Shunt Reactor Switching," *IEEE Transactions on Power Delivery*, Vol. 11, pp. 881-887, 1996.

2.15 D. F. Peelo, B.R. Sunga, and R.P.P. Smeets, "Stresses on shunt reactors due to switching," *Cigre Session*, A2-304, Paris, 2008.

2.16 *Operating Environment of Voltage Grading Capacitors Applied to High Voltage Circuit-breakers*, CIGRE Technical Guide No.368, WG A3.18, February 2009.

2.17 L. Prikler, G. Ban and G. Banfai, "EMTP models for simulation of shunt reactor switching transients," *Int. Journal of Electrical Power & Energy Systems*, Elsevier Science (UK),Vol 19, pp 235- 240. 1997.

2.18 L. Cipcigan, et al., "Analysing a 400 kV power system for an expert system switching," *10th Mediterranean Electrotechnical Conference (MELECON 2000)*, Vol.3, pp. 999-1002, 2000.

2.19 S. Bojic, I. Uglesic, and N. Jaman, "Transient Phenomena by Controlled Switching of High Voltage Shunt Reactor in 123 kV Transmission Network", *16th International Symposium on High Voltage Engineering (ISH2009)*, Cape Town, South Africa, Aug. 2009.

2.20 P.F. Coventry and A. Haddad, “Electrical Operating Environment of Circuit-breaker Grading Capacitors: Use of Non-contact Voltage Probes”, First *UHVnet Colloquium*,Cardiff, United Kingdom, 2005.

2.21 P.F. Coventry and M. Runde, “Electrical Stresses on Circuit-breaker Voltage Grading Capacitors caused by Unequal Voltage Sharing during Switching Operations”, *European Transactions on Electrical Power*, Wiley Online Library, March 2010, pp.174-179.

2.22 D. Jefferies, "Developing the highways of power", *Power Engineering Journal*, vol. 11, pp. 5-9, 1997A.

2.23 N.M. MacLeod, J.J. Price, and I.W. Whitlock, “The Control of Harmonics Distortion on an EHV system by the use Capacitive Damping Networks”, *Proc. IEEE 8th International Conference on Harmonics and Quality of Power (ICHQP-98)*, 1998.

2.24 *Guide to the Specification and Design Evaluation of AC Filters for HVDC Systems*, CIGRE Technical Guide No.139, CIGRE WG 14.30, April 1999.

2.25 V. Ayadurai, *Electrical Application Substation Design Guide* [Online]. Available: http://www.scribd.com/doc/55158137/Electrical-Application-Substation-Design-Guide

2.26 MSCDN-Mechanical Switched Capacitive Damping Network, Bulletin PTD H166/MC, SIEMENS, 2005.

2.27 R.C. Campos, D.O. Lacerda, and M.F. Alves, “Mechanically Switched Capacitor with Damping Network (MSCDN)-Engineering Aspects of Application, Design, and Protection”, *2010 IEEE/PES Transmission and Distribution Conference and Exposition*: Latin America, 2010.

2.28 Y.Xiao, J.Zhao and S.Mao, “Theory for the Design of C-type Filter”, *Proc. IEEE 11th International Conference on Harmonics and Quality of Power (ICHQP-04*), New York, 2004.

2.29 J.A. Bonner, W.M. Hurst, R.G. Rocamora, R.F. Dudley, M.R Sharp, and J.A. Twiss, “Selecting Ratings for Capacitors and Reactors in Applications involving Multiple Single-tuned Filters”, *IEEE Trans. Power Delivery*, Vol.10, No.1, 1995.

2.30 M. Kizilcay, K. Teichmann, A. Agdemir, and G. Kaflowski, “Flashovers at a 33-kV Filter Reactor during Energization”, *International conference on power system transient (IPST)*, Lyon, France, 2007.

2.31 A. Kalyuzhny, S. Zissu, and D. Shein, "Analytical Study of Voltage Magnification Transients Due to Capacitor Switching," *IEEE Transactions on Power Delivery*, vol. 24, pp. 797-805, 2009.

2.32 J.H.R. Enslin, J. Knijp, C.P.J. Jansen, and J.H. Schuld, "Impact of Reactive Power Compensation Equipment on the Harmonic Impedance of High Voltage Networks", *IEEE PowerTech-2003*, Bologna, Italy, 23-26 June 2003.

2.33 *"IEEE Standard Requirements, Terminology, and Test Code for Dry-Type Air-Core Series-Connected Reactors"*, IEEE Std. C57.16-1996.

2.34 Dry-type Air-core Reactors, Bulletin E600, 2007, Trench Electric Ltd, Toronto Canada.

2.35 R.F. Dudley, M.Sharp, A.Castanheira, and B.B.Biglar, *"Reactors"*, in *Electric Power Transformer Engineering*, J.H. Harlow, 2nded, Tylor&Francis Group, LLC, 2007, ch. 10.

2.36 M.J. Heatcote, *The J&P Transformer Book*, 12thed, Great Britain, Newnes, 1998.

2.37 S.V.Kulkarni and S.A.Khaparde, *Transformer Engineering Design and Practice*, Marcel Dekker, Inc., 2004. Chp.7, pp.277-326.

2.38 M.M.A. Salama, "A Calculation Method for Voltage Distribution in a Large Air Core Power Reactor", *IEEE Trans. PAS*, Vol. PAS-100, No.4, pp.1752-1758, 1981.

2.39 A.A. Dahab, P.E. Burke, and T.H. Fawzi, "A Complete Model of a Single Layer Air-cored Reactor for Impulse Voltage Distribution". *IEEE Transactions on Power Delivery*, Vol. 3(4), pp. 1745-1753, 1988.

2.40 S.L. Varricchio and N.H.C. Santiago, "Transient Voltage Distribution in Air Core Reactors", *8th International Symposium on High Voltage Engineering (ISH93)*, Yokohama, Japan, 1993, pp. 221-224.

2.41 S.L. Varricchio and N.H.C. Santiago, "Electrical Strength in Air Core Reactors", *Proceedings of the 4th International Conference on Properties and Applications of Dielectric Materials*, Brisbane, Australia, 1994.

2.42 P. Holmberg, Modelling of Transient Response of Windings, Laminated Steel Cores and Electromagnetic Power Devices by Means of Lumped Circuits. PhD Thesis, Uppsala University, 2000.

2.43 P. S. Maruvada and N. Hylten-Cavallius, "Capacitance calculations for some basic high voltage electrode configurations," *IEEE Transactions on Power Apparatus and Systems*, vol. 94, pp. 1708-1713, 1975.

2.44 F. Grover, *Inductance Calculations; Working Formulas and Tables*. New York: Van Nostrand, 1946.

2.45 F. W. Grover, "Formulas and Tables for the Calculation and Design of Single-Layer Coils," *Proceedings of the Institute of Radio Engineers,* vol. 12, pp. 193-208, 1924.

2.46 T. H. Fawzi and P. E. Burke, "The Accurate Computation of Self and Mutual Inductances of Circular Coils," *IEEE Transactions on Power Apparatus and Systems,* vol. 97, pp. 464-468, 1978.

2.47 B.Basavaraja and D.V.S.S. Siva Sarma, “Impact of Non-uniform Distribution of Voltage on Stator Winding of PWM Fed Induction Motor”, *IEEE International Conference on Powertech*, 2007.

2.48 Mylar Electrical Properties, *Product Information*, DuPont Teijin Films, USA.

Chapter 3

3.1 L. Prikler, G. Ban and G. Banfai, “EMTP models for simulation of shunt reactor switching transients,” *Int. Journal of Electrical Power & Energy Systems,* Elsevier Science (UK),Vol 19, pp 235- 240. 1997.

3.2 I. Uglešić, S. Hutter, M. Krepela, B. Filipovic-Grcic, and F. Jakl, “Transients due to Switching of 400 kV Shunt Reactor”, *International conference on power system transient (IPST)*, Rio de Janeiro, Brazil, Paper No.045. 2001.

3.3 *Mathcad 13 User’s Guide*, Mathsoft Engineering & Education, Inc. 2005.

3.4 Canadian/American EMTP User Group, *"Alternative Transients Program Rule Book"*, 1987-1995.

3.5 H.W. Dommel, *"EMTP Theory Book"*, Microtran Power System Analysis Corporation, Vancouver, British Columbia, Canada, May 1992.

3.6 L.Prikler and H.K Hoidalen, *ATPDraw User’s Manual,* 1998.

3.7 A. L. Shenkman, *Transient Analysis of Electric Power Circuits Handbook*, Springer, Netherlands, 2005.

3.8 P.F. Coventry and A. Haddad, “Electrical Operating Environment of Circuit-breaker Grading Capacitors: Use of Non-contact Voltage Probes”, First UHVnet Colloquium, Cardiff, United Kingdom, 2005.

3.9 *Insulation Co-ordination - Part 4: Computational Guide to Insulation Coordinationand Modelling of Electrical Networks,* International Electrotechnical Commission Standard IEC 60071-4, 2004.

3.10 *Operating Environment of Voltage Grading Capacitors Applied to High-Voltage Circuit-breakers*, CIGRE Technical Guide No.368, WG A3.18, February 2009.

Chapter 4

4.1 R.C. Campos, D.O. Lacerda, and M.F. Alves, "Mechanically Switched Capacitor with Damping Network (MSCDN)-Engineering Aspects of Application, Design, and Protection", *2010 IEEE/PES Transmission and Distribution Conference and Exposition*: Latin America, 2010.

4.2 V. Ayadurai, *Electrical Application Substation Design Guide* [Online]. Available: http://www.scribd.com/doc/55158137/Electrical-Application-Substation-Design-Guide

4.3 A. L. Shenkman, *Transient Analysis of Electric Power Circuits Handbook*, Springer, Netherlands, 2005.

4.4 *High Voltage Surge Arresters – Buyer's Guide*, 6.0 ed., ABB, Ludvika, Sweden, 2008-08.

4.5 A. Kalyuzhny, S. Zissu, and D. Shein, "Analytical Study of Voltage Magnification Transients Due to Capacitor Switching," *IEEE Transactions on Power Delivery*, vol. 24, pp. 797-805, 2009.

4.6 Y.Xiao, J.Zhao and S.Mao, "Theory for the Design of C-type Filter", *Proc. IEEE 11th International Conference on Harmonics and Quality of Power (ICHQP-04*), New York, 2004.

4.7 J.A. Bonner, W.M. Hurst, R.G. Rocamora, R.F. Dudley, M.R Sharp, and J.A. Twiss, "Selecting Ratings for Capacitors and Reactors in Applications involving Multiple Single-tuned Filters", *IEEE Trans. Power Delivery*, Vol.10, No.1, 1995.

4.8 N.M. MacLeod, J.J. Price, and I.W. Whitlock, "The Control of Harmonics Distortion on an EHV system by the use Capacitive Damping Networks", *Proc. IEEE 8th International Conference on Harmonics and Quality of Power (ICHQP-98)*, 1998.

4.9 *Guide to the Specification and Design Evaluation of AC Filters for HVDC Systems*, CIGRE Technical Guide No.139, CIGRE WG 14.30, April 1999.

4.10 Y. H. Fu, "Simulation Study on the Switching Transients during de-generation of Filter and Capacitor Banks," *Sixth International Conference on AC and DC Power Transmission*, pp. 375-380, 1996.

4.11 J.H.R. Enslin, J. Knijp, C.P.J. Jansen, and J.H. Schuld: “Impact of Reactive Power Compensation Equipment on the Harmonic Impedance of High Voltage Networks”, *IEEE PowerTech-2003*, Bologna, Italy, 23-26 June 2003.

4.12 *“IEEE Standard Requirements, Terminology, and Test Code for Dry-Type Air-Core Series-Connected Reactors”*, IEEE Std. C57.16-1996.

4.13 *Electrical insulation systems-Electrical stresses produced by repetitive impulses-Part 1: General method of evaluation of electrical endurance*, British Standard, BS EN 62068-1, 2003.

4.14 NG, *"National Electricity Transmission System Seven Year Statement"*. National Grid, Warwick, UK, May 2010.

4.15 *“Industrial A.C. Networks Affected by Harmonics-Application of Filters and Shunt Capacitors”*, International Electrotechnical Commission Standard IEC 61642-1997.

Chapter 5

5.1 *Insulation Co-ordination - Part 2: Application Guide*, International Electrotechnical Commission Standard IEC 60071-2, 1997.

5.2 A. Greenwood, *Electrical Transients in Power Systems*. 2nd ed. New York: John Wiley and Sons, Inc., 1991.

5.3 P. Holmberg, Modelling of Transient Response of Windings, Laminated Steel Cores and Electromagnetic Power Devices by Means of Lumped Circuits. PhD Thesis, Uppsala University, 2000.

5.4 M. Enohnyaket, PEEC Modelling and Verification for Broadband Analysis of Air-Core Reactors. PhD Thesis, Lulea University of Technology, 2007.

5.5 H. W. Dommel, "Digital Computer Solution of Electromagnetic Transients in Single-and Multiphase Networks," *IEEE Transactions on Power Apparatus and Systems*, vol. PAS-88, pp. 388-399, 1969.

5.6 B.M.Dent, E.R.Hartill and J.E.Miles, “A Method of Analysis of Transformer Impulse Voltage Distribution Using a Digital Computer”, *Proc. IEE*, Vol.105, Pt. A. pp. 445-459, 1958.

5.7 J. H. McWhirter, "Calculation of impulse voltage stresses in transformer windings," *IEEE Conference Proceeding on Transmission and Distribution*, pp. 579-585, 1996.

5.8 W.J. McNutt, I.J. Blalock, and R.A. Hinton, “Response of Transformer Windings to System Transient Voltage”, *IEEE Trans. PAS*, Vol.PAS-93, pp.457-467, 1974.

5.9 F. de Leon and A. Semlyen, "Efficient calculation of elementary parameters of transformers," *IEEE Transactions on Power Delivery*, vol. 7, pp. 376-383, 1992.

5.10 R. Kasturi and G.R.K. Murthy, “Computation of Impulse Voltage Stresses in Transformer Windings”, *Proc. IEEE*, Vol.126, No.5, 1979.

5.11 M. Popov, L. Van der Sluis,R.P.P. Smeets, J.Lopez-Roldan, and V.V. Terzija, “Modelling, simulation and measurement of fast transients in transformer windings with consideration of frequency-dependent losses”, *IET Electrical Power Application*, Vol.1, No.1, pp.29-35, 2007.

5.12 M. Popov, R.P.P. Smeets, L. Van der Sluis, H. De Herdt, and J. Declercq, “Analysis of Voltage Distribution in Transformer Windings during Circuit Breaker Prestrike”, *the International Conference on Power Systems Transients (IPST2009)*, Kyoto, Japan, 3-6 June, 2009.

5.13 M.M.A. Salama, “A Calculation Method for Voltage Distribution in a Large Air Core Power Reactor”, *IEEE Trans. PAS*, Vol. PAS-100, No.4, pp.1752-1758, 1981.

5.14 M. M. A. Salama, *et al.*, "Calculation of Steady-State Surface at Winding Ends of Air-Core Power Reactors," *IEEE Transactions on Power Apparatus and Systems*, vol. PAS-100, pp. 3673-3678, 1981.

5.15 A.A. Dahab, P.E. Burke and T.H.Fawzi, “A Complete Model of a Single Layer Air-Cored Reactor for Impulse Voltage Distribution’, *IEEE Trans. Power Delivery*, Vol.3, No.4, pp.1745-1753, 1988.

5.16 S.L. Varricchio and N.H.C. Santiago, “Transient Voltage Distribution in Air Core Reactors”, *8th International Symposium on High Voltage Engineering (ISH1993)*, Yokohama, Japan, 1993, pp.221-224.

5.17 S.L. Varricchio and N.H.C. Santiago, “Electrical Strength in Air Core Reactors”, *Proceedings of the 4th International Conference on Properties and Applications of Dielectric Materials*, Brisbane, Australia, 1994.

5.18 J.O. Bird, *Electrical Circuit Theory and Technology*. Oxford: Butterworth-Heinemann, 1997.

5.19 F. Grover, *Inductance Calculations; Working Formulas and Tables*. New York: Van Nostrand, 1946.

5.20 P. Sarma Maruvada and N. Hylten-Cavallus, “Capacitance Calculations for Some Basic High Voltage Electrode Configurations”, *IEEE Trans. PAS*, Vol.PAS-94, pp.1708-1713, 1975.

5.21 Dry-type Air-core Reactors, Bulletin E600, 2007, Trench Electric Ltd, Toronto Canada.

5.22 *Evaluation and qualification of electrical insulation systems*. BS EN 60505, 2011.

Chapter 6

6.1 M. M. A. Salama and R. Hackam, "Voltage and Electric Field Distributions and Discharge Inception Voltage In Insulated Conductors," *IEEE Transactions on Power Apparatus and Systems*, vol. PAS-103, pp. 3425-3433, 1984.

6.2 N.M. MacLeod, J.J. Price, and I.W. Whitlock, “The Control of Harmonics Distortion on an EHV system by the use Capacitive Damping Networks”, *Proc. IEEE 8th International Conference on Harmonics and Quality of Power (ICHQP-98)*, 1998.

6.3 I. Romano and R. Schifani, "Effects of 3rd-harmonic voltage content on dielectric losses of solid insulating materials," *IEE Proceedings Electric Power Applications*, vol. 128, pp. 119-125, 1981.

6.4 A.G. Day, *Failure Mechanism of Solid Electrical Insulation*, Letterhead: ERA Technology Ltd., 1988.

6.5 E. Kuffel, W.S. Zaengl, and J. Kuffel, *High Voltage Engineering Fundamentals*, 2nd Ed. Great Britain, Butterworth-Heineman, 2000.

6.6 A. M. Mahdy, A. El-Morshedy, and H.L. Anis, "Insulation failure assessment under random energizationovervoltages," *IEEE Transactions on Industry Applications*, vol. 32, pp. 214-220, 1996.

6.7 X. Wei, C. Shukang, W. Jian’er, and W. Yonghong, "Research on turn-to-turn insulation test method of dry-type air-core reactor," *Proceedings of the 6th International Conference on Properties and Applications of Dielectric Materials*, vol.2, pp. 1058-1061, 2000.

6.8 Y. Xiuke and Y. Jian, "Calculation of Wave Process in an Air Core Reactor," *International Conference on Energy and Environment Technology, 2009. (ICEET '09)*, pp. 96-98, 2009.

6.9 Y. Xiuke, Y. Jian, and C. Yu, "Electric Field Analysis of Air Core Power Reactor," *Asia-Pacific Power and Energy Engineering Conference (APPEEC)*, pp. 1-3, 2010.

6.10 X. Mei,L. Tiecheng, S. Ziming, G. Ting, and Y. Long, “Based on the BEM of Internal Electric Field Simulation of Shunt Dry Reactor,” in *Asia-Pacific Power and Energy Engineering Conference (APPEEC)*, pp. 1-4, 2011.

6.11 *Evaluation and Qualification of Electrical Insulation System*, British Standard BS EN 60505, 2011.

6.12 J.O. Bird, *Electrical Circuit Theory and Technology*. Oxford: Butterworth-Heinemann, 1997.

6.13 A. Ahmad and P. Auriol, "Dielectric losses in power transformers under high frequency transients," in *Electrical Insulation, Conference Record of the 1992 IEEE International Symposium on*, 1992, pp. 460-463.

6.14 A.K. Lokhanin, T.I. Morozova, G.Y. Shneider, V.V. Sokolov, and V.M. 62Chornogotsky, “Internal Insulation Failure Mechanism of HV Equipment under Service Conditions”, *Cigre Session*, Paper 15-201, Paris 2002.

6.15 N. Foulon, J-P. Lucas, G. Barre, R. Mailfert, and J. Enon, "Investigation of the failure mechanism of insulation subjected to repetitive fast voltage surges," in *Electrical Insulation Conference, 1997, and Electrical Manufacturing & Coil Winding Conference. Proceedings*, 1997, pp. 401-406.

6.16 C. Mayoux, "Degradation of insulating materials under electrical stress," *IEEE Transactions on Dielectrics and Electrical Insulation*, vol. 7, pp. 590-601, 2000.

6.17 R. Bruetsch, "High Voltage Insulation Failure Mechanisms," *IEEE International Symposium on Electrical Insulation (ISEI 2008)*, pp. 162-165, 2008.

6.18 A.A. Dahab, P.E. Burke and T.H.Fawzi, “A Complete Model of a Single Layer Air-Cored Reactor for Impulse Voltage Distribution’, *IEEE Trans. Power Delivery*, Vol.3, No.4, pp.1745-1753, 1988.

6.19 *Insulation Co-ordination - Part 2: Application Guide*, International Electrotechnical Commission Standard IEC 60071-2, 1997.

6.20 M.J. Heatcote, *The J&P Transformer Book*, 12thed, Great Britain, Newnes, 1998.

6.21 R.F. Dudley, M.Sharp, A.Castanheira, and B.B.Biglar, *“Reactors”*, in *Electric Power Transformer Engineering*, J.H. Harlow, 2nded, Tylor&Francis Group, LLC, 2007, ch. 10.

6.22 *Product information*, Goodfellow, United Kingdom, 2011 [Online], Available: http://www.goodfellow.com/E/Polyethylene-terephthalate.html

APPENDIX A

```
%CALCULATION OF SELF INDUCTANCES
clc
clear
dr=0.902*10^2;  %Reactor inner diameter--cm
dw=0.00203*10^2; %Conductor diameter--cm
br=2.65*10^2; %Reactor length--cm
Nr=1224; %Total no of turns
bs=br/10; %10-section equal length
ns=Nr/10;%No of turns for one section
at=dr/2+dw/2;%Equal radii for all sections
%Diameter=2a=90.203, Length=b=26.42
sr=bs/(2*at);%Shape ratio for b less than 2a
%Pause: go to Newt_118 for K value
k=0.400093; %Nagaoka Constant-refer Newt_118.m
disp('SELF INDUCTANCE (118):')
L_ss=(0.002*k*pi^2*at*ns^2)/sr;%Self-inductance formula 118 in uH
Lss=L_ss/10^3;%Unit conversion to mH
Ls=sprintf('%.6g mH',Lss)

%NEWTON INTERPOLATION
clc
clear
%Reactor diam. and conductor diam. in cm
dr=90.2; %==2a
dw=0.203;
%Reactor length--cm
br=265;
%No of turns
Nr=1224;
%Winding density
nd=Nr/br;
%10-section length
bs=26.5; %==b
%Equal radii of all sections
at=dr/2+dw/2;
%Shape ratio for b less than 2a
sr=bs/(2*at)
%Tabular interval
z=0.01;
%Nagaoka constant k
f1=sr;
f0=0.29;
k0=0.397703;
d1=0.007566;
d2=-0.000192;
u=(f1-f0)/z;
kk=k0+u*d1+(u*(u-1)/factorial(2))*d2;
k=sprintf('%.6g',kk)

%CALCULATION OF MUTUAL INDUCTANCES
clc
clear
dr=0.902*10^2;  %Reactor inner diameter--cm
```

```
dw=0.00203*10^2; %Conductor diameter--cm
br=2.65*10^2; %Reactor length--cm
Nr=1224; %No of turns
nd=Nr/br;%Winding density
bs=br/10; %10-section equal length
at=dr/2+dw/2;%Equal radii of all sections
disp('MUTUAL INDUCTANCES:')

%Section 1 and 2
%Separation
s_2c=bs;
%Four axial distances
x1_2c=s_2c+bs;
x2_2c=s_2c;
x3_2c=s_2c;
x4_2c=s_2c-bs;
%Four diagonal distances
r1_2c=sqrt(at^2+x1_2c^2);
r2_2c=sqrt(at^2+x2_2c^2);
r3_2c=sqrt(at^2+x3_2c^2);
r4_2c=sqrt(at^2+x4_2c^2);
%Four ratios
p1_2c=at^2/r1_2c^2;
p2_2c=at^2/r2_2c^2;
p3_2c=at^2/r3_2c^2;
p4_2c=at^2/r4_2c^2;
%Pause: go to excel file for data interpolation
%Four Bn: Refer to Linear Interpolation Table 35 by Excel
B1_2c=0.9800072;
B2_2c=0.9346060;
B3_2c=0.9346060;
B4_2c=0.8488260;
%Mutual Inductance by Formula 108
rb14_2c=(r1_2c*B1_2c)+(r4_2c*B4_2c);
rb23_2c=(r2_2c*B2_2c)+(r3_2c*B3_2c);
sub_2c=rb14_2c-rb23_2c;
M_2c=(0.002*pi^2*at^2*nd^2*sub_2c)/10^3;
M2c=sprintf('%.6g mH',M_2c)

%Section 1 and 3
%Separation
s_3c=2*bs;
%Four axial distances
x1_3c=s_3c+bs;
x2_3c=s_3c;
x3_3c=s_3c;
x4_3c=s_3c-bs;
%Four diagonal distances
r1_3c=sqrt(at^2+x1_3c^2);
r2_3c=sqrt(at^2+x2_3c^2);
r3_3c=sqrt(at^2+x3_3c^2);
r4_3c=sqrt(at^2+x4_3c^2);
%Four ratios
p1_3c=at^2/r1_3c^2;
p2_3c=at^2/r2_3c^2;
p3_3c=at^2/r3_3c^2;
```

```
p4_3c=at^2/r4_3c^2;
%Four Bn: Linear interpolation of values from Table 35 by Excel
B1_3c=0.9931291;
B2_3c=0.9800072;
B3_3c=0.9800072;
B4_3c=0.934606;
%Mutual Inductance by Formula 108
rb14_3c=(r1_3c*B1_3c)+(r4_3c*B4_3c);
rb23_3c=(r2_3c*B2_3c)+(r3_3c*B3_3c);
sub_3c=rb14_3c-rb23_3c;
M_3c=(0.002*pi^2*at^2*nd^2*sub_3c)/10^3;
M3c=sprintf('%.6g mH',M_3c)

%Section 1 and 4
%Separation
s_4c=3*bs;
%Four axial distances
x1_4c=s_4c+bs;
x2_4c=s_4c;
x3_4c=s_4c;
x4_4c=s_4c-bs;
%Four diagonal distances
r1_4c=sqrt(at^2+x1_4c^2);
r2_4c=sqrt(at^2+x2_4c^2);
r3_4c=sqrt(at^2+x3_4c^2);
r4_4c=sqrt(at^2+x4_4c^2);
%Four ratios
p1_4c=at^2/r1_4c^2;
p2_4c=at^2/r2_4c^2;
p3_4c=at^2/r3_4c^2;
p4_4c=at^2/r4_4c^2;
%Four Bn:Linear interpolation of values from Table 35 by Excel
B1_4c=0.9972094;
B2_4c=0.9931291;
B3_4c=0.9931291;
B4_4c=0.9800072;
%Mutual Inductance by Formula 108
rb14_4c=(r1_4c*B1_4c)+(r4_4c*B4_4c);
rb23_4c=(r2_4c*B2_4c)+(r3_4c*B3_4c);
sub_4c=rb14_4c-rb23_4c;
M_4c=(0.002*pi^2*at^2*nd^2*sub_4c)/10^3;
M4c=sprintf('%.6g mH',M_4c)

%Section 1 and 5
%Separation
s_5c=4*bs;
%Four axial distances
x1_5c=s_5c+bs;
x2_5c=s_5c;
x3_5c=s_5c;
x4_5c=s_5c-bs;
%Four diagonal distances
r1_5c=sqrt(at^2+x1_5c^2);
r2_5c=sqrt(at^2+x2_5c^2);
r3_5c=sqrt(at^2+x3_5c^2);
r4_5c=sqrt(at^2+x4_5c^2);
```

```
%Four ratios
p1_5c=at^2/r1_5c^2;
p2_5c=at^2/r2_5c^2;
p3_5c=at^2/r3_5c^2;
p4_5c=at^2/r4_5c^2;
%Four Bn:Linear interpolation of values from Table 35 by Excel
B1_5c=0.9986975;
B2_5c=0.9972094;
B3_5c=0.9972094;
B4_5c=0.9931291;
%Mutual Inductance by Formula 108
rb14_5c=(r1_5c*B1_5c)+(r4_5c*B4_5c);
rb23_5c=(r2_5c*B2_5c)+(r3_5c*B3_5c);
sub_5c=rb14_5c-rb23_5c;
M_5c=(0.002*pi^2*at^2*nd^2*sub_5c)/10^3;
M5c=sprintf('%.6g mH',M_5c)

%Section 1 and 6
%Separation
s_6c=5*bs;
%Four axial distances
x1_6c=s_6c+bs;
x2_6c=s_6c;
x3_6c=s_6c;
x4_6c=s_6c-bs;
%Four diagonal distances
r1_6c=sqrt(at^2+x1_6c^2);
r2_6c=sqrt(at^2+x2_6c^2);
r3_6c=sqrt(at^2+x3_6c^2);
r4_6c=sqrt(at^2+x4_6c^2);
%Four ratios
p1_6c=at^2/r1_6c^2;
p2_6c=at^2/r2_6c^2;
p3_6c=at^2/r3_6c^2;
p4_6c=at^2/r4_6c^2;
%Four Bn:Linear interpolation of values from Table 35 by Excel
B1_6c=0.9993215;
B2_6c=0.9986975;
B3_6c=0.9986975;
B4_6c=0.9972094;
%Mutual Inductance by Formula 108
rb14_6c=(r1_6c*B1_6c)+(r4_6c*B4_6c);
rb23_6c=(r2_6c*B2_6c)+(r3_6c*B3_6c);
sub_6c=rb14_6c-rb23_6c;
M_6c=(0.002*pi^2*at^2*nd^2*sub_6c)/10^3;
M6c=sprintf('%.6g mH',M_6c)

%Section 1 and 7
%Separation
s_7c=6*bs;
%Four axial distances
x1_7c=s_7c+bs;
x2_7c=s_7c;
x3_7c=s_7c;
x4_7c=s_7c-bs;
%Four diagonal distances
```

```
r1_7c=sqrt(at^2+x1_7c^2);
r2_7c=sqrt(at^2+x2_7c^2);
r3_7c=sqrt(at^2+x3_7c^2);
r4_7c=sqrt(at^2+x4_7c^2);
%Four ratios
p1_7c=at^2/r1_7c^2;
p2_7c=at^2/r2_7c^2;
p3_7c=at^2/r3_7c^2;
p4_7c=at^2/r4_7c^2;
%Four Bn:Linear interpolation of values from Table 35 by Excel
B1_7c=0.9996145;
B2_7c=0.9993215;
B3_7c=0.9993215;
B4_7c=0.9986975;
%Mutual Inductance by Formula 108
rb14_7c=(r1_7c*B1_7c)+(r4_7c*B4_7c);
rb23_7c=(r2_7c*B2_7c)+(r3_7c*B3_7c);
sub_7c=rb14_7c-rb23_7c;
M_7c=(0.002*pi^2*at^2*nd^2*sub_7c)/10^3;
M7c=sprintf('%.6g mH',M_7c)

%Section 1 and 8
%Separation
s_8c=7*bs;
%Four axial distances
x1_8c=s_8c+bs;
x2_8c=s_8c;
x3_8c=s_8c;
x4_8c=s_8c-bs;
%Four diagonal distances
r1_8c=sqrt(at^2+x1_8c^2);
r2_8c=sqrt(at^2+x2_8c^2);
r3_8c=sqrt(at^2+x3_8c^2);
r4_8c=sqrt(at^2+x4_8c^2);
%Four ratios
p1_8c=at^2/r1_8c^2;
p2_8c=at^2/r2_8c^2;
p3_8c=at^2/r3_8c^2;
p4_8c=at^2/r4_8c^2;
%Four Bn: Linear interpolation of values from Table 35 by Excel
B1_8c=0.999766;
B2_8c=0.9996145;
B3_8c=0.9996145;
B4_8c=0.9993215;
%Mutual Inductance by Formula 108
rb14_8c=(r1_8c*B1_8c)+(r4_8c*B4_8c);
rb23_8c=(r2_8c*B2_8c)+(r3_8c*B3_8c);
sub_8c=rb14_8c-rb23_8c;
M_8c=(0.002*pi^2*at^2*nd^2*sub_8c)/10^3;
M8c=sprintf('%.6g mH',M_8c)

%Section 1 and 9
%Separation
s_9c=8*bs;
%Four axial distances
x1_9c=s_9c+bs;
```

```
x2_9c=s_9c;
x3_9c=s_9c;
x4_9c=s_9c-bs;
%Four diagonal distances
r1_9c=sqrt(at^2+x1_9c^2);
r2_9c=sqrt(at^2+x2_9c^2);
r3_9c=sqrt(at^2+x3_9c^2);
r4_9c=sqrt(at^2+x4_9c^2);
%Four ratios
p1_9c=at^2/r1_9c^2;
p2_9c=at^2/r2_9c^2;
p3_9c=at^2/r3_9c^2;
p4_9c=at^2/r4_9c^2;
%Four Bn:Linear interpolation of values from Table 35 by Excel
B1_9c=0.9998493;
B2_9c=0.999766;
B3_9c=0.999766;
B4_9c=0.9996145;

%Mutual Inductance by Formula 108
rb14_9c=(r1_9c*B1_9c)+(r4_9c*B4_9c);
rb23_9c=(r2_9c*B2_9c)+(r3_9c*B3_9c);
sub_9c=rb14_9c-rb23_9c;
M_9c=(0.002*pi^2*at^2*nd^2*sub_9c)/10^3;
M9c=sprintf('%.6g mH',M_9c)

%Section 1 and 10
%Separation
s_10c=9*bs;
%Four axial distances
x1_10c=s_10c+bs;
x2_10c=s_10c;
x3_10c=s_10c;
x4_10c=s_10c-bs;
%Four diagonal distances
r1_10c=sqrt(at^2+x1_10c^2);
r2_10c=sqrt(at^2+x2_10c^2);
r3_10c=sqrt(at^2+x3_10c^2);
r4_10c=sqrt(at^2+x4_10c^2);
%Four ratios
p1_10c=at^2/r1_10c^2;
p2_10c=at^2/r2_10c^2;
p3_10c=at^2/r3_10c^2;
p4_10c=at^2/r4_10c^2;
%Four Bn:Linear interpolation of values from Table 35 by Excel
B1_10c=0.9998995;
B2_10c=0.9998493;
B3_10c=0.9998493;
B4_10c=0.999766;
%Mutual Inductance by Formula 108
rb14_10c=(r1_10c*B1_10c)+(r4_10c*B4_10c);
rb23_10c=(r2_10c*B2_10c)+(r3_10c*B3_10c);
sub_10c=rb14_10c-rb23_10c;
M_10c=(0.002*pi^2*at^2*nd^2*sub_10c)/10^3;
M10c=sprintf('%.6g mH',M_10c)
```

```
 % CALCULATION OF SHUNT RESISTANCES
clc
clear
% Resistance of Mylar Dielectric
rho_my=10^18; %Resistivity of dielectric Mylar--ohm.cm
tm=0.00508;%Insulation thickness of the wire--cm
Nr=1224;   %No of turns
br=265;    %Reactor length--cm
bs=br/10;  %Length of one section--cm
ns=Nr/10;  %No of turns in one section
dr=90.2;   %Reactor diameter--cm
dw=0.203;  %Conductor diameter--cm
a=dr/2;    %Reactor radius
aw=dw/2;   %Conductor radius
disp('SHUNT RESISTANCE:')
area=2*pi^2*aw*a; %area=(2*pi*R)x(2*pi*r)/2
Rdt=(rho_my*2*tm)/area %R=(rho*l)/A, l=2x dielectric thickness
Rds=Rdt*(ns-1);%Resistance in series for one section
Rd=sprintf('%.6g ohm',Rds)

%CALCULATION OF SERIES RESISTANCES
clc
clear
%Reactor parameters
Nr=1224; %No of turns
br=2.65; %Reactor length
dr=0.902;%Reactor diameter in meter
dw=0.00203;%Conductor diameter in meter
rho=2.82*10^-8; %Resistivity of aluminium conductor-ohm.m
%Sections of reactor parameters
bs=0.265; %Section length
ns=Nr/10; %No of turns in one-section
%Formula requirements
Aw=(pi*dw^2)/4;%Effective area of the conductor
bt=pi*dr; %Length of one-turn=2*pi*R
disp('SERIES RESISTANCES: ')
%Winding resistance formula
Rww=(rho*bt*ns)/Aw; %(Rho*length of one-turn*no of turn per-section)/area)
Rw=sprintf('%.5g ohm',Rww)

%CALCULATION OF SERIES CAPACITANCES
% clc
% clear
%REACTOR
%Dielectric constant
epso=8.854*10^-12; %Vacuum F/m
epsr=3.0; %Mylar polyester film at 1 MHz
%Reactor diam. and conductor diam.--m
dr=0.902;
dw=0.00203;
%Insulation thickness--m
tm=0.00508*10^-2; %0.0000508 m
%Reactor length--m
br=2.65;
%No of turns
Nr=1243;
```

```
%Radius of reactor and conductor
a=dr/2;
aw=dw/2;
%SECTIONS
%No of sections
n=10;
%Section length
bs=br/n;
%No of turns of each section
ns=Nr/n;
%CALCULATION
%Turn-to-turn Capacitance by Parallel Plate Formula
disp('INTER-SECTION CAPACITANCE: ')
%Formula:(eps*(2pi*R)x(2pi*r)/2)/2tm
Ct=(epso*epsr*pi^2*aw*a)/tm %turn-to-turn capacitance
%Total series capacitance of a section having ns turns
C_tt=Ct/(ns-1); %Capacitances in series
Ctt=sprintf('%.5g F',C_tt)

%CALCULATION OF CAPACITANCE TO GROUND
clc
clear
%Dielectric constant
epso=8.854*10^-12;%vacuum F/m
epsa=1.0006; %air
%Reactor diameter--m
dr=0.902;
%Distance of reactor above ground--m
hg=0.127;
%Reactor length--m
br=2.65;
%10-sections of equal length
bs=br/10;
%Calculation of capacitance to ground by parallel plate formula
%Height from ground to the center of each section
hm_10=hg+(bs/2); %nearest section to ground
hm_9=hm_10+bs;
hm_8=hm_9+bs;
hm_7=hm_8+bs;
hm_6=hm_7+bs;
hm_5=hm_6+bs;
hm_4=hm_5+bs;
hm_3=hm_4+bs;
hm_2=hm_3+bs;
hm_1=hm_2+bs;  %highest section from ground

disp('SECTION CAPACITANCE TO GND: ')
%Section 1--the highest from ground
a=dr/2;
Cg1=(epso*epsa*2*pi*a*bs)/hm_1; %Paralle plate=(eps*area)/distance
Cg_1=sprintf('%.5g F',Cg1)
 %Section 2
Cg2=(epso*epsa*2*pi*a*bs)/hm_2;
Cg_2=sprintf('%.5g F',Cg2)
 %Section 3
Cg3=(epso*epsa*2*pi*a*bs)/hm_3;
```

```
Cg_3=sprintf('%.5g F',Cg3)
 %Section 4
Cg4=(epso*epsa*2*pi*a*bs)/hm_4;
Cg_4=sprintf('%.5g F',Cg4)
 %Section 5
Cg5=(epso*epsa*2*pi*a*bs)/hm_5;
Cg_5=sprintf('%.5g F',Cg5)
 %Section 6
Cg6=(epso*epsa*2*pi*a*bs)/hm_6;
Cg_6=sprintf('%.5g F',Cg6)
 %Section 7
Cg7=(epso*epsa*2*pi*a*bs)/hm_7;
Cg_7=sprintf('%.5g F',Cg7)
 %Section 8
Cg8=(epso*epsa*2*pi*a*bs)/hm_8;
Cg_8=sprintf('%.5g F',Cg8)
 %Section 9
Cg9=(epso*epsa*2*pi*a*bs)/hm_9;
Cg_9=sprintf('%.5g F',Cg9)
 %Section 10--the nearest to ground
Cg10=(epso*epsa*2*pi*a*bs)/hm_10;
Cg_10=sprintf('%.5g F',Cg10)
```

APPENDIX B

Goodfellow Cambridge Limited Ermine Business Park, Huntingdon PE29 6WR England
Telephone 0800 731 4653 : Fax 0800 328 7689

Polyethylene terephthalate
Polyester, PET, PETP

Common Brand Names : Arnite, Dacron, Hostaphan, Impet, Melinar, Melinex, Mylar, Rynite, Terylene, Trevira

General Description: The most common thermoplastic polyester, this polymer is often called just "polyester". This often causes confusion - not only is the chemically similar PBT also a (thermoplastic) polyester, the most common resin system used in GRP is also a polyester system - and also often called just "polyester". (In this latter case, however, the polyesters are chemically unsaturated and are "free-radical polymerised" into a thermoset).

PET is a hard, stiff, strong, dimensionally stable material that absorbs very little water. It has good gas barrier properties and good chemical resistance except to alkalis (which hydrolyse it). Its crystallinity varies from amorphous to fairly high crystalline; it can be highly transparent and colourless but thicker sections are usually opaque and off-white.

It is widely known in the form of biaxially oriented and thermally stabilised films usually referred to by their main brand names Mylar, Melinex or Hostaphan. Strictly speaking, these names should be used only for this type of film whose properties are different from, and in several respects superior to, those of "ordinary" PET film.

These "Mylar®-type" films are used for capacitators, graphics, film base and recording tapes etc. PET is also used for fibres for a very wide range of textile and industrial uses (Dacron®, Trevira®, Terylene®). Other applications include bottles and electrical components.

Physical Properties

Density	1.3-1.4 g cm^{-3}
Flammability	HB
Limiting oxygen index	21 %
Radiation resistance	Good
Refractive index	1.58-1.64
Resistance to Ultra-violet	Fair2
Water absorption - equilibrium	< 0.7 %
Water absorption - over 24 hours	0.1 %

Electrical Properties

Dielectric constant @1MHz	3.0
Dielectric strength	17 kV mm^{-1}
Dissipation factor @ 1kHz	0.002
Surface resistivity	10^{13} Ohm/sq
Volume resistivity	> 10^{14} Ohm.m

Thermal Properties

Coefficient of thermal expansion	20-80 x10^{-6} K^{-1}
Heat-deflection temperature @ 0.45MPa	115 C
Heat-deflection temperature - 1.8MPa	80 C
Lower working temperature	-40 to -60 C
Specific heat	1200 - 1330 J K^{-1} kg^{-1}
Thermal conductivity @23C	0.15-0.4 W m^{-1} K^{-1}
Upper working temperature	115-170 C

Mechanical Properties

Coefficient of friction	0.2-0.4
Hardness - Rockwell	M94-101
Izod impact strength	10-35 J m^{-1}
Poisson's ratio	0.37-0.44(oriented)
Tensile modulus	2-4 GPa
Tensile strength	80, for biax f or 190-280 MPa

Chemical Resistance

Acids - concentrated	Good-Poor
Acids - dilute	Good
Alcohols	Good
Alkalis	Poor
Aromatic hydrocarbons	Good-Fair
Greases and Oils	Good
Halogenated Hydrocarbons	Good-Poor
Halogens	Fair-Poor
Ketones	Good-Fair

Film

Dielectric Strength @25µm thick	kV mm^{-1}	300
Dissipation Factor @1MHz		0.016
Elongation at Break	%	60-165
Initial Tear Strength	g µm^{-1}	18-54
Permeability to Carbon Dioxide @25C	x10^{-15} cm^3. cm cm^{-2} s^{-1} Pa^{-1}	0.2
Permeability to Hydrogen @25C	x10^{-15} cm^3. cm cm^{-2} s^{-1} Pa^{-1}	0.4
Permeability to Nitrogen @25C	x10^{-15} cm^3. cm cm^{-2} s^{-1} Pa^{-1}	0.004
Permeability to Oxygen @25C	x10^{-15} cm^3. cm cm^{-2} s^{-1} Pa^{-1}	0.03
Permeability to Water @25C	x10^{-13} cm^3. cm cm^{-2} s^{-1} Pa^{-1}	100
Permeability to Water @38C	x10^{-13} cm^3. cm cm^{-2} s^{-1} Pa^{-1}	150
Specific Heat	kJ kg^{-1} K^{-1}	1.3
Thermal Conductivity @23C	W m^{-1} K^{-1}	0.13-0.15

ES301005 Thickness ..... 0.0005mm Coil width 315mm
Condition ..... Biaxially Oriented

XI

Coil Web Code	Width 315mm Length	Quantity 1 Reel
777-190-664	0.1 m	£ 174.00
673-214-694	0.2 m	£ 204.00
184-719-488	0.5 m	£ 272.00
055-309-801	1 m	£ 358.00
505-180-832	2 m	£ 498.00
092-446-056	5 m	£ 912.00

ES301007 Thickness ..... 0.0007mm Coil width 315mm
Condition ..... Biaxially Oriented

XI

Coil Web Code	Width 315mm Length	Quantity 1 Reel
444-702-124	0.1 m	£ 157.00
661-370-162	0.2 m	£ 181.00
833-489-721	0.5 m	£ 235.00
822-974-170	1 m	£ 306.00
038-111-267	2 m	£ 424.00
351-485-718	5 m	£ 722.00